

Dissertation
submitted to the
Combined Faculty of Natural Sciences and Mathematics
of Heidelberg University, Germany
for the degree of
Doctor of Natural Sciences

Put forward by
Anna Solvejg Dinger
Born in: Aalen
Oral examination: 8 January 2020

**Quantitative imaging of turbulent tracer dispersion
in the atmospheric boundary layer
with a tomographic setup of SO₂ cameras**

**Referees: Prof. Dr. Ulrich Platt
Prof. Dr. Werner Aeschbach**

Quantitative imaging of turbulent tracer dispersion in the atmospheric boundary layer with a tomographic setup of SO₂ cameras

Accurate models of turbulent dispersion are required for simulating the near-field concentration distribution of pollutants. However, high-resolution measurements of turbulent dispersion in the atmospheric boundary layer are sparse. This thesis describes the three artificial release experiments in the summers of 2017-2019 within the COMTESSA (Camera Observation and Modelling of 4D Tracer Dispersion in the Atmosphere) project and presents derived results for the turbulent dispersion of tracer puffs. Instantaneous puffs of sulfur dioxide (SO₂) were released from a tower on a military site in Norway. Column-integrated SO₂ concentrations were observed with SO₂ cameras from up to six viewing directions while the atmospheric flow was characterised by eddy covariance measurements at different altitudes along the release tower. A novel simplified tomographic approach was applied to reconstruct the dispersion of tracer puffs separated into their centre of mass trajectories and their dispersion around the centre of mass. Using ensembles of puff releases, the meandering, relative and absolute dispersion as well as the Lagrangian velocity autocorrelations were measured. The ratio of Lagrangian and Eulerian time scales was estimated to a lower bound of $\frac{T^L}{T^E} = 0.33 \cdot \frac{1}{i}$ where i is the turbulence intensity; agreeing with previous studies.

Quantitative Bildgebung von turbulenter Dispersion in der atmosphärischen Grenzschicht mit einem tomografischen Aufbau von SO₂ Kameras

Genauere theoretische Modelle von turbulenter Dispersion sind nötig, um die Konzentrationsverteilung von Umweltschadstoffen zu simulieren. Allerdings gibt es nur wenige hochaufgelöste Messungen von turbulenter Dispersion in der atmosphärischen Grenzschicht. Diese Doktorarbeit beschreibt die drei Freisetzungsexperimente innerhalb des COMTESSA Projektes und diskutiert abgeleitete Ergebnisse zur turbulenten Dispersion von Puffs aus Schwefeldioxid (SO₂). Diese wurden von einem Turm auf einem Militärfeld in Norwegen freigesetzt. SO₂ Kameras erfassten die integrierten SO₂ Konzentrationen aus bis zu sechs Blickrichtungen, während der atmosphärische Hintergrundfluss mittels Eddy-Kovarianz Messungen entlang des Turms charakterisiert wurde. Ein neuer tomografischer Ansatz wurde angewandt, um die Dispersion der Puffs zu rekonstruieren, aufgeteilt in Schwerpunktstrajektorien und der Dispersion um den Schwerpunkt. Durch statistische Analyse von vielen Puffs konnte das Mäandern, die relative und die absolute Dispersion sowie die Lagrangeschen Geschwindigkeitskorrelationen bestimmt werden. Die untere Grenze für das Verhältnis von Lagrangescher und Eulerscher Zeitskala wurde bestimmt zu $\frac{T^L}{T^E} = 0.33 \cdot \frac{1}{i}$ in Abhängigkeit der turbulenten Intensität i und bestätigt vorherige Studien.

Contents

1	Introduction	1
2	Turbulence in the atmospheric boundary layer	7
2.1	The atmospheric boundary layer	7
2.2	Statistical description of turbulence	10
2.3	Previous atmospheric transport and dispersion experiments	17
3	Remote sensing of SO₂ with ultraviolet cameras	21
3.1	Optical absorption spectroscopy	21
3.2	SO ₂ cameras	23
3.3	SO ₂ column density retrieval	25
3.4	Tomography of atmospheric SO ₂ distributions	28
3.5	COMTESSA SO ₂ cameras	28
4	The COMTESSA tracer dispersion experiments	33
4.1	Experimental site and instrumentation	33
4.2	Passive tracer release	38
4.3	Meteorological conditions	44
5	The COMTESSA tracer dispersion data set	47
5.1	Retrieval of column-integrated SO ₂ images	47
5.2	SO ₂ image data set	52
5.3	Discussion	61
6	Turbulent dispersion from SO₂ camera images	63
6.1	Detection of puffs	64
6.2	Three-dimensional trajectories	69
7	Statistical analysis of puff ensembles	79
7.1	Time intervals of nearly-stationary turbulence	79
7.2	Turbulent dispersion	85
7.3	Velocity correlations	91
8	Conclusions	101
A	Details on measurements and data analysis	107
A.1	Details on pose reconstruction	107
A.2	Analysis of eddy covariance time series	107
A.3	Optical camera calibration and distortion	108

List of Abbreviations	111
List of Figures	114
List of Tables	115
Personal bibliography	117
Bibliography	127
Acknowledgements	130

Chapter 1

Introduction

Most of us spend their entire lives on the Earth’s surface where our daily routines are affected by the weather. Close to the surface, within the so-called atmospheric boundary layer (ABL), turbulence is the driving force of many phenomena. Already Leonardo da Vinci [1510] wrote about and drew (Fig. 1.1) the apparently random nature of the motion of single fluid parcels, and still nowadays no complete theory exists. It is reported that even Nobel Laureate Richard P. Feynman claimed that “turbulence is the most important unsolved problem of classical physics” during one of his lectures [Feynman, 1964]. Besides the weather, atmospheric turbulence controls processes which impact people directly. For example, the turbulent dispersion of pollutants after natural, deliberate or accidental emission needs to be predicted in order to decide if and where an evacuation of the population is necessary or whether an aircraft can stay on route due to volcanic ash particles [e.g. Peterson et al., 2015; Mathieu et al., 2018]. On larger scales, turbulence indirectly limits surface fluxes to and from the atmosphere of e.g. water vapour or carbon dioxide as it controls the transport of the gases away from the surface [e.g. Roedel and Wagner, 2011].



Fig. (1.1) Leonardo da Vinci’s drawing of turbulence in water. Reproduced from Kemp [2019] after an original drawing in da Vinci [1510].

Turbulent dispersion of a tracer is described and simulated as a statistical process within a turbulent flow. Chapter 2 gives an introduction to the statistical description of turbulence and turbulent dispersion while this thesis presents measurements of short-scale

turbulent dispersion of sulfur dioxide (SO_2). Intuitively, turbulent dispersion is described in a reference frame moving with the dispersing particles, the so-called Lagrangian frame. Taylor [1921] linked the absolute dispersion (mean square displacement from the source) of a tracer in a homogeneous turbulent flow to the Lagrangian velocity autocorrelation of the tracer particles. For clusters of particles ("puffs"), the particles will disperse relative to their centre of mass in addition to a meandering motion of their centre of mass. This relative dispersion was described in the pioneering work of Richardson [1926] who found that the diffusivity is proportional to $\sigma^{4/3}$ where σ is the mean particle separation. Later, Batchelor [1952] extended the theory based on Kolmogorov's [1941] similarity theory. He obtained $\sigma^2 = C_r \epsilon t^3$ linking the relative dispersion σ^2 to the mean energy dissipation rate ϵ of the turbulent flow and introduced the Richardson-Obukhov constant C_r . Its exact value is still not exactly known due to a lack of empirical data and theoretical understanding [see e.g. Franzese and Cassiani, 2007] and the validity of the model under a wide range of atmospheric conditions was not yet observed. Further, the theoretical models are linked to the Lagrangian parameters of the background flow e.g the velocity correlations [see e.g. Sawford, 2001b]. Therefore, when the turbulent dispersion should be simulated using for example Lagrangian particle dispersion models (e.g. FLEXPART [Stohl and Thomson, 1999; Pisso et al., 2019]) or Large Eddy Simulations (LES) [Deardorff, 1972], knowledge of the Lagrangian quantities of the flow is required. However in practice, Eulerian (fixed-point) measurements of the velocity correlations are easier to perform and often readily available to characterise the turbulence due to their relatively simple application (e.g. automatic measurements at meteorological towers) and the models rely on parametrisations to derive the Lagrangian parameters from the measured, respective Eulerian ones. Therefore, there is a need to validate such models with atmospheric data obtained under different conditions to assess their reliability.

Measurement of atmospheric turbulent dispersion is challenging due to the high level of turbulence. The level of turbulence in a flow is assessed by the dimensionless Reynolds number which is given by the ratio of turbulence-producing inertial and turbulence-dissipating viscous forces in the Navier-Stokes equations [e.g. Roedel and Wagner, 2011]. The flow in the atmospheric boundary layer has the highest natural turbulence level on Earth with Reynolds numbers in the order of 10^7 [e.g. Stull, 1988]. The higher the Reynolds number, the wider the range of spatial and temporal scales which are involved in the turbulent flow. This means that a large range of scales has to be captured to characterise the turbulent flow in which the tracer dispersion should be observed. Additionally, the dispersion of the tracked fluid or particles has to be measured without disturbing the flow but with high level of detail. For these reasons, atmospheric observations are sparse up to this point. Hanna [2010] recently gave a comprehensive review of previous experimental studies. For most studies, a tracer substance (e.g. sulfur dioxide) is released from a fixed source (e.g. tower) and the tracer concentrations are sampled at discrete locations. Probably the most notable of these experiments is Prairie Grass [Barad, 1958] but many others followed. These experiments are however limited to concentration measurements at few points typically close to the ground rather than capturing the entire tracer concentration distribution. Alternatively, photographs of smoke plumes were used to study the relative dispersion [e.g. Gifford, 1957, 1980; Nappo et al., 2008]. Nowadays, these are replaced by scanning backscattering lidar measurements of smoke plumes allowing for measurement of the concentration fluctuations with up to 1 s resolution [e.g. Jørgensen and Mikkelsen, 1993; Munro et al., 2003; Hiscox et al., 2006; Jørgensen et al., 2010]. More intuitively, Lagrangian experiments follow marked particles or air parcels

and therefore allow for directly measuring the Lagrangian time scales and the concentration distribution (if sufficient many particles are tracked). Early experiments in the 20s of the last century have been carried out by Richardson [1926] with simple means as turnips and thistledown leading to his empirical $4/3$ -power law of eddy diffusivity. In later experiments, the trajectories of neutrally buoyant balloons were tracked [Gifford, 1955; Angell, 1964; Angell et al., 1971; Hanna, 1981] which confirmed the linear relationship between Eulerian and Lagrangian time scales [Hay and Pasquill, 1959]. However, the obtained data had high uncertainties (up to 50%) and due to the high cost, only few such studies are available. Empirical data has been important for model development but the exact values of model parametrisations (e.g. Richardson-Obukhov constant, relationship of Eulerian and Lagrangian time scales) still have a wide spread [see e.g. Franzese and Cassiani, 2007; Anfossi et al., 2006]. Hence, there is a need for more and high-resolution observations [Galmarini et al., 2011].

The aim of the project Camera Observation and Modelling of 4D Tracer Dispersion in the Atmosphere (COMTESSA) is to bring together simulations and observations of turbulent tracer dispersion in the ABL and thereby creating a solid base for model and theory development. For this end, a large team of scientists at the Norwegian Institute for Air Research (NILU) performed three artificial tracer release experiments to which the author participated. This thesis focuses on the tracer experiments and direct results from the obtained image data, while others within the project have worked on the technical aspects of the tracer releases, large eddy simulations of the ABL for comparable atmospheric conditions, tomographic reconstruction methods and further camera advances.

During three tracer release field campaigns every July in 2017-2019, continuous plumes and instantaneous puffs of sulfur dioxide (SO_2) were released into the ABL from a tower equipped with eddy covariance measurement systems. On short time scales as observed here, SO_2 can be considered a passive tracer as atmospheric removal processes result in SO_2 lifetimes of few hours to days [Lee et al., 2011; Fioletov et al., 2015]. At the same time, due to its negligible low atmospheric concentrations and strong absorption bands in the ultraviolet spectral range, SO_2 can be imaged with so-called SO_2 cameras [Mori and Burton, 2006] to visualise the atmospheric flow at high resolution. A set of six custom-made SO_2 cameras observed the SO_2 column integrated concentrations with few Hertz and few tens of centimetres resolution from different directions simultaneously. Chapter 3 will give details on the SO_2 camera method and the developed SO_2 cameras within this thesis and chapter 4 presents the three tracer release experiments. The obtained data set (chapter 5) is unique in the sense that it consists of high-resolution, quantitative image data of tracer dispersion in the ABL on different days and times and hence for different conditions of the surface layer.

The camera setup allows for a three-dimensional (3D) reconstruction of the concentration distribution. This full tomography is developed by another scientist at NILU and is not part of this thesis. Instead, in chapter 6 a novel simplified tomographic approach to study the dispersion of tracer puffs is introduced. The data analysis follows the steps as sketched in Fig. 1.2. While this thesis presents all field campaigns, the analysis focuses mainly on data obtained during the 2017 and 2018 campaigns. The 3D centre of mass trajectories of the puffs were reconstructed from the simultaneous image data from different directions. The trajectories were needed to link the image projections of the dispersion to the three-dimensional dispersion enabling the scaling of the images with the distance between camera and puffs. In this way, the size and trajectories of the puffs could be measured. In chapter 7, the novel method was applied to sets of puff releases

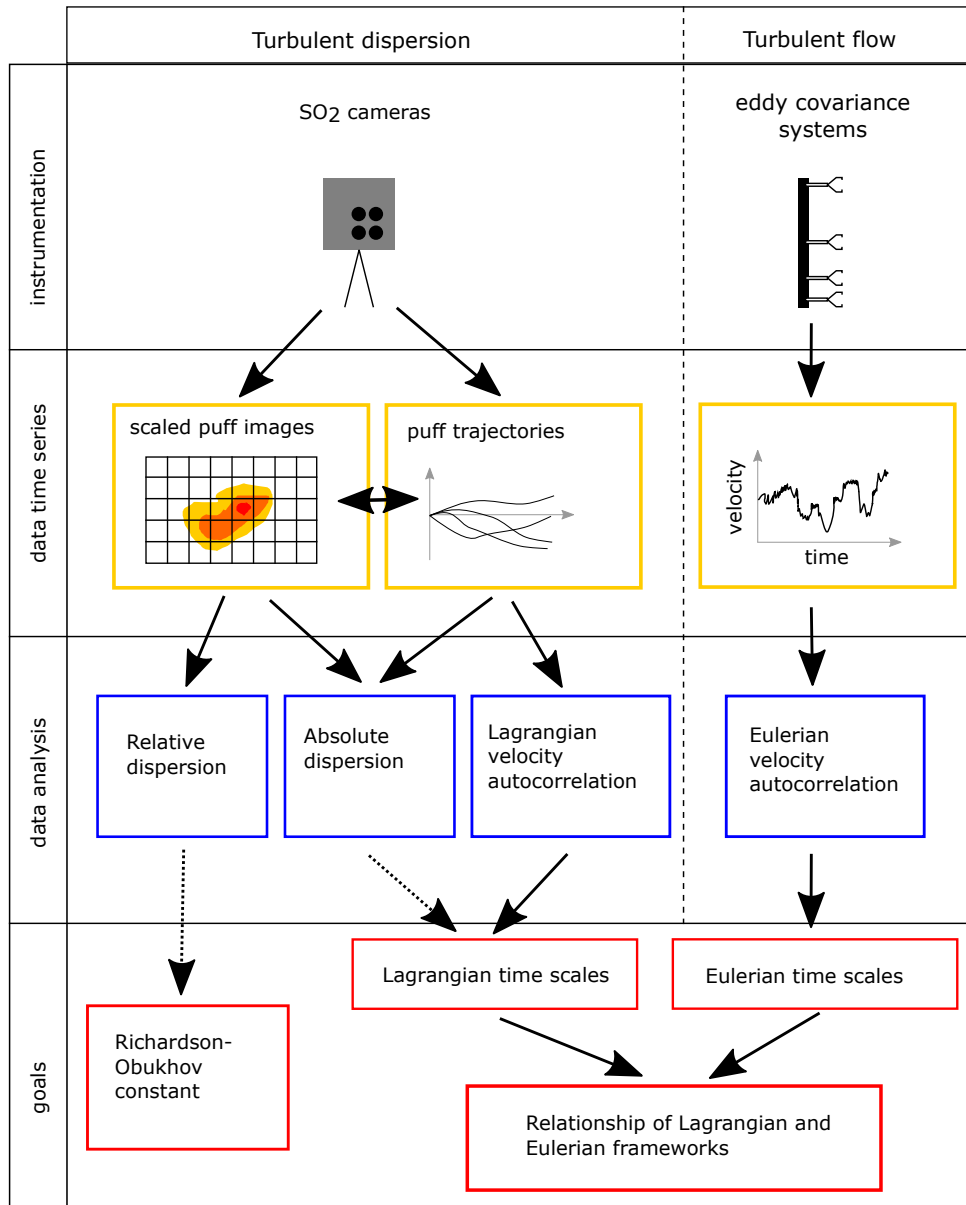


Fig. (1.2) Overview of analysis steps. The image data allowed to estimate different aspects of turbulent dispersion and Lagrangian time scales. The background flow was characterised by Eulerian eddy covariance measurements at different altitudes along the release tower. Steps following solid arrows have been successfully performed while dashed arrows symbolise a demonstration of concept within this thesis.

to study statistical aspects of turbulent dispersion. The meandering, relative and absolute dispersion of puff ensembles were estimated. Further, the image data and deduced trajectories enable a Lagrangian treatment of the centre of mass velocity correlations and integral time scales. Combined with the Eulerian velocity measurements at the tower, the presented data offers a chance to deepen our understanding of the link between Eulerian and Lagrangian frameworks.

Chapter 2

Turbulence in the atmospheric boundary layer

This chapter starts with a brief introduction to the atmospheric boundary layer which is the part of the atmosphere which is affected by turbulence. Within this layer, particles are transported by turbulent dispersion. Section 2.2 presents the statistical description of turbulence and turbulent tracer dispersion. In section 2.3, the COMTESSA experiments are put in the context of previous atmospheric dispersion experiments. This chapter follows the textbooks by Stull [1988], Arya [1999] and Roedel and Wagner [2011].

2.1 The atmospheric boundary layer

In meteorology, the Earth's atmosphere can be divided into two parts: The atmospheric boundary layer (ABL) which is significantly affected by the topography and processes on the Earth's surface and the free atmosphere [e.g. Stull, 1988]. In the free atmosphere, air motion is mostly independent of surface friction and the wind is almost geostrophic (parallel to the isobars). The atmospheric boundary layer extends through the lowest 100-3000 m of the atmosphere depending on the location. Surface friction and convection triggered by radiative heating of the surface produce turbulence which in turn lead to strong vertical mixing of the air masses within the ABL. Over land surfaces, the ABL shows a distinct diurnal cycle in the tropics and mid latitudes which is sketched in Fig. 2.1. During the day, a turbulent well-mixed layer extends through the ABL. About half an hour before sunset, convection decreases and a layer of residual air with decaying turbulence builds up. During night time, radiative cooling of the surface leads to a temperature stratification and the formation of a stable boundary layer in which turbulence is suppressed. The lowest 10% of the ABL where most of the turbulence is produced, is called surface layer.

2.1.1 Navier-Stokes equation

The motion of an air parcel in the atmosphere can be described by the Navier-Stokes equation

$$\rho \frac{d\vec{u}}{dt} = \rho \left(\frac{\partial \vec{u}}{\partial t} + (\vec{u} \cdot \vec{\nabla}) \vec{u} \right) \quad (2.1)$$

$$= -\vec{\nabla} p - \rho g + 2\rho(\vec{u} \times \vec{\Omega}) + \rho\nu \Delta \vec{u} \quad (2.2)$$

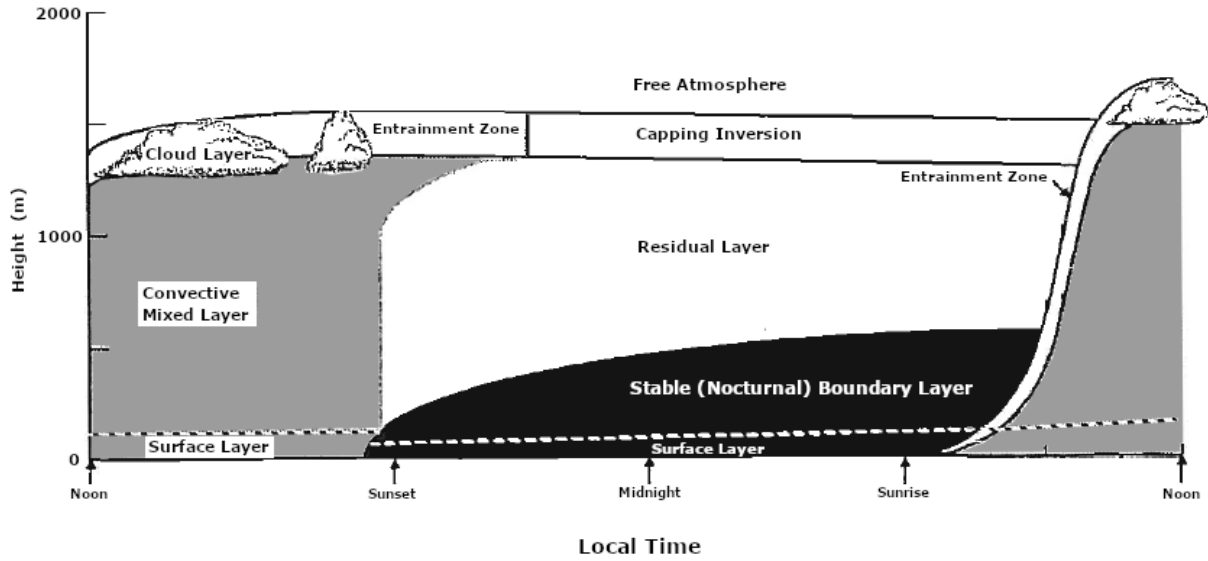


Fig. (2.1) Diurnal cycle of the atmospheric boundary layer. Adapted from Stull [1988, Fig.1.7].

where p , ρ , \vec{u} and ν describe the pressure, density, velocity and kinematic viscosity of the fluid parcel, g is the gravitational acceleration on Earth and Ω is the angular velocity [e.g. Roedel and Wagner, 2011]. The dynamics of the atmospheric flow is determined by the relative strength of the four terms in Eq. 2.2: the pressure gradient, gravitational forces, Coriolis force and friction. Above equation could be used to describe the flow of air if the initial conditions are perfectly known, which however in the atmosphere is for practical reasons almost never the case. At the same time, the non-linearity of the inertia term $((\vec{u} \cdot \nabla)\vec{u})$ prohibited until now to find a general, analytical solution. The difficulty to find a suitable approximation for the atmospheric flow lies in the large range of scales involved in turbulent motion. The dimensionless Reynolds number gives an estimate of how turbulent a flow is. It is defined as the ratio of turbulence-maintaining inertial forces and the turbulence-dissipating viscous forces.

$$Re = \frac{\rho u L}{\mu} = \frac{u L}{\nu} \quad (2.3)$$

for a flow with the characteristic length L (e.g. boundary layer height) and the dynamic $\mu = \rho\nu$, respectively. For typical values in the atmosphere (e.g. $\nu = 1.5 \times 10^{-5} \text{ m}^2\text{s}^{-1}$, $u = 5 \text{ ms}^{-1}$, $L = 100 \text{ m}$), the Reynolds number is 3×10^7 [e.g. Stull, 1988] or even higher. The higher the Reynolds number, the more spatial and temporal scales contribute to the turbulent motion (similarity scaling) while the largest scale is confined by the characteristic length scale.

2.1.2 Wind profile

The wind velocity in the ABL exhibits a typical vertical profile. In the free atmosphere, the wind flow follows in good approximation the geostrophic wind which is given by the balance of the pressure gradient and the Coriolis force. The flow direction is parallel to the isobars. Close to the Earth's surface, friction forces decrease the wind velocity. The

surface friction causes a shear stress τ_{xz} , which in turn produces turbulence. This shear stress can be expressed for convenience as a velocity, the so-called shear or friction velocity

$$u_* = \sqrt{\frac{\tau_{xz}}{\rho}} \quad (2.4)$$

Later in section 2.2, it will be seen that u_* can be measured statistically from the covariance of the velocity fluctuations close to the surface.

In a thermally neutral boundary layer (see section 2.1.3), the velocity gradient can only depend on the height z and the shear stress at the surface. From a dimensional analysis, it follows

$$\frac{\partial u_x}{\partial z} = \frac{1}{\kappa} \frac{u_*}{z} \quad (2.5)$$

where the proportionality constant κ is called von-Karman constant and was empirically determined to be $\kappa=0.4$. From Eq. 2.5 follows a logarithmic wind profile

$$u_x = \frac{u_*}{\kappa} \ln(z/z_0) \quad (2.6)$$

with the surface roughness z_0 . Typically values for z_0 range from 0.0001 m over calm sea to 1 m over a city [e.g. Stull, 1988]. This logarithmic wind profile is known as the Prandtl layer.

2.1.3 Stability types

In the description of the diurnal cycle of the ABL (see Fig 2.1), several stability types of the ABL were already introduced. Formally, the stability of the atmospheric boundary layer can be defined based on vertical buoyant fluxes. The Obukhov length L is defined as

$$L = -\frac{u_*^3 \overline{\theta'_v}}{\kappa g \overline{w' \theta'_v}}, \quad (2.7)$$

where $\overline{\theta'_v}$ is the mean virtual potential temperature and $\overline{w' \theta'_v}$ is the vertical turbulent flux of virtual potential temperature. The Obukhov length measures the relative importance of buoyant forces and wind shear to the production of turbulent kinetic energy and can be interpreted as proportional to the height at which both terms become equal. The Obukhov length is often used as scaling parameter for the height, $\zeta=z/L$, to compare turbulent flows and plays a central role in the Monin-Obukhov similarity theory [Monin and Obukhov, 1954].

In a thermally neutral boundary layer, the potential temperature is constant and the vertical turbulent flux of virtual potential temperature converges towards zero (L towards infinity). The logarithmic wind profile (Eq.2.5) is adaptable here. In the tropics and during day time in the mid-latitudes, typically a convective boundary layer is present. Solar heating causes a thermal instability at the surface which causes a positive buoyancy-driven vertical flux and increased turbulent mixing. Consequently, the Obukhov length is negative. During night time and during inversion layers, radiative cooling leads to a stable stratification of potential temperature and therefore suppressed vertical fluxes. During stable conditions, turbulent mixing is damped and only the shear stress at the surface causes turbulence. The Obukhov length is positive.

For non-neutral stratification, the wind profile (Eq. 2.5) can be adapted by adding a correction factor $\Phi(\zeta)$ and becomes

$$\frac{\partial u_x}{\partial z} = \frac{u_*}{\kappa \cdot z} \Phi(\zeta) \quad (2.8)$$

2.2 Statistical description of turbulence

Without knowing the exact environment, the behaviour of a single fluid element cannot be predicted. However, its motion can be modelled as a stochastic process. In this way it is possible to predict the statistical distribution of a large number of fluid elements or particles. In a statistical description of turbulence, it is handy to separate physical quantities into their mean (either temporal or spatial) and fluctuations around the mean. This is known as Reynolds decomposition. For example, a quantity $A(t)$ is described as

$$A(t) = \overline{A(t)} + A'(t) = \frac{1}{T} \int_0^T A(t') dt' + A'(t) \quad (2.9)$$

where \overline{A} denotes an average with averaging time T and A' the deviation from the average. Obviously, the separation will depend on the choice of the averaging time. The fluctuations of the velocity of the turbulent flow is often used to characterise the flow. At convenience in this thesis, the velocity components are described as $\vec{u} = (u_1, u_2, u_3) = (u, v, w)$ where u is the component along the average flow direction, v is the cross wind component and w is the vertical component. Further σ^2 is used to describe the statistical variance of a component, e.g. $\sigma_u^2 = \overline{u'(t)^2}$.

The mean flow field, which can be understood as the stable flow without turbulence, is described by the mean velocity while the fluctuations of the velocity (amplitude and temporal behaviour) contain the information about the turbulence. These fluctuations can be studied by analysing the energy (or power) spectrum of the fluctuations or by looking directly at the temporal correlation of the turbulent velocity fluctuations to itself. This is a way of analysing how long an air parcel "remembers" its prior motion. In the following the energy spectrum is introduced (section 2.2.1) and the links to the velocity autocorrelations are made clear (section 2.2.2). Finally, it is described how the energy spectrum and the autocorrelations are used to predict the turbulent dispersion (section 2.2.3).

2.2.1 Energy spectrum and Kolmogorov's similarity theory

The energy spectrum $E(f)$ describes the distribution of kinetic energy E over the frequencies f

$$E = \int_0^\infty E(f) df = \frac{1}{2} \overline{u_i(t) u_i(t)} \quad (2.10)$$

Each frequency can be interpreted as the contribution of all eddies with the same size. Taylor [1938] introduced the approximation of "frozen turbulence" which assumes that an eddy is not changing significantly when it is advected with the mean flow over a fixed point e.g. a sensor. With this approximation, time t and length scales r are linearly connected $t = r/\bar{u}$ via the mean wind \bar{u} . Then, the energy spectrum can be interchangeably expressed as energy distribution over temporal or spatial scales, most commonly the wavenumber $k = \frac{2\pi}{r}$.

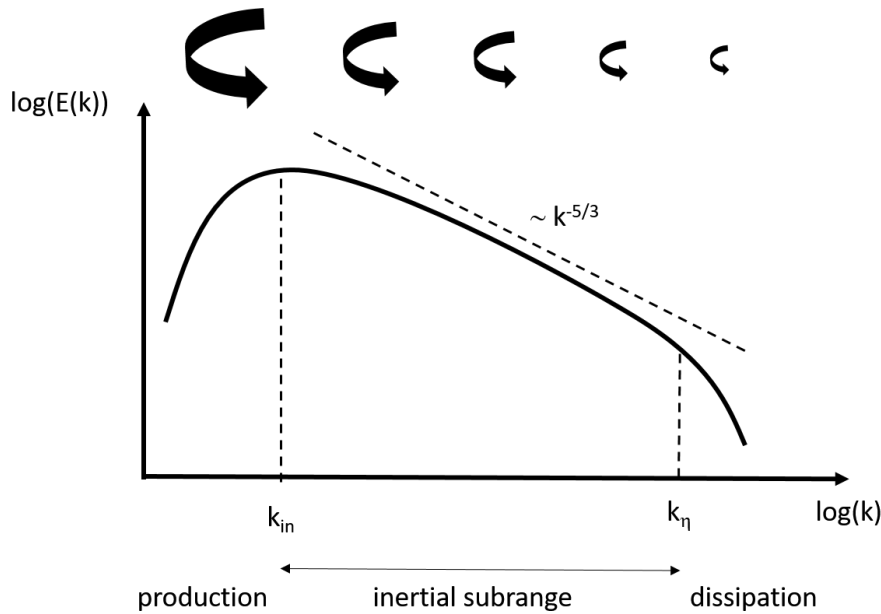


Fig. (2.2) Energy cascade according to Kolmogorov's similarity theory. Turbulent energy is produced at large scales (small wavenumbers). Within the inertial subrange, the energy is transferred to smaller eddy sizes. At scales smaller than the Kolmogorov scale k_η , energy is dissipated by viscous friction.

The form of the energy spectrum (Fig. 2.2) is often described as energy cascade. Large scale eddies produced by the topography or wind shear input turbulent energy into the system. The large eddies break eventually and divide into smaller eddies. These eddies break into smaller ones and so on until the length scales of the eddies are so small that viscous forces play a role. On these small scales, turbulent energy is dissipated into heat due to viscosity. The rate at which the energy cascades to smaller scales is given by the mean rate of energy dissipation ϵ .

In 1941, Kolmogorov presented his seminal work to describe the energy cascade quantitatively for large Reynolds numbers. He postulated two conceptual hypotheses: (1) Through the energy cascade, initial directional information is getting lost and turbulence becomes isotropic on smaller scales. In the dissipation subrange, the energy can only depend on the mean energy dissipation ϵ and the kinematic viscosity ν . From dimensional analysis, the scale at which this range onsets is known as Kolmogorov micro scale $k_\eta = (\frac{\nu^3}{\epsilon})^{1/4}$. (2) In the so-called inertial subrange, inertial forces are far more important than viscous forces. In consequence, the inertial subrange depends only on the energy dissipation. By a dimensional analysis, he concluded that

$$E(k) = C_k \epsilon^{2/3} k^{-5/3} \quad (2.11)$$

is the only possible form in the inertial subrange with the Kolmogorov constant C_k [e.g. Stull, 1988; Pope, 2000]. By measuring the energy spectrum, the mean rate of energy dissipation can be determined.

2.2.2 Autocorrelation

Air parcels and particles in turbulent flows are subject to random accelerations. However, in comparison to a random-walk movement, the air parcel or particle "remembers" its previous state. Statistically, such movements are modelled by a Markov chain [e.g. Sawford, 2001b]. Autocorrelation functions, i.e. the correlation of a particle's velocity with its velocity at a later time or place, are useful to quantify the duration and distance of the "memory". The autocorrelation can be described in two frameworks: Eulerian and Lagrangian statistics (Fig. 2.3).

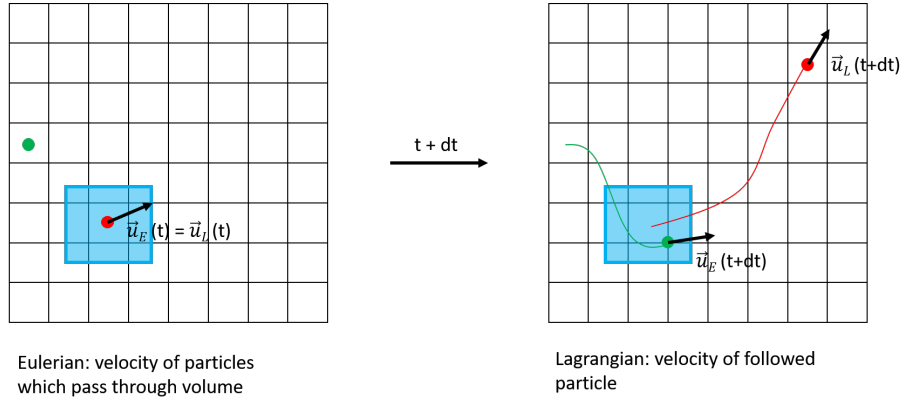


Fig. (2.3) Lagrangian and Eulerian frameworks. Eulerian measurements consider air parcels passing through a fixed point in space while Lagrangian measurements follow the motion of an air parcel.

In the Eulerian description, the quantity of interest (e.g. velocity, concentration,...) is measured at a fixed point. For example, instruments on a meteorological tower will record time series at fixed measurement spots. Most atmospheric turbulence experiments rely on the Eulerian description by using, for example, grids of fixed sensors. The Eulerian autocorrelation of the velocity fluctuations is given by

$$R_{u_i}^E(\tau) = \frac{\overline{u_i'(t) \cdot u_i'(t + \tau)}}{\overline{u_i'^2(t)}}. \quad (2.12)$$

where τ is the time lag. Here, the "memory" can be interpreted as an eddy of certain size passing over the sensor and therefore leading to a velocity of the same sign for about half of time when considering Taylor's hypothesis of frozen turbulence. In the Lagrangian description, a moving frame is considered: air parcels or particles are tracked along their path. Air parcels are correlated with themselves. Such experiments are harder to realise, e.g. tracking of balloons, and are therefore less common. The Lagrangian autocorrelation function is given by

$$R_{u_i}^L(\tau) = \frac{\langle u_i'(t) \cdot u_i'(t + \tau) \rangle}{\langle u_i'^2(t) \rangle} \quad (2.13)$$

where $\langle \rangle$ represents the average over an ensemble of followed air parcels.

Based on these definitions of the Eulerian and Lagrangian autocorrelations, it can be shown [see e.g. Roedel and Wagner, 2011] that the energy spectrum (Eq. 2.10) and the autocorrelation function can be expressed as a Fourier transform pair. The Eulerian spectrum for the component u_i is given as

$$E^E(f) = \frac{1}{2} \cdot \overline{u_i'^2(t)} \cdot \int_0^\infty R_{u_i}^E(\tau) \cdot e^{i2\pi f\tau} d\tau \quad (2.14)$$

The typical shapes of the autocorrelation functions and energy spectra are sketched in Fig. 2.4. In a first approximation, the curves can be described as exponential decays of the "memory"; that is for the Lagrangian view $R_{u_i}^L(\tau) = \exp(\tau/T_{u_i}^L)$; [e.g. Taylor, 1921; Csanady, 1973] where the (Lagrangian) integral time scale

$$T_{u_i}^L = \int_0^\infty R_{u_i}^L(\tau) d\tau \quad (2.15)$$

gives the decay constant. Analogously the Eulerian integral time scale $T_{u_i}^E$ is defined.

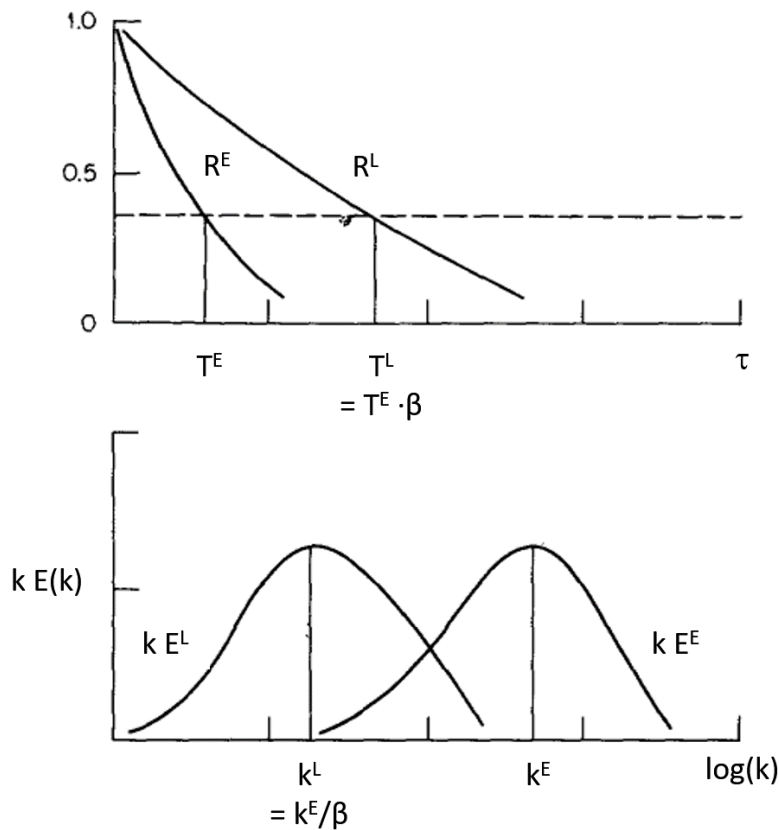


Fig. (2.4) Comparison of autocorrelation functions (upper panel) and energy spectra (lower panel) in the Lagrangian and Eulerian framework. The curves are self-similar: The Lagrangian frame follows the motion of the fluid and experiences a linear stretching of time. Adapted from Hanna [1981].

Intuitively, the correlation of a air parcel relative to itself decreases slower than the correlation between different air parcels passing through the same space. Hay and Pasquill [1959] assumed that the Eulerian and Lagrangian autocorrelation functions are similar in shape. This corresponds to a linear scaling of time and a constant ratio of the Eulerian and Lagrangian integral time scales $\beta = \frac{T^L}{T^E}$. Theoretical studies [Corrsin, 1963; Pasquill and Smith, 1983] predicted an inverse proportionality between β and the turbulence intensity $i_i = \frac{\sigma_{u_i}}{\bar{u}}$

$$\frac{T_{u_i}^L}{T_{u_i}^E} \frac{\sigma_{u_i}}{\bar{u}} = \beta i_i \approx C. \quad (2.16)$$

The exact value of C is of importance particularly for Lagrangian dispersion models as it allows to estimate the Lagrangian time scales by measuring Eulerian velocities. Eulerian measurements are considerably easier to perform, e.g. with a sonic anemometer on a tower [Foken, 2008] and might be routinely available for a particular event (e.g. volcanic eruption, accidental release of pollutants,...) which should be modelled. Lagrangian measurements instead require extensive tracking of e.g. balloons and are therefore sparse. Theoretical studies [Wandel and Kofoed-Hansen, 1962; Saffman, 1963; Pasquill and Smith, 1983; Koeltzsch, 1998] give values of the constant C between 0.3 and 0.8. The scatter in the values estimated from experimental studies in the ABL and from simulations is wide and no consensus exists. Table 2.1 gives an overview of the estimates from recent studies.

Early atmospheric studies [Gifford, 1955; Angell, 1964; Angell et al., 1971] tracked balloons or tetroons and found values of β ranging from 3 to 4. Hanna [1981] compared balloon trajectories with simultaneous tower and aircraft measurements and proposed an empirical value of $C=0.7$. However the data basis shows a wide scatter and an error of at least 50% for T^L and β is assumed. To the author's knowledge, since then no measurements of C in the atmospheric boundary layer have been performed. LES are a suitable tool to study the autocorrelations as they are dominated by the large scale motion which is resolved in LES. Simulations (LES and DNS at low Reynolds numbers) suggest values between 0.35 to 0.8 [e.g. Wang et al., 1995; Luo et al., 2007]. These studies modelled a homogeneous channel flow which represents only a thermally neutral boundary layer. The atmosphere is often unstable and turbulence might be heterogeneous. Dosio et al. [2005] compared the height-dependency of β obtained from LES of a convective boundary layer and found that it generally agrees with Hanna [1981] but towards the top $C=0.4$ represent the LES better. Anfossi et al. [2006] used LES to simulate turbulent flow for strongly convective, buoyancy-dominated and neutral conditions and found a higher value ($C\approx 0.6$) for strongly convective conditions compared to neutral conditions ($C\approx 0.4$).

During the COMTESSA experiments, the Eulerian autocorrelation can be calculated from the eddy covariance measurements at the tower, while the Lagrangian autocorrelation function can be retrieved from the image data with some assumptions. Therefore the data set is suited to study the relationship between Eulerian and Lagrangian frameworks.

2.2.3 Particle dispersion

When a tracer (e.g. gas, particles, ...) is released into the ABL, its concentration distribution will disperse due to the turbulent flow. To predict downwind tracer concentrations, the turbulent dispersion needs to be described. Even if it is not possible to predict the movement of single particles, the statistical mean can be predicted. Averaged over a large number of particles, the mean square displacement from the source of the release is called absolute dispersion. When the total released amount of the tracer is known, the absolute dispersion can be scaled to describe the mean tracer concentration. Releases from a realistic source cannot be considered as point emissions but have an finite source distribution. Considering such an extended source, the released plume or puff will disperse relative to its centre of mass/centre line, called relative dispersion, and it will be moved as a whole in a meandering motion (see Fig. 2.5). It can be beneficial for model development to study these two phenomena separately. Mathematically, the absolute mean square displacement σ^2 is given by the sum of the meandering σ_{cm}^2 and relative component σ_r^2

$$\sigma^2 = \sigma_{cm}^2 + \sigma_r^2 \quad (2.17)$$

Table (2.1) Overview of previous studies on the Eulerian-Lagrangian transformation

Reference	type of study	$C=\beta i$
Wandel and Kofoed-Hansen [1962]	theoretical	0.44
Pasquill and Smith [1983]	review of theoretical works	0.3 - 0.8
Koeltzsch [1998]	theoretical	$0.8 \frac{u_{adv}}{u}$
Gifford [1955]	balloon and tower/airplane	-
Angell [1964]	tetroon and tethered balloon	$3.3i^*$
Angell et al. [1971]	tetroon and tower	$2.5i - 4i^*$
Hanna [1981]	balloon and tower/airplane	0.7
Wang et al. [1995]	LES, channel flow	0.6
Dosio et al. [2005]	LES, convective boundary layer	0.4-0.7*
Anfossi et al. [2006]	LES, three stability conditions	0.36 - 0.64
Mito and Hanratty [2002]	DNS, channel flow	*
Luo et al. [2007]	DNS, channel flow	0.6 (for u)

* no explicit calculation of C

In the beginning, most eddies are much larger than the puff diameter and will move it as a whole. Thus, meandering is important in the beginning. Relative dispersion on the other hand is driven by scales comparable to the size of the puff ensuring effective mixing with the surrounding air. As the puff disperses and grows, more and especially more energetic scales (compare Fig. 2.2) contribute to the relative dispersion and the relative dispersion accelerates.

Absolute dispersion

Taylor [1921] demonstrated that the absolute dispersion $\sigma_{x_i}^2$ along the coordinate axis x_i from a point source is directly linked to the Lagrangian autocorrelation function

$$\sigma_{x_i}^2(t) = 2 \cdot \langle u_i^2(t) \rangle \int_0^t \int_0^{t'} R_i^L(\tau) d\tau dt' \quad (2.18)$$

where t is the time after release. According to Taylor's theory and assuming homogeneity and an exponential autocorrelation function [see e.g. Arya, 1999] the evolution of the absolute dispersion is modelled as

$$\sigma_{x_i}^2(t) = 2 \cdot \langle u_i^2(t) \rangle \cdot (T_{u_i}^L)^2 \left(\frac{t}{T_{u_i}^L} - \left[1 - \exp\left(-\frac{t}{T_{u_i}^L}\right) \right] \right). \quad (2.19)$$

For short and large dispersion times, Equation (2.19) has two analytical limits

$$\sigma_{x_i}^2(t) = \langle u_i^2(t) \rangle \cdot t^2 \quad \text{for } t \ll T_{u_i}^L \quad (2.20)$$

$$= 2 \cdot \langle u_i^2(t) \rangle \cdot T_{u_i}^L t \quad \text{for } t \gg T_{u_i}^L \quad (2.21)$$

This means that the particles initially disperse rapidly and independently of the Lagrangian time scale. For large dispersion times, the dispersion slows and becomes proportional to t . Hence, for large dispersion times, the behaviour is analogous to molecular diffusion and is described as "eddy diffusivity".

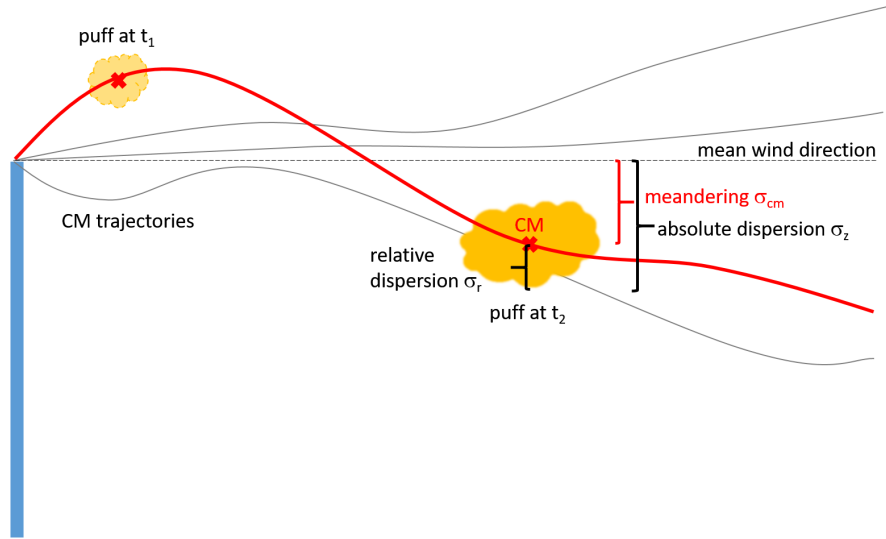


Fig. (2.5) Sketch of absolute dispersion from an extended source, divided in meandering and relative dispersion. The centre of mass of the released puffs follow a meandering trajectories while they also disperse around their centre of mass. By considering an ensemble of a large number of releases, the variance of the trajectory distribution is called meandering and the average dispersion around the centre of mass is called relative dispersion. Adapted from Dinger et al. [2018].

Relative dispersion

The following paragraph is adapted from Dinger et al. [2018].

A cluster of particles released at the same time from a finite source will follow slightly different paths and form a distribution around its centre of mass. The relative dispersion is therefore influenced by the source size r_0 , i.e. the initial separation of the particles. For an initial particle separation (puff size) in the inertial subrange of turbulence, the particle separation will be first influenced by the source size and then become independent of the initial separation [e.g. Monin and Yaglom, 1975; Franzese and Cassiani, 2007, Eq. A1-A6]. Based on inertial range scaling arguments [e.g. Monin and Yaglom, 1975], the characteristic time scale of the source is given by

$$t_s = \left(\frac{r_0^2}{\epsilon} \right)^{1/3}, \quad (2.22)$$

where ϵ is the mean dissipation of turbulent kinetic energy.

Batchelor [1952] showed that for $t \ll t_s$ the spread of a puff, or cluster of particles, is dominated by the initial velocity differences between the particles ("ballistic regime")

$$\langle \mathbf{r}^2 \rangle = r_0^2 + \frac{11}{3} \cdot C_k \cdot \epsilon^{2/3} \cdot r_0^{2/3} \cdot t^2 \quad \text{for } t \ll t_s \quad (2.23)$$

where C_k is the Kolmogorov's constant for the longitudinal structure function in the inertial subrange. Here, \mathbf{r} is the 3D separation between two particles of the cluster and $\langle \mathbf{r}^2 \rangle$ is the ensemble mean square separation between all particles of the cluster. In homogeneous isotropic turbulence, $\langle \mathbf{r}^2 \rangle$ is related to the 1D relative dispersion as $\sigma_{r,i}^2 =$

$\langle \mathbf{r}^2 \rangle / 6$ [see e.g. Franzese and Cassiani, 2007]. Eq. 2.23 reduced to the relative dispersion along a single axis x_i is given by

$$\sigma_{r,x_i}^2(t) = \sigma_{r,x_{i0}}^2 + 6^{-2/3} \cdot \frac{11}{3} \cdot C_k \cdot \epsilon^{2/3} \cdot \sigma_{r,x_{i0}}^{2/3} \cdot t^2 \quad (2.24)$$

with the 1D initial separation

$$\sigma_{r,x_{i0}}^2 = \frac{r_0^2}{6}. \quad (2.25)$$

For larger times $t \gg t_s$, the rate of change of particle separation becomes independent of the initial separation, and the spread of the puff is proportional to the Richardson-Obukhov constant C_r according to the Richardson-Obukhov scaling [e.g. Monin and Yaglom, 1975]

$$\langle \mathbf{r}^2 \rangle = r_0^2 + C_r \cdot \epsilon \cdot t^3 \quad \text{for } t \gg t_s \quad (2.26)$$

The value of the Richardson-Obukhov constant is uncertain, as it is difficult to estimate from experiments and numerical simulations [see Franzese and Cassiani, 2007, for a detailed discussion]. However, C_r and the directly related relative dispersion are important for models as the relative dispersion defines the effective rate of mixing of a puff and therefore the decay rate of concentration fluctuations [e.g. Sawford, 2004; Cassiani et al., 2005; Pinsky et al., 2016; Marro et al., 2018].

2.3 Previous atmospheric transport and dispersion experiments

Atmospheric experiments and data sets are crucial for model development and validation. For this, observations under a wide range of conditions and resolutions are required to assess also the models' universality. The focus of the experiments co-developed with society's needs from fundamental aspects of turbulent transport to predictions after accidental or military release of toxic or radioactive substances to air pollution modelling. In general, atmospheric dispersion studies can be divided by the measurement framework: Eulerian (concentration measurements at fixed locations) or Lagrangian (trajectories). Eulerian sampling can be both in-situ or using remote sensing techniques. Figure 2.6 sketches the typical experimental setups which will be detailed below. All dispersion experiments have in common, that the background turbulent flow in which the tracer disperses has to be characterised. Typically this is done by retrieving turbulent fluxes from high frequency sonic anemometry measurements along a tower using the eddy covariance (EC) technique [e.g. Foken, 2008]. In the following several selected examples are given but for an extensive list of historic experiments, the reader is referred to Hanna [2010] or the textbook Arya [1999] section 7.7.

2.3.1 Eulerian experiments

Eulerian experiments are the most performed type of experiments. A passive tracer (e.g. sulfur dioxide, sulfur hexafluoride) is released in the ABL and its concentration is measured by sensors at fixed positions along a grid or tower. The wide, flat areas of Northern America provide many ideal test sites for studying undisturbed turbulence. For example the sites Round Hill Field Station of MIT, O'Neill, Nebraska and Hanford site, Washington were used for extensive field experiments by the US military [Hanna, 2010].

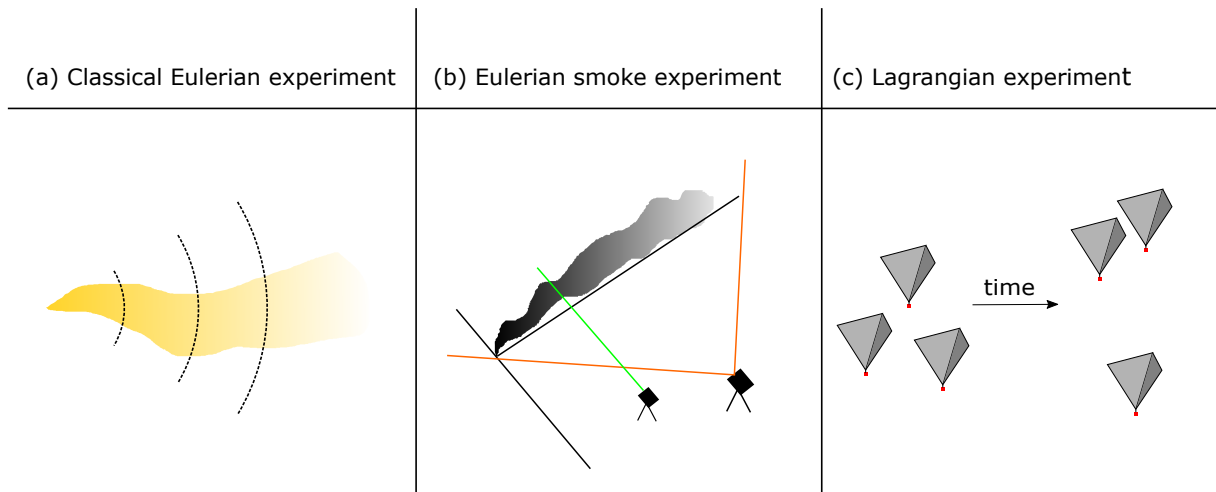


Fig. (2.6) Overview of different study design for atmospheric dispersion experiments. (a) In classical Eulerian experiments, a tracer is released from a point, line or grid source and observed at sensors on the ground, towers or aircrafts. (b) Releases of smoke plumes and puffs are observed with remote-sensing instruments (photography, LIDAR) (c) In classical Lagrangian experiments, tetroons or balloons are equipped with sensors or their position are tracked from the ground using theodolites or radar.

Probably, the most prominent data set is the Prairie Grass field experiment during which sulfur dioxide was released in 1956 in Nebraska [Barad, 1958]. The data set has played a prominent role in the development of models and the quality of the data makes it still used nowadays [e.g. Sawford, 2001a; Olesen et al., 2007; Venkatram, 2010]. Other examples of Eulerian experiments are the Green Glow at the Hanford site [Fuquay et al., 1963], the Ocean Breeze [Haugen and Fuquay, 1963] and the Dry Gulch [Haugen and Fuquay, 1963] projects.

More recent examples include the projects Sagebrush and Jack Rabbit. The NOAA Air Resources Laboratory carried out two phases of SF_6 releases in the project Sagebrush [Finn et al., 2015, 2017] at the Idaho national Laboratory and sampled the concentration along arcs 100-400 m away from the source. The plume dispersion could be studied over a range of seasons and atmospheric conditions and was compared to early studies as e.g. Prairie Grass [Finn et al., 2016, 2018]. In 2010-2016, the US Department of Homeland Security conducted the Jack rabbit I and II trials (<https://www.uvu.edu/esa/jackrabbit/>) releasing large amounts of liquefied chlorine at the Dugway Proving Ground in Utah. The data set is comprehensive and is already widely used by several groups for model evaluation of dense gas dispersion [e.g. Gant et al., 2018]. Tracer experiments were also conducted under more complex conditions, for example to study dispersion in urban areas [e.g. Fast et al., 2006]. Other experiments were conducted on much larger, up to continental, scales [Nodop et al., 1998].

2.3.2 Eulerian experiments using remote sensing techniques

The COMTESSA experiments are most comparable with classical smoke experiments. Image data are particularly suited to study the relative dispersion. Photographs of smoke plumes and puffs can be used to retrieve the optical outline [Roberts, 1923]. Assuming

a Gaussian shape in the horizontal [Gifford, 1957, 1980], the visible edge represents a constant concentration threshold which can be linked to the relative dispersion. However, quantitative concentration measurements are not possible. Nappo et al. [2008] gives a comprehensive review of the method and a summary of studies using smoke plumes. They outline the advantage that "[t]he analysis of plume images as proposed by Frank Gifford is an efficient and accurate way to obtain turbulence and dispersion data from regions or under conditions that are otherwise inaccessible to instrumentation", for example by aerial or satellite images.

The modern analogous and extension of black-and-white photography is backscatter lidar in scanning mode [e.g. Jørgensen and Mikkelsen, 1993; Mikkelsen et al., 2002; Schröter et al., 2003; Hiscox et al., 2006; Jørgensen et al., 2010]. In contrast to photo film, lidar samples concentrations at rates up to 1 Hz [Jørgensen et al., 2010]. Lidar is not constrained to day-time measurements and can be used to study the stable night time boundary layer [Hiscox et al., 2006].

2.3.3 Lagrangian experiments

The Lagrangian framework is the most intuitive framework to study the dispersion of a pollutant by considering a frame moving with the pollutant. In atmospheric experiments, neutrally buoyant balloons were released and passively transported with the air flow. Early studies tracked the balloons manually from the ground using radar or theodolites [Gifford, 1955; Angell, 1964; Angell et al., 1971; Hanna, 1981], limiting the sampling time to 30 min. With the development of cheap GPS sensors and communication, balloons are nowadays equipped with a variety instrumentation to monitor e.g. temperature, humidity or tracer concentrations [Zak, 1981; Businger et al., 1996, 2006]. As described in section 2.2.2, the balloon trajectories were used to study Lagrangian time scales [Gifford, 1955; Angell, 1964; Angell et al., 1971; Hanna, 1981] and by releasing clusters of balloons, the relative dispersion can be analysed in principle [e.g. Businger et al., 2006]. However, increasing cost and complexity of balloon releases (e.g. 8000\$ material cost for a NOAA smart balloon [Businger et al., 2006]) limited the overall number of Lagrangian experiments. The trajectories of the puffs released during COMTESSA are comparable to the trajectories of neutral balloons under the conditions that the puffs stay small.

2.3.4 Accessibility of experimental data

The cost of atmospheric dispersion experiments have increased to amounts that substantial funding is necessary. As a consequence, historic and new data set are highly valued and re-used for model validation and parametrisation. The impact of an atmospheric dispersion study therefore depends largely on its accessibility, integrity and documentation. Efforts have been made to digitalise classic data sets and make them publicly available [e.g. Modelers' Data Archive (MDA) Chang and Hanna, 2010]. Military data sets are often classified and other data can be inquired from the respective institutes. The "Harmonisation in atmospheric dispersion modelling for regulatory purposes" initiative has been founded in 1991 to improve collaboration and to standardise atmospheric dispersion models. It offers links to many data sets with comprehensive descriptions on its website (www.harmo.org). It is planned that the data set obtained in COMTESSA will be made available in the future.

Chapter 3

Remote sensing of SO₂ with ultraviolet cameras

3.1 Optical absorption spectroscopy

Radiation is interacting with molecules and particles when passing through the atmosphere by absorption, scattering and emission. Many atmospheric remote sensing applications are based on absorption spectroscopy using an active (artificial, e.g. LASER) or passive light source (natural, e.g. sun, moon). The effect of the interactions on the radiation $I(\lambda)$ emitted from the light source is quantitatively given by the Beer-Lambert-Bouguer law

$$dI(\lambda, x) = -I(\lambda) \cdot \sum_i^N \sigma_i(\lambda, p, T) \cdot c_i(x) dx, \quad (3.1)$$

which describes the loss of radiation dI at wavelength λ along the light path x through a medium at pressure p and temperature T containing N species with absorption cross sections $\sigma_i(\lambda, p, T)$ and concentrations $c_i(x)$. The absorption cross sections are wavelength dependent and specific to every species as atoms and molecules can be excited to higher energy states by absorbing photons of matching energy depending on their electron configuration. They can be therefore seen as "molecular fingerprints" of that absorber. In general, the absorption cross sections depend further on the ambient pressure and temperature. For ultraviolet and visible radiation, this dependency is typically negligible and the dependencies are dropped ($\sigma_i(\lambda, p, T) \approx \sigma_i(\lambda)$) in the following equations for simplicity. A detector at distance L from a light source, which emits the initial radiation $I_0(\lambda)$, will observe

$$I(\lambda, L) = I_0(\lambda) \cdot \exp(-\tau(\lambda)) \quad (3.2)$$

where the optical density $\tau(\lambda)$ is defined as

$$\tau(\lambda) = - \int_0^L \sum_i^N \sigma_i(\lambda) \cdot c_i(x) dx = \sum_i^N \sigma_i(\lambda) \cdot S_i. \quad (3.3)$$

The slant column density (SCD) S_i describes the integrated concentration along the light path. When multiple-scattering can be neglected, the light path can be approximated with the geometric length L' of a cloud of absorbers (e.g. when observing a distinct exhaust or volcanic plume). The average absorber concentration in the plume is then

simply given by

$$\bar{c}_i = \frac{S_i}{L}. \quad (3.4)$$

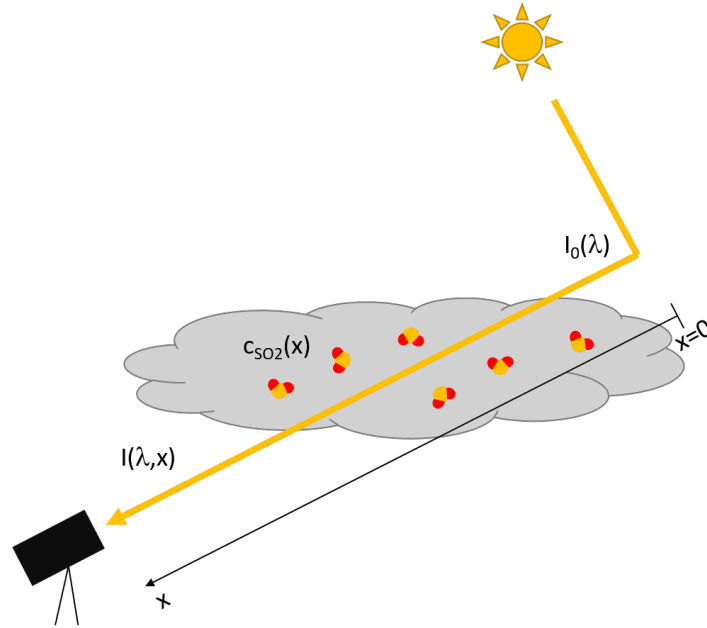


Fig. (3.1) Measurement principle of atmospheric optical absorption spectroscopy. The incident radiation from the light source (here backscattered sunlight) is altered by the gases and particles in the atmosphere.

Besides the wavelength-selective absorption of incident radiation, the radiation can decrease due to several scattering processes in the atmosphere. Elastic scattering of photons out of the light beam by air molecules (much smaller than the wavelength of the incident radiation) is described by Rayleigh scattering. The extinction due to Rayleigh scattering $\epsilon_R(\lambda, x)$ is approximately proportional to λ^{-4} . A small part of the photons (2-4%) is scattered inelastically and hence changes its wavelength (Raman scattering). The Mie theory describes the scattering of electromagnetic waves on homogeneous spheres and can be used to approximate the scattering on particles of comparable size as the scattering light (e.g. water droplets, ash particles, aerosol,...). The size of the particles are described with the dimensionless size parameter $x = \frac{2\pi r}{\lambda}$ with the particle radius r . The Mie extinction coefficient $\epsilon_M(\lambda) = \epsilon_{M,0}\lambda^{-\alpha}$ depends i.a. on the size of the particles which is described by the Ångström coefficient α . The Ångström coefficient for atmospheric particles is circa 1.3 leading to a weak wavelength-dependency of Mie scattering [Roedel and Wagner, 2011]. Eq. 3.3 is extended to include scattering

$$\tau(\lambda) = - \sum_i^N \sigma_i(\lambda) \cdot S_i \cdot c_i(x) - \int_0^L \epsilon_R(\lambda, x) + \epsilon_M(\lambda, x) dx. \quad (3.5)$$

Here, multiple scattering, which is the process of photons being re-scattered into the light beam after being scattered out, is neglected.

Atmospheric optical absorption spectroscopy instruments estimate the optical density by measuring spectra or single wavelength bands of the radiation before and after passing through the volume which should be studied. Depending on the type of instrument, the

spectral information is used to relate the optical density to the slant column densities. In the ultraviolet and visible spectral range, differential optical absorption spectroscopy (DOAS) [e.g. Platt and Stutz, 2008] is a popular method for measuring the slant column densities of many absorbers simultaneously with high accuracy. It exploits the narrow absorption bands of the absorption cross sections by separating the measured spectrum in narrowband and broadband contributions and thereby isolates the absorption from the scattering processes. The DOAS technique is used as absolute calibration for other instruments as e.g. SO₂ cameras.

3.2 SO₂ cameras

SO₂ cameras were originally developed for measuring volcanic sulfur dioxide (SO₂) emission rates [Mori and Burton, 2006; Bluth et al., 2007]. SO₂ is a toxic gas which affects both local ecosystems around emission sources as well as global climate due to its cooling effect and long lifetimes in the stratosphere. Further, at volcanic systems, changes in SO₂ emissions are linked to volcanic activity and can be a proxy to predict future eruptions (see e.g. Oppenheimer et al. [2013]). Therefore, continuous monitoring of SO₂ emissions has become important over the last few decades. Both in-situ sensors [e.g. Shinohara, 2005] and ground- or space-borne remote sensing techniques have been exploited [see e.g. Galle et al., 2010; Fioletov et al., 2016; Carn et al., 2017; Platt et al., 2018]. On the ground, SO₂ fluxes have been measured remotely by correlation spectrometers (COSPEC, [Stoiber et al., 1983]) since the 70s and by MAX-DOAS instruments routinely since the early 2000s [e.g. Edner et al., 1994; Bobrowski et al., 2007]. Both instrument types collect all radiation within a single solid angle ("one-pixel" detector) and scan through the plume to get a vertical cross section of the SO₂ distribution which can be multiplied by the wind speed to receive the SO₂ emission rate. This leads to a limited temporal resolution of few minutes. The techniques are well-suited for long-term monitoring. For instance Max-DOAS instruments are used in the network for volcanic and atmospheric change (NOVAC)[Galle et al., 2010] due to their high accuracy despite their autonomy and robustness. However, fast or local changes in the emission rates cannot be detected. Imaging-DOAS instruments [Louban et al., 2009] can resolve the two-dimensional distribution but nevertheless lack the temporal resolution.

By using a two-dimensional sensor, SO₂ cameras capture images of the plume and clear sky (Fig. 3.2) and hence provide both high spatial and temporal resolution in the order of few Hertz [Mori and Burton, 2006]. Figure 3.3 shows an example image of volcanic SO₂ SCDs which can be retrieved from the images (see section 3.3). In comparison to classical absorption spectroscopy applications in which the full spectrum is resolved, the SO₂ camera has a simpler approach: The light absorption due to SO₂ is measured in a narrow wavelength region where SO₂ is highly absorbing (typically around 310 nm) using a UV-sensitive CCD detector placed behind a band-pass interference filter [Bluth et al., 2007]. The broadband influence of aerosols and water droplets on the measured optical density can be corrected by using a second filter centred at a wavelength around 330 nm where SO₂ absorption is negligible [Mori and Burton, 2006; Kern et al., 2010]. Figure 3.4 shows the absorption cross section of SO₂ in comparison to the wavelength ranges of the two filters. SO₂ camera systems deploy either a single UV-sensitive camera and a filter wheel or two UV-sensitive cameras with one filter placed in front of each CCD detector. Double camera systems are preferable when high temporal resolution is needed but require

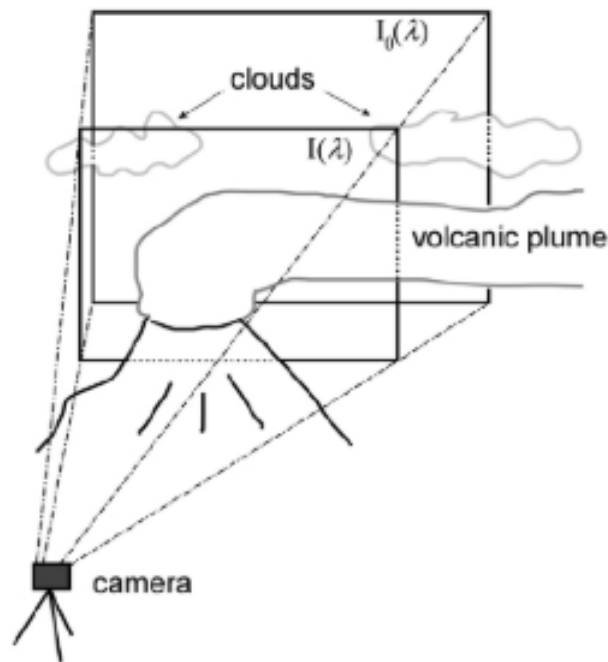


Fig. (3.2) Typical measurement geometry of a SO_2 camera. Images of the radiation $I(\lambda)$ containing both plume and clear sky are recorded. The background intensity $I_0(\lambda)$ behind the plume has to be estimated from the clear sky areas or from an additional SO_2 -free image. Reproduced from Kern et al. [2010], Fig.2.

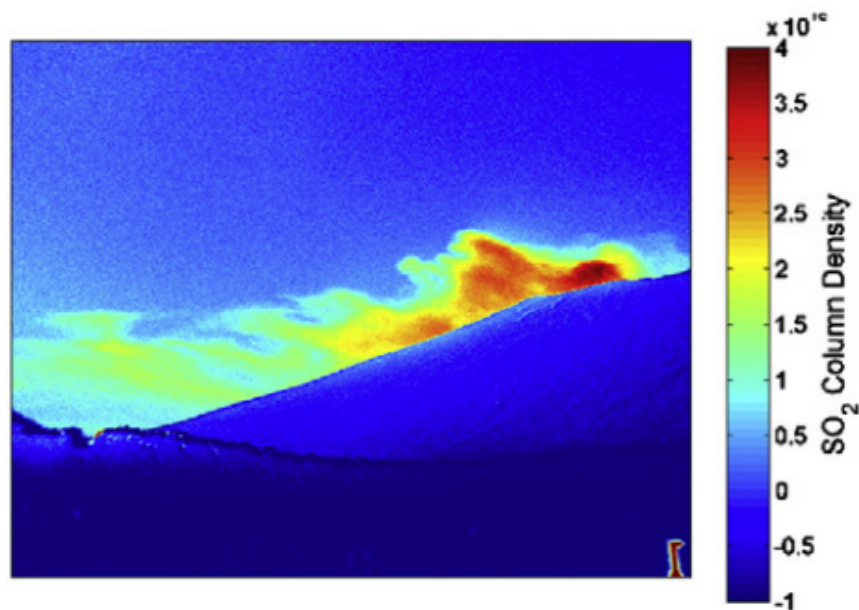


Fig. (3.3) Typical image of volcanic SO_2 emission from a SO_2 camera at Popocatepetl, Mexico. Adapted from Platt et al. [2015], Fig.12.

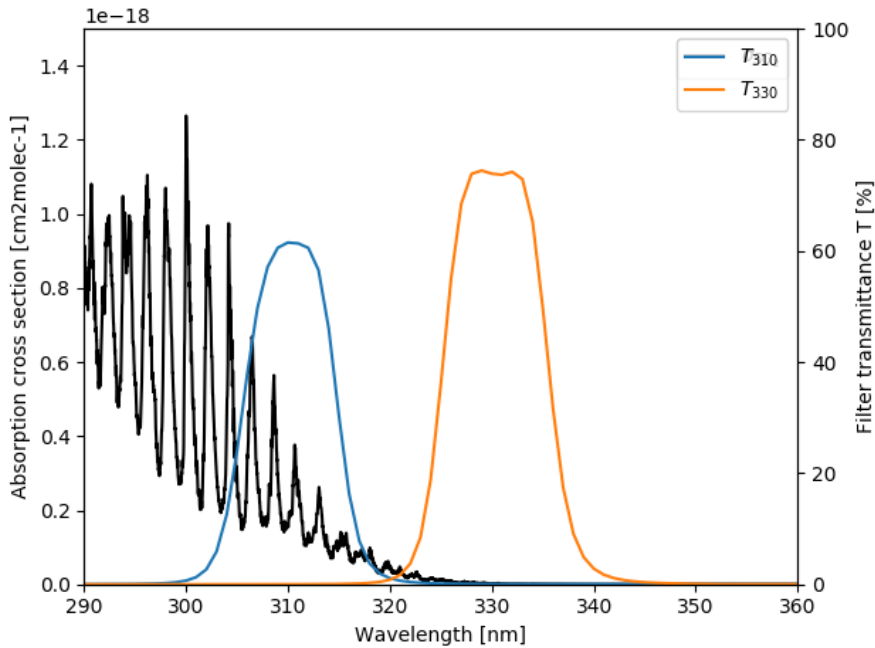


Fig. (3.4) Measurement principle of the two-filter SO₂ camera. The intensity of backscattered sun light is sampled at two wavelength windows in which SO₂ is absorbing strongly and weakly, respectively. The intensity measured in the second wavelength window is used to correct for broadband extinction from ash or aerosol particles in the plume.

a correction of parallax when imaging objects at close distance. Most SO₂ cameras contain a spectrometer for absolute calibration of the SO₂ column densities using the DOAS method. In the last decade, the technique has seen major improvements [see e.g. Platt et al., 2018, for an overview] and SO₂ cameras have been used for measuring emissions from anthropogenic and natural sources: single and multiple volcanic plumes [e.g. Burton et al., 2015; Stebel et al., 2014; D’Aleo et al., 2016], power plants [Marmureanu et al., 2013; Smekens et al., 2015] and ships [Prata, 2014]. Nowadays, SO₂ flux measurements with SO₂ cameras are a well-established method and have been used to study a variety of fast volcanic degassing processes [e.g. McGonigle et al., 2017]. Recent developments further explore an alternative wavelength region in the thermal infrared [Prata and Bernardo, 2014] or use a Fabry-Perot interferometer [Kuhn et al., 2014, 2019].

3.3 SO₂ column density retrieval

A good overview of different approaches to retrieve SO₂ emission rates from UV cameras is given by Kantzas et al. [2010] and many routines are implemented in the open source software pyplis [Gliß et al., 2017] with additional information on how they should be used. Parts of the software developed in this thesis was implemented within pyplis, while the code for the statistical analysis of turbulent dispersion builds on top of it.

3.3.1 Sensor effects

The SO₂ camera records intensity images integrated over the narrow-wavelength region of the bandpass filter with transmittance $T(\lambda)$. Additionally, the camera sensor has a wavelength dependent quantum efficiency $Q(\lambda)$ and a dark signal $I_{dark}(i, j)$ due to thermally excited electrons in the semiconductor and the electronic offset of the amplifier. The measured intensity in a pixel (i, j) becomes

$$I(i, j) = \int_0^{\infty} T(\lambda)Q(\lambda)I(\lambda, i, j)d\lambda + I_{dark}(i, j). \quad (3.6)$$

The dark signal can be measured by covering the camera with a black cloth. The optical density $\tau(i, j)$ for a wavelength band can be calculated

$$\tau(i, j) = -\ln \frac{I(i, j) - I_{dark}(i, j)}{I_0(i, j) - I_{dark}(i, j)} \quad (3.7)$$

where $I_0(i, j)$ is an image of the same scene with no SO₂ present.

3.3.2 Background radiation

The background radiation changes throughout the day as the light paths through the atmosphere change with the movement of sun and the atmospheric aerosol load. Further, the radiation strongly depends on the viewing direction. For practical reasons, it is not possible to measure the incident radiation before and after passing through the plume simultaneously (see Fig. 3.2). Therefore, it is necessary to estimate the incident radiation from an image which typically was recorded before or after the plume measurement and towards a different azimuth or elevation angle where no SO₂ is present. To compensate for the difference in the real and measured $I_0(i, j)$, the average values in a image region or along pixel rows/columns which are free of SO₂ in both $I(i, j)$ and $I_0(i, j)$ are compared and pixel-wise scaling, intra- or extrapolation is applied to $I_0(i, j)$ before calculating the optical density according to Eq. 3.7. Gliß et al. [2017] discuss several methods and the optimal method depends on the individual measurement geometry. While the estimate of the incident radiation gives reasonable good results for clear sky areas, scattered, inhomogeneous clouds cannot be accounted for as they scale differently than the blue sky [Kern et al., 2010] and move rapidly. They will often lead to a signal in the same order of magnitude as the SO₂ column densities. Despite efforts to correct for cloud cover [Osorio et al., 2017], accurate SO₂ camera measurements are generally limited to clear sky observations.

3.3.3 Correction of broadband scattering and absorption

The optical density for both wavelength channels are calculated independently according to Eq. 3.7. The two wavelength channels are often called "on-band" and "off-band" because their wavelength regions are located on or besides ("off") the absorption bands of SO₂; here "on" refers to the channel at 310 nm and "off" to the one at 330 nm. To correct for aerosol in the plume, the apparent absorbance is the differential optical density ascribed only to absorption of SO₂ and is calculated as

$$\tau_{AA} = \tau_{on} - \tau_{off} = -\ln \frac{I_{on}}{I_{on,0}} + \ln \frac{I_{off}}{I_{off,0}} \quad (3.8)$$

When a two-camera SO₂ camera system is used, the field of views of the two cameras are shifted and a pixelwise-translation of the images might be necessary before applying Eq. 3.8 to avoid artefacts.

3.3.4 Radiative transfer

Radiative transfer effects can cause large errors for instance for large distances to the plume or optically thick plumes [e.g. Kern et al., 2013; Campion et al., 2015]. On one hand, multiple scattering inside the plume extends the light path over the geometric thickness of the plume. If this extension cannot be quantified, the SO₂ columns will be overestimated. On the other hand, additional photons which get scattered into the solid angle of a pixel between the SO₂ plume and camera lead to a higher intensity and hence underestimated SO₂. This effect is commonly denoted as "light dilution". Campion et al. [2015] propose a correction method for the measured intensities to estimate the atmospheric scattering coefficients from the images. Generally, the uncertainties due to radiative transfer effects become more prominent with larger distances to the source and high aerosol load in both the plume and background atmosphere.

3.3.5 Calibration

While the absorption cross section of SO₂ is known with high resolution from laboratory studies [e.g. Vandaele et al., 2009], the wavelength-dependencies of the filter transmittance curve $T(\lambda)$ and the detector quantum efficiency $Q(\lambda)$ are generally less known. To overcome this, an absolute calibration from optical densities to slant column densities is required. This can be done by either recording images of gas cells filled with a known amount of SO₂ or by measuring the absolute SO₂ column density simultaneously with, for instance, a DOAS instrument, which samples a small area of the total image within the field of view of the camera [Lübcke et al., 2013]. From a linear fit, the calibration constant $a(i, j)$ of the camera is estimated. The images are then scaled to SO₂ slant column densities

$$S(i, j) = a(i, j) \cdot \tau_{AA}(i, j). \quad (3.9)$$

The obtained SO₂ slant column densities $S(i, j)$ are a projection of the SO₂ concentration distribution to the image plane.

For optical thick plumes (large aerosol load or high SO₂ SCDs), this simple picture fails and radiative transfer calculations are necessary to obtain a calibration curve. Kern et al. [2013] simulated calibration curves for different aerosol optical thicknesses and concludes that deviation from the linear relation starts at SO₂ columns of 2000 ppm m. Dalton et al. [2009] reported a linear relation up to SO₂ columns of 1500 ppm m and a logarithmic curve above this value based on SO₂ cells measurements. A second order polynomial calibration curve was estimated by Huret et al. [2019] from comparing UV and IR SO₂ camera measurements.

3.3.6 SO₂ flux estimation

For monitoring purposes, the emission flux of SO₂ from a natural or anthropogenic point source (e.g. volcano, power plant, ship,...) is of high interest. This thesis does not contain flux estimations but fluxes could be in principle estimated for the plume releases. The flux ϕ can be estimated when the propagation velocity $v(i, j)$ and the orientation of the plume

to the camera is known. The flux is then calculated as the integrated column densities along the pixels of a plume-cross section L in the image.

$$\phi = \sum_{i,j \text{ on } L} v(i, j) \cdot S(i, j) \cdot \Delta s(i, j) \quad (3.10)$$

with the apparent pixel size $\Delta s(i, j)$ at the plume distance. The velocity can be directly estimated from a stream of SO_2 camera images using cross-correlation [McGonigle et al., 2005; Mori and Burton, 2006] or optical flow methods [e.g. Peters et al., 2015; Gliš et al., 2018]. The distance to the plume, and hence the apparent pixel size, is typically approximated with the geometric distance to the source. The orientation of the plume to the camera’s viewing direction affects the observed plume velocity and pixel size. These two effects are often assumed to cancel out [Mori and Burton, 2006]. However, Klein et al. [2017] showed that this assumption can easily cause errors larger than 10% and proposed a method for estimating the direction of single plumes from the images.

3.4 Tomography of atmospheric SO_2 distributions

The primary result from SO_2 cameras are two-dimensional (2D) images of the SO_2 column densities. Using several 2D images from different directions allows for reconstructing three-dimensional (3D) properties of the SO_2 distribution, from macroscopic properties as e.g. centre line and shape up to a full tomography of the in-plume concentrations. Gas concentrations are critical for chemical reactions inside the plume but can also be used to study the plume dispersion when combined with the temporal dimension available in the camera measurements.

The absorption of UV radiation by SO_2 molecules is equivalent to the absorption of X-rays by organic tissue. Computed tomography (CT) is nowadays a standard method in medicine. The light source and detector rotate around the object and hence produce few hundred images of the object from different directions. While, in principle, the same mathematical framework can be used for atmospheric applications, studies have to face several challenges: (1) Instruments (imagers or scanning methods) can typically be placed only at certain spots on ground level due to topography and/or road access although airborne studies (plane, satellite) are possible as well. (2) The gas concentration distribution is typically not constant and undergoes atmospheric transport and dispersion. Viewing directions need to be recorded at approximately the same time. Due to these challenges, few tomographic studies have been reported in the past, mostly using active longpath DOAS [Hartl et al., 2006], airborne traverses [Kazahaya et al., 2008] or scanning DOAS [Wright et al., 2008; Johansson et al., 2009] methods. Recently, Wood et al. [2019] used a space carving method to reconstruct the plume shape of the volcano Fuego from a data set of four thermal infrared cameras.

3.5 COMTESSA SO_2 cameras

For realising the COMTESSA project, a set of nearly identical SO_2 cameras was required. To enable the resolution of the fast number of temporal and spatial scales involved in turbulent dispersion, the main requirement for the COMTESSA cameras were high resolution in time and space. Such a system was not readily available on the market. Therefore, the

SO₂ cameras were custom-built for the COMTESSA project. An image of the full system is shown in Fig. 3.5. The camera properties and components are summarised in table 3.1 and depicted in Fig. 3.6.



Fig. (3.5) Image of a COMTESSA SO₂ camera. The cameras run autonomously with the dedicated computer but a remote desktop connection is required to access the computer.

The following paragraph is adapted from Dinger et al. [2018]. At the core of each SO₂ camera are two UV cameras from PCO (pco.ultraviolet), which record images in two different wavelength regimes. The cameras' CCD sensors have 1392 pixel columns and 1040 pixel rows with quadratic pixels of size $4.65\ \mu\text{m}$. The wavelengths are selected by mounting two Asahi Spectra band-pass filters (10 nm bandwidth) at 310 and 330 nm between each of the CCD sensor and camera lens. This setup attenuates radial sensitivity changes due to different light paths through the filter for off-axis rays compared to mounting the filters in front of the lens [Kern et al., 2010]. The cameras can be equipped with two different quartz lenses with a focal length of either 25 mm or 12 mm depending on the desired field of view (FOV) and angular resolution. The lenses can be exchanged effortlessly in the field to adapt to the experimental setup. The 12 mm lenses have a FOV of $30.0^\circ \times 22.7^\circ$ and the 25 mm lenses have a FOV of $14.7^\circ \times 11.1^\circ$. Precise time synchronisation is assured by a GPS system. Additionally, a high resolution visible camera, an inclinometer and four temperature sensors are placed within the enclosure. Further, each camera contains an AvaSpec-ULS2048x64 spectrometer from Avantes for robust SO₂-calibration. The spectrometer is coupled via a $3 \times 200\ \mu\text{m}$ cross section converter fibre from Loptek to a telescope, pointing in the same direction as the UV cameras. The telescope consists of a quartz lens from Thorlabs with 100mm focal length and a Hoya U-330 filter which prevents stray light to enter the detector. This setup results in a telescope field of view of 0.572° which corresponds to a disk with a 52-pixel diameter within the UV camera image for the 25 mm-lens. The spectrometer is operated automatically with a measurement script for the software DOASIS [Kraus, 2006], while the rest of the camera hardware is operated with a custom software.

For each SO₂ camera, an additional box containing the power supply (both 12V-DC and AC) and a computer was manufactured. The computer (MXC-6301D/M16G(G) from

Table (3.1) COMTESSA SO₂ camera specifications

UV cameras	Camera model	PCO.ultraviolet
	CCD sensor	Sony ICX407BLA
	Pixel $P_H \times P_V$	1392 × 1040 pixel
	Sensor size $D_H \times D_V$	6.47 mm × 4.84 mm
	Sensor quantum efficiency	ca. 30 % at $\lambda=300$ nm
	ADC bit depth	14 bits
	Sensor temperature	ambient
	Shutter type	electronic, global
	Interface	USB2.0
	Maximum frame rate	7.3 Hz (full resolution)
Bandpass filters	Filter manufacturer	Asahi Spectra
	Filter model channel A	XBPA310
	Filter model channel B	XBPA330
	Wavelength channel A	310 nm
	Wavelength channel B	330 nm
Optical lens 1	Object lens	Universe Kogaku UV2528B
	Object lens focal length	25.04 mm at $\lambda=266$ nm
	Field of view $W \times H$	14.7° × 11.1°
	Aperture	f/2.8, f/4, f/5.6, f/8, f/11, f/16
	Distortion	-4.05 %
Optical lens 2	Object lens	Universe Kogaku UV1228CM
	Object lens focal length	12.08 mm at $\lambda=250$ nm
	Field of view $W \times H$	30.0° × 22.7°
	Aperture	f/2.8 to f/16 (smooth)
	Distortion	-6.8 %
Spectrometer	Collocated spectrometer	Avantes AvaSpec-ULS2048 × 64
	Filter	Hoya U330
	Optical fibre	Loptek 3x200 μ m
	Spectrometer field of view	0.572°
	Spectrometer temp control	no
Other parts	Visual camera	Basler acA3800-10gm
	GPS	MR-350PS4
	Inclinometer	ACA626T-30-232
	4 temperature sensors	custom-made
Physical properties	Dimensions, camera	21.5 cm × 21.5 cm × 29 cm
	Dimensions, PC box	28 cm × 25 cm × 45 cm
	Weight	21 kg

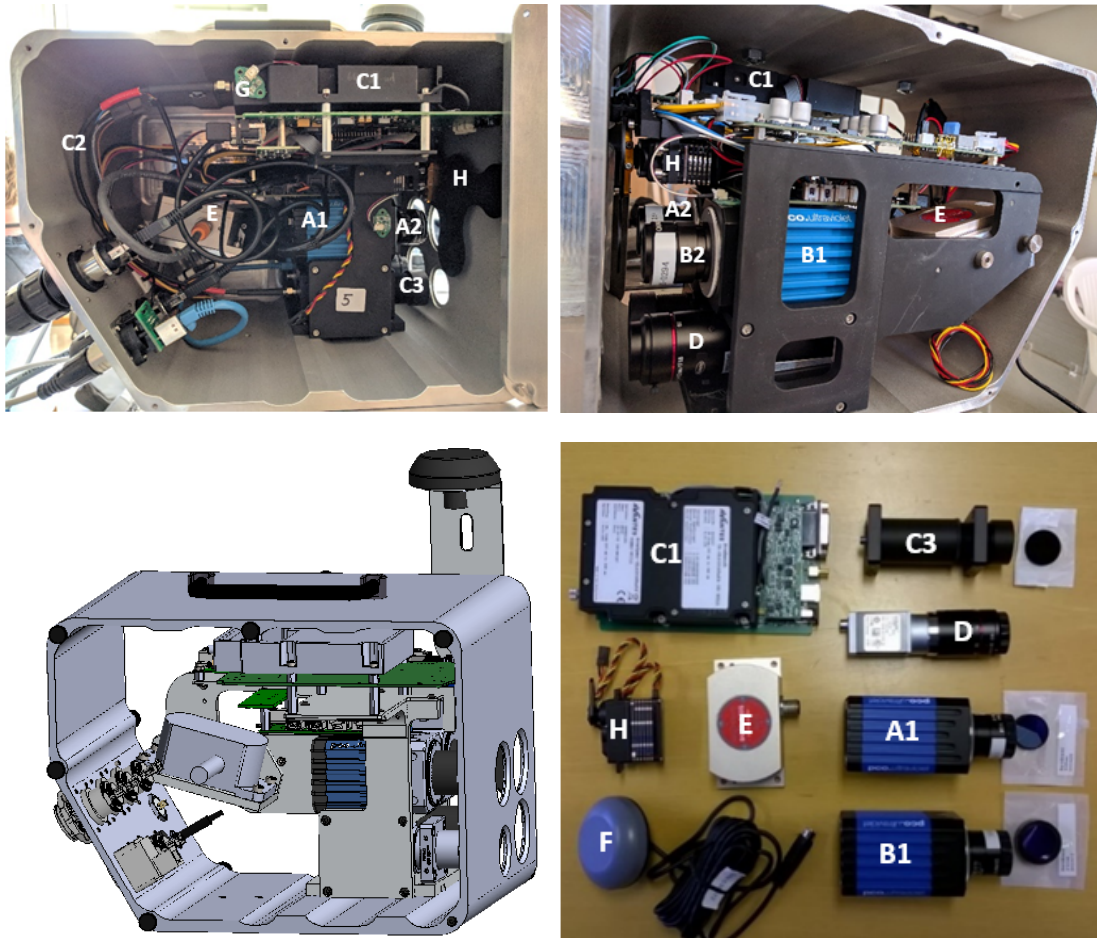


Fig. (3.6) Internal view of COMTESSA cameras: pco.ultraviolet cameras with lenses and filters (A and B), spectrometer with telescope (C), visual camera with lens (D), inclinometer (E), GPS (F), temperature sensors (G) and servo motor with shutter (H). Design drawing courtesy to C. Bernardo.

ADLINK Technology Inc) with 16 GB RAM was equipped with a 1 TB internal hard disc enabling an autonomous and smooth operation of the cameras. During the COMTESSA experiments, the cameras operated mostly at frame rates of circa 5 Hz (exposure times between 150-250 ms). At this rate, one camera produced circa 2 GB of image data per minute when operated at full resolution. In this case, the cameras could record images for circa 8 h continuously before a data backup was necessary.

All six cameras use the same hardware components. Nevertheless, the manufacturing process led to small differences in the characteristics of the components which have consequences for e.g. SO_2 sensitivity, image distortion or time resolution. For instance, Figure 3.7 shows the filter transmittance curves of the six COMTESSA cameras. The filter transmittance of camera UV6 is slightly lower than for the other cameras at lower wavelengths where SO_2 absorption is strongest leading to a lower overall SO_2 sensitivity.

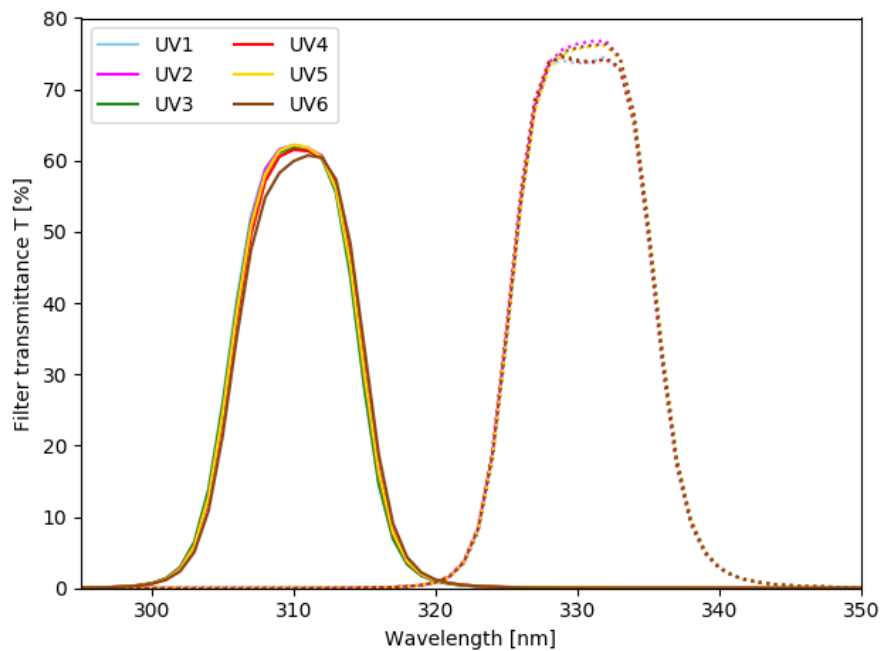


Fig. (3.7) Filter transmittance curves for the six XBPA310 (solid) and six XBPA330 (dashed) filters used inside the six COMTESSA cameras as measured by the manufacturer.

Chapter 4

The COMTESSA tracer dispersion experiments

Three measurement campaigns were performed in July 2017, July 2018 and July 2019 on the same experimental site in Norway. Sulfur dioxide (SO_2) was released in controlled experiments from a tower and its dispersion was observed by SO_2 cameras. In the course of the three years, the measurement procedures were further developed. In the following, the technical aspects of the tracer release and the measurements of all three campaigns are described while chapter 5 will describe the obtained data set.

4.1 Experimental site and instrumentation

The artificial release campaigns were performed at the military training ground Regionalfelt Østlandet (11.5°E , 61.4°N) about 28 km northeast of the small city of Rena, Norway. The experimental site is located in a remote forested mountain area at an altitude of 850 m above sea level. It is a fenced-in flat gravel field with dimensions of about $900\text{ m} \times 400\text{ m}$, which is normally used for ammunition testing by the Norwegian military. A road goes along the fence which allows the placement of the cameras on the road increasing the usable area to $1\text{ km} \times 1.5\text{ km}$. The surrounding area is parts forest, parts swamp.



Fig. (4.1) Experimental site: Terrain map and satellite image from Kartverket Norge and image of the site during the field campaign 2018

The release tower was mounted in the middle of the gravel field at the beginning of each campaign and remained fixed for the entire 3-weeks period of the individual campaigns. In 2017, the tower was 9 m height and in 2018 and 2019, a 60 m tall tower was used. Two additional masts of 10 m height were available of which one was placed on the gravel field

to get better representation of the state of the surface layer. In 2017, the second auxiliary mast was placed outside the gravel field to characterise the differences of the surface layer on the gravel field and on the swamp. In the following years, the instruments on the second mast were used on the higher release tower instead and the mast was not placed at all. The cameras were placed around the release tower both on the gravel field and along the ring road at varying positions during the campaigns.

At the northernmost end of the experimental site, a meteorological tower (Rena-Ørnhaugen, station number 7420, WMO number 01388) is operated on a small hill by the Norwegian Meteorological Institute. Along the forest road, three permanent towers exist which can be seen clearly from the gravel field and are present in images from some cameras.

4.1.1 Instrumentation

Turbulent flow

The meteorological conditions and turbulent fluxes of momentum, heat, moisture and CO₂ were recorded using a state-of-the-art measuring system from Campbell Scientific. A total of seven measurement units were attached at different height levels along the release mast and secondary masts. Each unit included a sonic anemometer (model CSAT3A or CSAT3B) for measuring the three wind velocity components and sonic temperature with 50 Hz sampling frequency. Additionally, an EC150 gas analyser was coupled to the lowest height level of the release tower. It measured simultaneously water vapour and carbon dioxide densities at 50 Hz. Low response sensors measured the atmospheric pressure and temperature at lower frequency.

The placement of the levels along the masts were chosen such that it represents the logarithmic wind profile close to the ground. In 2017, the flow was sampled at three levels along the release mast and at two levels at both of the the additional masts. In 2018 and 2019, five levels were used at the significantly higher release mast and two levels at one additional 10 m-mast placed at a distance of circa 150 m from the release tower. The exact height above ground of the levels are listed in table 4.1.

Table (4.1) EC measurement level heights at the release tower

	2017	2018	2019
Main tower			
1st level	2.0 m	2.0 m	2.0 m
2nd level	5.4 m	5.0 m	5.0 m
3rd level	8.7 m	10.4 m	10.4 m
4th level	-	31.9 m	32.0 m
5th level	-	60.2 m	60.2 m
release, plume	9.0 m	60.8 m	60.8 m
release, puffs	9.0 m	60.8 m	55.3/57.3 m
Add. tower(s)			
1st level	2.0 m	1.0 m	1.0 m
2nd level	8.8 m	9.0 m	9.0 m

SO₂ cameras

The technical details of the COMTESSA SO₂ cameras were described in section 3.5. During the first measurement campaign in 2017, the cameras were equipped with the 25 mm-lenses and the apertures were fixed to f/2.8 (on-band) and f/5.6 (off-band). The aperture of the off-band camera was decreased in order to achieve similar exposure times. In consequence, the off-band images have a larger depth of field and appear sharper. During the following two campaigns in 2018 and 2019, a larger field of view (FOV) was desired for observing the release for longer times. Therefore, the cameras were equipped with the 12 mm-lenses. The aperture of the on-band camera was again fully open (f/2.8) while the aperture of the off-band camera was set such that the exposure times during noon time were similar.

The cameras were operated semi-autonomous. The exposure times were manually adjusted such that the 14-bit-sensor was roughly 70-90 % saturated. Usually, an adjustment at least once per hour was necessary to compensate the changing light conditions. Dark images, gas cell calibration measurements, as well as calibration of the built-in spectrometer were performed regularly.

At some spots of the experimental site, AC power was available. When a camera was placed close to such a spot, it was run on AC. Otherwise, 12 V car batteries were used for power supply. The cameras were mounted on tripods (Benro A-458M8) with full-control ballheads (Benro B3 Triple Action) which were extended to 75 cm or 110 cm above ground.

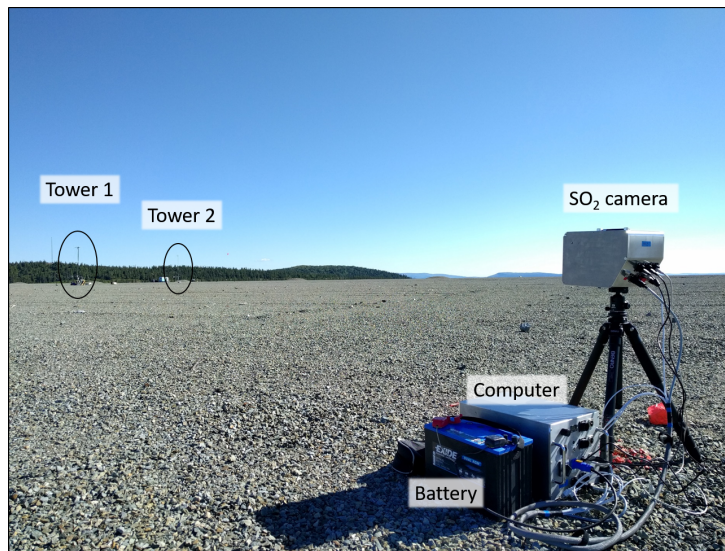


Fig. (4.2) Image of COMTESSA SO₂ camera during the 2017 campaign with the release tower in the background. Reproduced from Dinger et al. [2018]

4.1.2 Camera geometry

Release experiments were carried out with different configurations of the camera positions. See Fig. 4.3 for an overview. Both a high pixel resolution and a large field of view (FOV) are desired to resolve a wide range of turbulent scales. However, these depend contrary on the distance between the camera and the object (plume/puffs): Increasing distance leads to a large FOV but low pixel resolution. Table 4.2 gives values for a set of exemplary distances. The cameras were initially placed at a distance that compromises resolution and FOV. In the course of the project, it became obvious that a large FOV is required

to observe the SO_2 gas for a sufficient long time (see chapter 7). Therefore, the cameras were placed at a distance up to 1200 m from the tower in 2019 compared to circa 500 m in 2018 and up to 190 m in 2017. Additionally, the lenses were exchanged in 2018 to obtain a larger FOV. For practical purposes, only positions on the gravel field, on the dirt road along the fence and the regular forest roads could be considered. The topography in the fore- and background and the position of the sun put additional constraints to the camera placement and required partly that the cameras' positions were changed depending on the expected wind direction and time of day. At the same time, the half-circle configuration appeared to be most useful for the planned tomographic reconstruction as it covers both perpendicular and frontal direction.

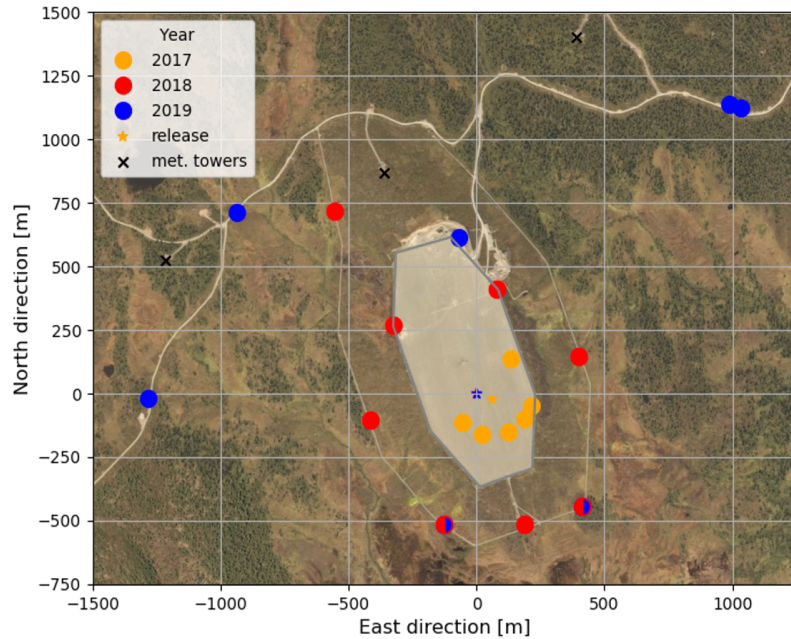


Fig. (4.3) Overview map of the camera positions used during all three campaigns. The cameras were moved further away from the release to increase the FOV. Few additional positions closer than 100 m were used in 2017 and 2018 which are not displayed here due to visibility.

Table (4.2) Resolution and FOV of the two lens types for various object distances

Lens		object distance		
		100 m	500 m	1000 m
UV2528B (f=25 mm)	pixel resolution [cm]	1.9	9.3	18.5
	FOV [m × m]	26 × 19	129 × 96	257 × 192
UV1228CM (f=12 mm)	pixel resolution [cm]	3.9	19.3	38.5
	FOV [m × m]	54 × 40	269 × 203	536 × 400

The positions of the cameras were not changed during the course of a measurement day. However, the pose of the cameras (azimuth and elevation angle) was adjusted regularly

during the experiments to adapt the cameras' field of view to changing wind direction. If possible, the releases should be observed in the centre of the field of view where camera vignetting and distortion effects are small.

Position measurement

In 2017, the software controlling the GPS acquisition was not operational yet. Instead, the distances and relative angles of the cameras to the release tower as placed on 15 and 20 July 2017 were measured manually by tape and a theodolite respectively. Using trigonometry, the relative positions were reconstructed. The absolute position is based on the Garmin GPS of the measurement station at the release tower. Additionally all positions were measured with the GPS sensor of a consumer grade smart phone. Comparing the values from different smart phones, an error of at least 2 m can be assumed.

From 2018 on, the built-in GPS logged during all measurements detailed messages in the SiRF binary protocol which can be used for post-processing. For fast processing purposes, the positions were additionally measured with a real time kinematics (RTK) base-rover solution from ublox (C94-M8P). The solution consisted of two GPS modules with an integrated radio link and reached centimetre-accuracies for relative positions. For some positions, the radio link was not sufficient and accuracies reached 15-20 cm.

Considering a tomographic reconstruction, the error of each pixel direction is directly given by the same uncertainty as the position. Depending on the distance between camera and object, the pixel resolution is given in table 4.2. For 2018 and 2019, the uncertainty of the position is below the pixel resolution of the cameras.

Pose reconstruction

The azimuth, elevation and tilt (roll) of the cameras were reconstructed from the images. Previous studies [Gliß et al., 2017; Wood et al., 2019] used detailed models of the background topography to reconstruct the viewing direction of a SO₂ camera. No such detailed map data was available for the experimental site which in addition to the lack of distinct topographic features (e.g. a volcanic crater area) did not allow for this approach. Instead, the top of the release tower was visible in all images. Comparing its pixel position with the measured GPS position, the azimuth and elevation angles of the cameras are extracted (see appendix A.1 for details). The cameras were adjusted with a water spirit level such that the tilt could be neglected in first approximation. For some directions, the meteorological towers to the north of the release are visible as well. Due to the large distance to the cameras (2 km) compared to the release tower, it can be preferable to use the less accurate position of the meteorological towers from satellite images, for example Kartverket Norge for the calculation of the azimuth angle. For these cameras, the azimuth angles showed general good agreement with a maximum measured difference of 0.3°.

It is obvious that the accuracy of the pose reconstruction depends largely on the accuracy of the positions of the camera and the top of the release tower. The uncertainty of the camera position can be neglected in comparison to the tower position. The 60 m-tower is not completely straight as it consists of single 2 m-conjunction pieces and was straightened and kept in place by metal wires. An uncertainty of the position of the tower top of 1 m was estimated from the tower setup. In 2018, the cameras were placed at distance of approximately 500 m leading to a resulting uncertainty of circa 5 pixels. This results in a uncertainty of the azimuth and elevation angle of 0.1°.

4.2 Passive tracer release

The release equipment and procedure were developed by Norbert Schmidbauer from NILU and 2-3 people were required for performing the release.

4.2.1 Sulfur dioxide as passive tracer

Atmospheric sulfur dioxide is comparably easy to measure remotely due to negligible background concentrations and its specific absorption lines in the ultraviolet and infrared spectral range as discussed in chapter 3. Additionally, SO₂ has been a frequent choice as passive tracer for atmospheric dispersion experiments due to its chemical and physical properties.

Sulfur dioxide is chemically inert on the time scales relevant to the COMTESSA experiments. SO₂ is removed from the atmosphere by dry and wet depositions and conversion to sulphuric acid. Depending on aerosol load, the lifetime of atmospheric SO₂ has been reported to few hours to few days [Lee et al., 2011; Fioletov et al., 2015]. In comparison to the observation duration of few minutes, the total released SO₂ mass can therefore be assumed to be conserved.

Further, SO₂ has a molecular weight of 64.066 g mole⁻¹ and is therefore more than two times heavier than air (28.97 g mole⁻¹ on average). However, dilution with ambient air before the release reduces the effect of a heavy gas and it can be assumed that the SO₂ is passively advected by the surrounding air.

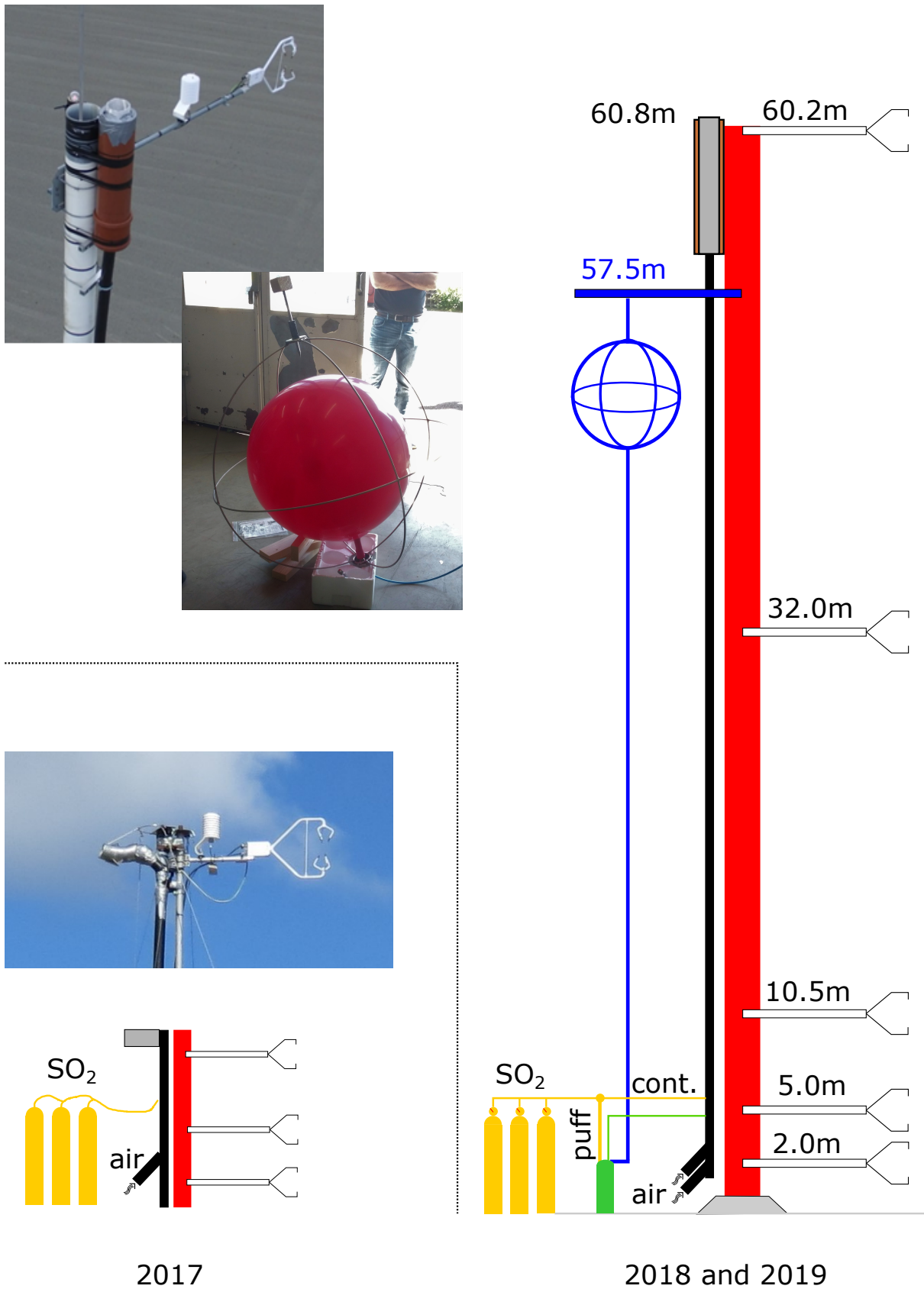
For tracer experiments, releasing SO₂ gas rather than smoke or manufactured particles has the advantage that the optical densities measured by the SO₂ cameras can be directly linked to column-integrated concentration via the Beer-Lambert-Bouguer law (Eq. 3.1), and thus allowing for a quantitative observation.

The release of SO₂ for tracer experiments has one main disadvantage: SO₂ is toxic and can be lethal for humans in high concentrations as well as catastrophic to ecosystems. Therefore, careful security measures, connected to logistic efforts, have to be taken into account when planning the experiment and deliberate emissions have to be made in accordance with national environment agencies.

4.2.2 Release equipment

The SO₂ was released from the top of a tower. Figure 4.4 shows a sketch of the setup. In 2017, the tower was approximately 9 m high, and in 2018 and 2019 a 60 m high meteorological tower was used. The gas was transported to the top through a PVC pipe with 7 cm diameter. The end piece merged into a slightly larger aluminium rod (12.5 cm diameter). The larger, final diameter decelerated the gas rising inside the pipe and ensured a passive release. Nevertheless, the release might have caused a small jet flow around the outlet. In the 2017 campaign, the outlet was bend horizontally and could be mechanically adjusted in wind direction. Hence, the gas was released horizontally into the atmospheric background flow. In the 2018 campaign, the final rod (length 78 cm) was fixed in a vertical position. The SO₂ was released above the tower and the measurement equipment which might have influenced the background flow.

The sulfur dioxide gas was provided in three gas bottles, each holding 65 kg of SO₂ and equipped with pressure regulating valves from Spectron Gas Control Systems GmbH. The gas bottles were placed on a scale and the weight was noted down at regular intervals



2017 2018 and 2019

Fig. (4.4) Sketch of release tower with positions of sonic anemometers and release pipe and image-inlets of the release. In 2019, the balloon cage and additional line (blue) was placed and the canister (green) was connected to the line instead of the pipe. Sketch is not to scale. (Image credits to H. Ardeshiri).



Fig. (4.5) Pictures of the gas bottle setup during the three campaigns. In 2017, one blower was used for both continuous and instantaneous releases while in 2018 and 2019, two blowers were used for the continuous releases and separate canisters were used for the instantaneous releases. (Image credits to H. Ardeshiri)

during the releases. Up to three gas bottles were simultaneously attached to the pipe. The gas was then released by opening the valves mechanically. In case of the 2018 puff releases, an additional canister was connected between the gas bottles and the pipe to improve the control over the release amount. Commercial blowers (STIHL SHE 71) were used to create an ambient air flow in the pipe and to dilute the SO_2 during the release. The blower velocity was set such that the release was nearly isokinetic. That was achieved by adjusting the flow in the pipe to the wind velocity monitored online with the sonic anemometer at the highest measurement level.

4.2.3 Continuous plume releases

The continuous releases were performed directly from the gas bottles with the same procedure during all three campaigns apart from smaller adjustments. The available valves limited the maximum continuous, combined flow rate from all bottles to 3.5 gs^{-1} . Due to the comparably small SO_2 concentration, most continuous releases were performed in 2017, when the cameras were placed closest to the release. In 2018, short and weak continuous releases were primarily used prior to puff releases to adjust the cameras' FOV to the wind direction. During the releases, the liquid SO_2 in the gas bottles vaporised leading to a decrease of in bottle temperature. Due to the lower temperature and hence lower equilibrium vapour pressure, less liquid vaporised causing a decrease of flow rate up to 8 % over the course of 40 min.

Table 4.3 gives an overview of all plume release experiments. The average release rates were calculated from the total released mass. For the low-rate adjustment plumes, no release rate estimate is available.

4.2.4 Instantaneous puff releases

For a statistical analysis, it is crucial that the puff releases are reproducible. Ideally, a constant mass of SO_2 is released instantaneously in a spherical, well-mixed volume. Due to the limited observation duration, it is additionally desirable that the puffs have a small initial source distribution which affects the relative dispersion for a short time (compare Eq. 2.22). However, also a high SO_2 mass is required to observe the SO_2 from large distances with the cameras. Further, the puffs should be released in short frequency to

Table (4.3) Plume release experiments

Date	UTC time	Duration [min]	SO ₂ flux [gs ⁻¹]
2017			
07/07	14:03 - 14:08	5	-
	14:28 - 14:39	11	0.5 ± 0.1
	15:00 - 15:19	19	0.5 ± 0.1
13/07	12:23 - 13:01	6×5	0.3 - 1.7*
14/07	09:43 - 10:15	3×10	1.7 ± 0.3
	12:07 - 12:28	2×10	1.75 ± 0.3
	12:41 - 13:27	4×10	1.8 ± 0.3
15/07	08:12 - 08:15	3	0.5 ± 0.1
	08:31 - 09:41	5×10	0.6 ± 0.1
	13:11 - 13:20	9	0.9 - 2.7**
	13:41 - 13:50	9	1.0 - 3.0**
19/07	14:21 - 14:38	17	1.2 ± 0.3***
	16:12 - 16:19	8	-
20/07	07:19 - 07:54	3×10	1.5 ± 0.3
	07:55 - 08:26	1×30	0.9 ± 0.3
	08:27 - 08:50	2×10	1.4 ± 0.3
	09:17 - 09:53	36	1.4 ± 0.3
	10:00 - 10:00	1	-
	10:06 - 10:19	13	-
	10:22 - 10:24	2	-
	10:48 - 11:10	22	1.6 ± 0.3
	13:46 - 14:03	17	1.9 ± 0.3
2018			
07/07	13:02 - 13:18	16	-
08/07	08:39 - 09:03	34	1.7 ± 0.3
	12:20 - 12:46	26	-
10/07	07:00 - 07:14	14	-
14/07	09:09 - 09:41	32	2 ± 0.3
	13:56 - 14:20	24	3.5 ± 0.3
15/07	07:11 - 07:52	41	2.5 ± 0.3
	14:14 - 14:30	16	3.0 ± 0.3
16/07	05:39 - 05:45	6	-
2019			
18/07	14:26 - 14:36	10	0.6 ± 0.1
26/07	07:05 - 07:27	22	2.5 ± 0.3

* variable

** increasing in three steps, release rates are estimated from total released mass

*** decreasing

ensure a large amount of puffs during comparable, ideally stationary conditions for the statistical analysis.

The release mechanism for nearly-instantaneous releases was improved in respect to these requirements. Initially in 2017, the puffs were directly released by opening a gas bottle for circa 1 s leading to a variable mass. The SO₂ gas needed 1-2s to be transported through the pipe where it was caught by the mean flow. The initial transport and diffusion caused an elongation of the SO₂ puffs in the pipe which was translated into cigar-shaped puffs. In 2018, an additional canister was used to control the released mass however the elongated shape persisted. In 2019, spherical puffs were achieved by replacing the pipe with instantaneously ruptured balloons.

2017

In 2017, the puffs were released analogous to the continuous releases by opening the directly-attached gas bottles. The mass of the individual puffs depended on the duration of the valve opening and the flow rate from each bottles which in turns depended on the bottles' temperatures and valves. Puff releases were limited to a single day. On 20 July 2017, ca. 210 puffs were released in high frequency with estimated SO₂ masses of (1.1 ± 0.2) g.

Table (4.4) Puff release experiments in 2017

Date	UTC time	SO ₂ mass [g]	puffs	interval
20/07	10:00 - 10:06	1.1 ± 0.2	40	5-10 s
	10:19 - 10:22	1.1 ± 0.2	40	5 s
	10:24 - 10:46	1.1 ± 0.2	130	10 s

2018

In 2018, an additional small canister was mounted between the gas bottles and the release pipe. The canister held 1 US gallon (3.78541l) ensuring a constant release volume. The canister was in thermal equilibrium with the environment. The pressure in the canister was recorded using a manometer before and after each release. The valve between the canister and the pipe was opened and closed manually. The canister was filled (release valve was closed) by opening the connection to the gas bottles. The filling process should be done as fast as possible and up to a constant pressure below the vapour pressure in the canister to avoid condensation.

Two release strategies were used: 1) The valve was opened and left open for a few seconds. 2) The valve was opened and immediately closed. Strategy 1) ensured that the total SO₂ in the canister was released and thus guaranteed a constant puff mass. However, if condensation took place during the filling of the canister, the pressure drop due to the release caused the condensed SO₂ to vaporise and be released with a delay. This in turn will produce a compact puff with trailing faint tail. Strategy 2) led to a smaller total release amount with small variation but without tails. Every 15 minutes, "cleaning puffs" were released to remove all condensed SO₂ from the canister. In this way, a nearly constant SO₂ mass of the puffs could be assured. Almost all puffs in 2018 were

released following strategy 1, except the last puff series on 16 July 2018 when strategy 2 was applied.

Table 4.5 gives an overview of the puff releases in 2018. The masses for 7, 8, 10 and 14 July were calculated as average mass from the total released SO₂ mass. An error of 25% is estimated for the single puff masses. On 15 and 16 July, the released mass per puff was calculated for each puff individually from the pressure in the canister before and after the release (for strategy 1 the remaining pressure is equal to the atmospheric pressure).

Table (4.5) Puff release experiments in 2018. The puff mass varied between releases of the same set. The mass uncertainty is ± 5 g until including 14/07 and ± 2 g for 15/07 and 16/07.

Date	UTC time	SO ₂ mass [g]	puffs	interval
07/07	13:25 - 14:46	20	38	irreg.
	15:15 - 16:29	20	43	90 s
08/07	09:07 - 12:19	20	100*	irreg.
10/07	07:16 - 09:14	20	95*	75 s
14/07	09:53 - 10:21	20	51*	30 s
	12:33 - 13:16	20	45	irreg.
15/07	07:55 - 08:02	15-35	8	60 s
	08:03 - 09:07	15-35	33	120 s
	09:52 - 11:40	15-35	63	90/120 s
	13:51 - 14:12	35	15	90 s
16/07	05:47 - 08:07	15-25	72	120 s
	08:29 - 09:39	22-27	35	120 s

* estimated

2019

In 2019, a completely new approach was taken for the instantaneous release: the puffs were released by filling and exploding balloons. This approach made it possible to control both shape and mass of the puffs but required a longer preparation time (>12 min) and hence shorter release frequency.

The tower construction was extended by a 1.8 m-long bar holding a steal cage at 57.5 m above ground. The steal cage could be pulled up to few metres below the bar using a system of winches which allowed to lift it to the same elevation of 55.3 m each time. On the last three days, the balloon was lifted 2 m higher. The steal cage had a flexible gas line (8 mm diameter, ca 85 m long) for SO₂ and air attached to a nozzle at its south pole and an adjustable steal scalpel attached to its north pole. Within this steal cage, balloons were filled until their increasing size caused the balloon to puncture. The balloon cage has an internal diameter of 95 cm and the scalpel punctured the balloons when they reached a diameter of 90 cm corresponding to a volume of 381 l. The balloons were manufactured of natural latex in different colours. The latex ruptured in 1-2 pieces which stay attached to the gas nozzle or fall directly down.

The same release procedure was followed to maintain nearly identical SO₂ puffs. The balloons were first pre-filled on ground level with ambient air for ca. 1 min until they reached a diameter of ca. 50 cm. Then they were lifted up to the release position where

they were filled with pure SO_2 from two canisters each holding 33 l of SO_2 . The canisters are in thermal equilibrium with the ambient air and the temperature is known from the metrological station at the lowest level at the tower. Previously, the cannisters were filled to 25 PSIG from the gas bottles. The balloons held between 250 g and 325 g of SO_2 . As soon as the balloons had the desired amount of SO_2 , they were filled with ambient air until they ruptured. The final air input additionally ensured that the SO_2 was well mixed within the balloon. The last balloon of a series of releases contained slight more SO_2 gas as the canister and line had to be emptied completely for security reasons.

Table (4.6) Puff release experiments in 2019

Date	UTC time	SO_2 mass [g]	puffs
11/07	09:57 - 10:57	250 ± 5	3
12/07	09:12 - 10:02	250 ± 5	4
	12:02 - 15:54	250 ± 5	10
18/07	19:20 - 21:30	250 ± 5	8
23/07	16:07 - 17:03	250 ± 5	4
24/07	06:19 - 09:35	250 ± 5	13
25/07	07:06 - 11:11	250 ± 5	14
	12:31 - 14:46	250 ± 5	10
26/07	08:42 - 12:37	250 ± 5	16
27/07	07:55 - 09:12	250 ± 5	7
	10:47	250 ± 5	1
	11:42 - 15:31	250 ± 5	19
28/07	07:18 - 08:46	325 ± 5	7
	11:01 - 15:32	325 ± 5	18

4.3 Meteorological conditions

4.3.1 First campaign: 6-20 July 2017

"The weather conditions in July 2017 were generally not favourable, with several cyclones passing over Fennoscandia during the campaign period. Daily average temperatures at a meteorological station located in the immediate vicinity (Rena øvingsfelt) ranged between 6.8 and 11.7° C, except for the last two days when they rose above 13° C. On 13 of the 19 campaign days, precipitation was recorded, and winds were often strong (up to 9 m s^{-1}). Conditions were suitable for instrument testing on several days, but clear-sky conditions were rare. The best conditions were encountered on 20 July when a ridge of high pressure built over Southern Fennoscandia. Even on that day, clouds were present but there were periods with relatively little cloud cover, enabling clear-sky camera observations for some viewing directions and yielding clouded scenes for the other cameras.", adapted from Dinger et al. [2018]

4.3.2 Second campaign: 7-16 July 2018

General conditions were more favourable than during the field campaign in 2017. Average temperatures were between 10.5 and 19.5° C as reported by the meteorological

station. However, completely clear-sky conditions occurred only before and after the active measurements of the campaign. Often, high clouds came in during the morning and intensified during the course of the day. The last day of measurements, 16 July, promised good conditions and the morning hours showed only few faint clouds for some cameras. Unfortunately, an electric power blackout affecting the whole region occurred at 9:40 UTC and power supply was provided again only on the next day when meteorological conditions were unfavourable again. Thus, except for the early morning hours, we could not do measurements during what otherwise would have been a near perfect (and certainly the best) measurement day.

4.3.3 Third campaign: 11-28 July 2019

The release tower was setup in the beginning of July 2019. However, the weather remained unstable, including snow fall and strong rain events, until 9 July 2019 when daily average temperature increased above 10°C and no precipitation was recorded for the following days. Nevertheless, sparse to complete cloud cover was often observed and the possibility of local, sudden rain showers required that all cameras had to be attended at all times. During the days with release experiments, the meteorological station recorded average temperatures between 8.9 and 20.4°C with warm, sunny and dry days towards the end of the campaign. Average wind velocities were weak to medium (generally below 5 m s^{-1}).

Chapter 5

The COMTESSA tracer dispersion data set

The measurement campaigns provided both Eulerian eddy covariance data and image data. In the following, the SO₂ slant column density (SCD) retrieval routine from the image data is described in detail (section 5.1). The SCDs were retrieved only for the best conditions when nearly clear sky was expected. For these periods, example snapshots are shown in section 5.2. This data set is the basis for all following analyses in chapters 6-7 in which the image data is analysed under Lagrangian aspects. It is planned that the data set will be made publicly available after the end of the project in 2020.

5.1 Retrieval of column-integrated SO₂ images

The raw intensity images have to go through several retrieval steps to get the final product, the SO₂ slant column densities. For a theoretical, general description see section 3.3. Here the practical application to the recorded data is described. The SO₂ image retrieval uses the open source PYthon PLume Imaging Software (pyplis) [Gliß et al., 2017].

Dark correction and pixel mask

In the following, all images were corrected for the dark signal. Dark images were recorded regularly at the same exposure time and temperature by shading all camera openings with a dark cloth. The dark signal was averaged over 1 min of images to reduce noise, when possible. All cameras showed a similar general pattern with a negligible dependency on the exposure time and a weak dependency on temperature. Hence the main contribution to the dark signal is the electronic offset. For the typically observed sensor temperatures of 30-40° C, the average dark signal makes 0.1 per mill of the maximum count rate but hot pixels reaching up to the maximum count rate were observed for some cameras and exposure times.

Sky masks were defined for every camera and viewing direction based on local intensity thresholds. The sky masks separated the images in two regions according to whether the intensity contained a reflected component or only backscattered sunlight. Sunlight can be reflected from the ground, topography in the background, and structures such as the release tower and antennas. This reflected region was ignored in the further analysis.

Background images

The optical density images of the SO₂ releases were calculated according to Eq. 3.7 from a SO₂-containing and SO₂-free background image. Owing to the artificial release of SO₂, it was possible to take SO₂-free images in the same viewing direction before or after the release. Hence in contrast to observations of continuous SO₂ sources, additional corrections of the intensity distribution were not necessary because the background was estimated from images recorded under the same azimuth and elevation angle. The background radiation at the moment of the release was calculated by linearly scaling the SO₂-free image. The scaling factor was found by comparing the mean intensity within a SO₂-free reference region in both images. However, due to the differences in release duration and cloud cover, the background estimation method was tailored to each set of experiment.

For puff releases with a large enough interval between the single releases, only one single puff was present in the camera's field of view (FOV) and, as soon as the puff left the FOV, the remaining images were averaged until the onset of the next puff release. This averaged image contained a reduced level of photon noise and was then used as background for the period of the next puff release. When clouds were present in the image, the background was averaged over only the last few seconds before the release to represent the cloud cover. This worked reasonably well for slow-moving clouds but fast-moving, inhomogeneous clouds caused strong artefacts nonetheless. The homogeneous changing of backscattered intensity (circa 0.5% and 5% in 10 minutes at noon and in the morning, respectively) was accounted for by scaling the background images. The scaling factor was found, by rationing the mean values of a 50×50 pixel scaling window in the background and puff image. Figure 5.1 shows the residual noise (mean and standard deviation) after the background correction in square, reference windows for a 10 min period of optical density images recorded by camera UV1. When the background image was updated (shaded areas), the mean in all references windows dropped close to zero and then drifts up to 0.003 until the next update of the background image. Distinct peaks in the optical density are due to passing of the puff through that window. The standard deviation was used to define a detection limit for SO₂, e.g. a 3- σ detection limit. However, the standard deviation depended on the saturation level of the images and the local area of the image due to optical vignetting and changes slightly over time and for different cameras. For the presented period, SO₂ was detected clearly when the optical density exceeds a value of 0.035 based on the highest value of the 3- σ limit. This detection limit is more than a factor 10 higher than the maximum drift due to the imperfect background estimate.

In the case of multiple puffs in the FOV and a strong, inhomogeneous cloud cover, SO₂-free images which represented the intensity distribution during the release were not available and scaling based on a permanent SO₂-free scaling window was not possible. Instead, the background images were created manually by overlaying at least two images for which the SO₂ containing pixels were masked out. In this way, the whole FOV could be covered with SO₂-free pixels. However, the correction of clouds persisted only for few ten seconds before artefacts in the same order as the SO₂ puffs appeared in the images. As this method was connected to significant manual effort, it was only applied to a short period of the 2017 data in Dinger et al. [2018] while analysis of the other campaigns was limited to more suitable data.

In contrast to typical applications at volcanoes or anthropogenic sources, pure SO₂ was released. It could not be observed in the off-band channel at 330 nm, that additional

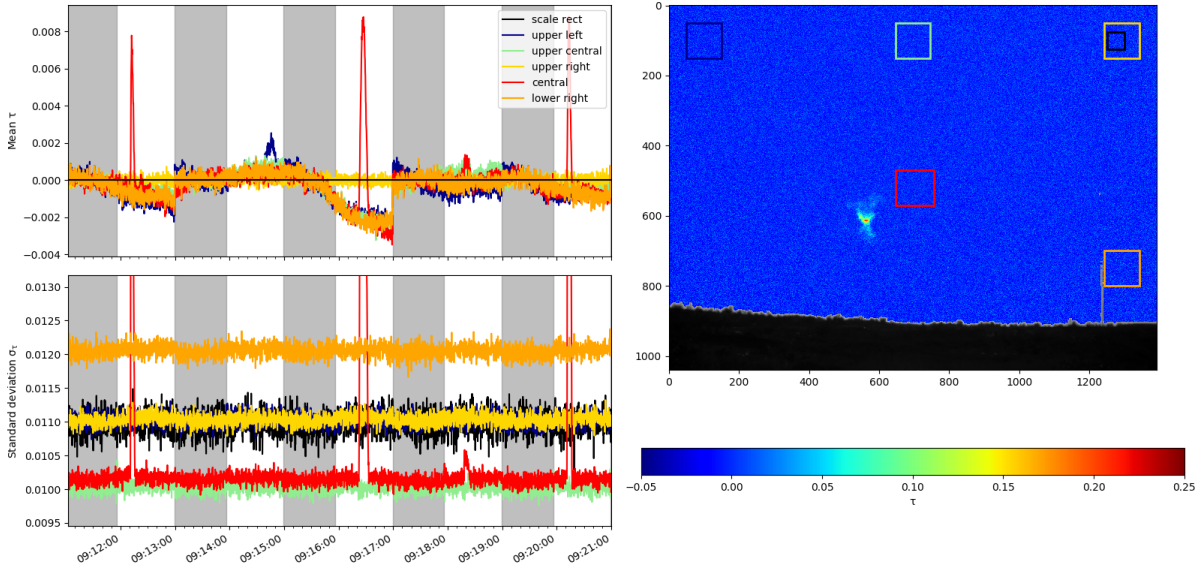


Fig. (5.1) Mean and standard deviation in arbitrary image areas (coloured squares) after background correction during a 10 min-period for camera UV1. The image areas are indicated in the example image recorded at 09:12:17 (right panel). The averaged intensity in the scaling window (black) was used to scale the entire background image. Differences in the standard deviations are due to optical vignetting which causes a higher signal-to-noise ratio in the central area than in the peripheral. The shaded area indicates the periods over which the background image was averaged.

aerosol was released or formed within the first few minutes after release. Therefore, the correction for broadband absorption and scattering at plume/puff particles was not necessary and the on-band channel at 310 nm was used directly as apparent absorbance. Further, the multiple scattering within the plume/puff was neglected due to the lack of aerosol. It was assumed that the effect of light dilution is relatively small due to the close distance to the release in 2017 and 2018. It can then be assumed, that the measured slant column densities can be approximated by the integrated concentrations along the solid angle of the pixel opening. In 2019, the distances for some cameras were significantly larger and light dilution might have an effect. However, a correction following Campion et al. [2015] was not attempted due to the lack of clear topography in the image background.

Optical camera calibration

For tomography it is essential, that the pointing direction of each pixel can be inferred. The optics of the camera caused the images to be both distorted and slightly shifted towards the optical centre. The optical centre and distortion parameters differed for each camera due to misalignments during assembly and manufacturing accuracy. According to the manufacturer, the 25mm and 12 mm lenses used for the COMTESSA cameras have a radial distortion of -4.05% and -6.8%, respectively. Further, the focal length of the lenses depend on the wavelength of the focused light. At the same time, the focus length defines the solid angle which each camera pixel covers (see chapter 6). The intrinsic camera matrix and the distortion coefficients of the individual cameras were measured following the method introduced by Zhang [2000]. This process is known as camera calibration in

computer vision applications. More details can be found in appendix A.3. All cameras showed similar radial distortion and negligible tangential distortion: The radial distortion was strongest at the image corners, where an undistorted pixel appeared circa 20 pixels closer to the optical axis. At a 500 m distance, this corresponded roughly to a translation of 4 m. The distortion was corrected in the following. In 2019, the measured focal lengths of the overall system ranged between 12.73 mm and 12.87 mm for the on-band-cameras and between 12.85 mm and 13.01 mm for the off-band cameras. From comparison of different sets of measurements, the relative error of the focal length was estimated to 1%.

SO₂ calibration

The images were calibrated to SO₂ column densities by multiplying with a calibration constant according to Eq. 3.9. The statistical analysis of turbulent dispersion does not require an absolute calibration to SO₂ and can be directly performed on optical density images. However, precise absolute calibration is important, for instance, if the total mass flux should be compared, for radiative transfer studies or for a full tomographic reconstruction.

Recent advances [Lübcke et al., 2013] in the SO₂ camera calibration made the calibration based on simultaneous spectroscopic measurements preferable over classical gas cell calibration. While spectra from the built-in spectrometer were available for the release periods, such calibration was often not possible as the time series of SO₂ column densities retrieved from the spectra contained none or only isolated SO₂ detections: The relatively small puffs and thin plumes (especially in 2018 and 2019) did not fill the spectrometer’s FOV or moved too fast. This led to either no signal, when the meandering puffs did not pass through the FOV or to an underestimated signal when the FOV was not homogeneously filled. Therefore, only for plume release experiments in 2017, the SO₂ camera images were calibrated according to Lübcke et al. [2013].

During the puff release experiments, the calibration constants were estimated based on gas cell measurements, performed during or after the release experiments. A total of 14 quartz glass cells filled with different amounts of SO₂ were available for calibration. The absolute SO₂ column densities were measured shortly before or after each campaign using the DOAS technique. In 2017 and 2018, the same four calibration cells were used for calibration of all cameras to ensure consistency of the calibration process. In 2019, the large distances between the cameras made it necessary that each camera was calibrated individually with two calibration cells each. Table 5.1 contains the absolute SO₂ column densities of the calibration cells measured with a spectrometer in June 2018 before the release experiment.

Table (5.1) Calibration gas cells as measured in 2018

Gas cell	SO ₂ column density
A34	$(2.28 \pm 0.06) \times 10^{17}$ molec cm ⁻²
A44	$(1.05 \pm 0.01) \times 10^{18}$ molec cm ⁻²
A54	$(4.34 \pm 0.08) \times 10^{17}$ molec cm ⁻²
A55	$(4.50 \pm 0.08) \times 10^{17}$ molec cm ⁻²

The calibration cells were manually positioned directly in front of the camera for a few seconds without changing the viewing direction. The optical density images were

calculated analogous as described above and averaged over the full calibration duration to increase the signal-to-noise ratio. The optical density values within the central area (200×200 pixels) were averaged to a single value. Only the central pixel were used in order to be less effected from vignetting and multiple reflection from the gas cell walls [e.g Lübecke et al., 2013]. The calibration constant was calculated by fitting a linear function to the relation between optical density and SO₂ column density. Often, the calibration was problematic due to the cloud cover. On 16 July 2018, the calibration was performed during completely clear-sky conditions after the last experiment (Fig. 5.2). The calibration constant was estimated to values between 3.8×10^{18} and 4.0×10^{18} molec cm⁻² for the different cameras and agree within the 1- σ fit error (up to 3×10^{17} molec cm⁻²). The slightly higher value for camera UV6 might result from its filter transmittance curve which is slightly shifted to higher wavelengths compared to the other cameras (see Fig. 3.7). Nevertheless, regarding the precision of the calibration method, differences in the calibration constant between the cameras due to different bandpass filters or due radiative transfer effects based on the different viewing are negligible. Cell calibrations performed on 15 July 2018 agree with the values obtained on 16 July 2018 within the error although the measurements were performed during sparse clouds cover and are generally less reliable.

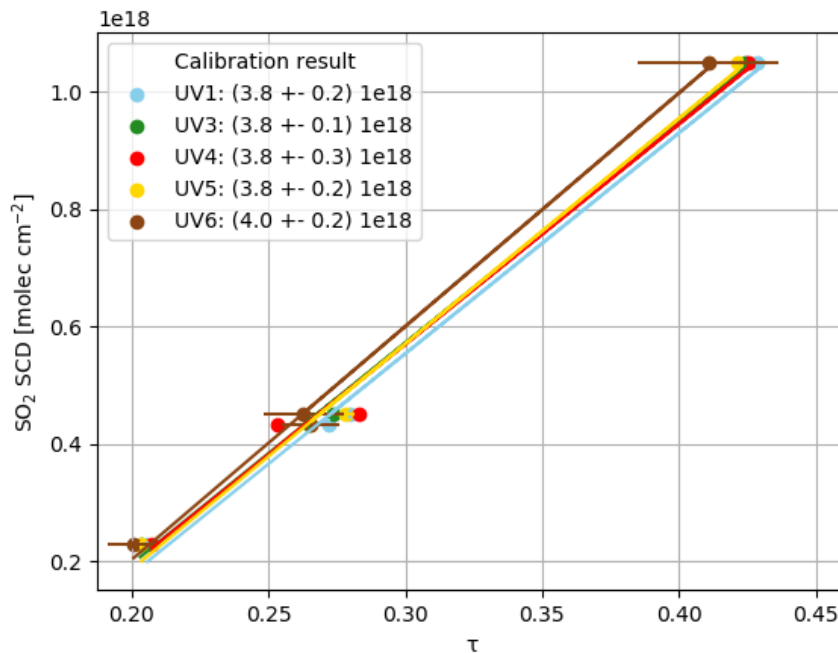


Fig. (5.2) SO₂ calibration using gas cells for all cameras on the 16 July 2018. The legend gives the fitted slopes. Images were recorded between 10:20 and 11:41 UTC.

The puffs in 2018 and 2019 showed optical densities exceeding 1 in the puff centres close after the release. From the simulated calibration curves in Kern et al. [2013], significant saturation effects can be expected for optical densities above 0.75. In 2018, such high values were observed for up to 20 s for single puffs in the centre. For these pixels the linear calibration fails. In 2019, the close cameras observed optical densities up to 1.5 in the beginning and values exceeding 0.75 for the entire observation duration of some puffs. Therefore, for the 2019 data, the linear calibration fails completely for some cameras and

here only optical density images are presented. The saturation might be corrected by radiative transfer simulations or by using the 330 nm-channel which observed significant optical densities at the high SCDs due to the weak absorption in that wavelength band. However, this has not yet been done.

Time synchronisation

Due to the fast movement of the plume and puffs, the tomographic reconstruction is highly sensitive to the time of the snapshot and requires that the times were synchronized a posteriori as accurately as possible. The cameras had an integrated GPS which synchronized the computer clock. Nonetheless, the cameras were out of sync up to 1 s when the GPS was synchronising and up to more than 10 s when the GPS synchronisation failed. As cause of the missing synchronisation, two processes were identified: 1) Lack or failure of GPS synchronisation (all data in 2017, few episodes of single cameras in 2018) and 2) an internal process/clock in the pco.ultraviolet cameras. For a posteriori synchronisation, the puff release times (first image with visible SO₂) were detected manually and aligned. The time difference between the camera times was a proxy for the time de-synchronization. It is important to note, that the precision of these timestamps were limited by the exposure time of the cameras. The puff could have been released at any moment between the start of the exposure and the end or even during the exposure of the previous image e.g. when the release was towards the end of the exposure and the integrated SO₂ columns did not exceed the detection limit. In most cases, the temporal offset between the cameras was in the order of the exposure time.

5.2 SO₂ image data set

The three campaigns were performed in three successive years at the same experimental site. The release and measurement setup was improved in the course of the years (see chapter 4). The main differences are summarised in table 5.2. The 2017 campaign was primarily an instrument and methodology test with lowest release heights and close distance imaging with mainly plume releases. In the 2018 and 2019 campaigns, the focus shifted to puff releases from a higher source. The cameras were moved further away and the lenses were exchanged from the 25 mm to 12 mm focal length. Combined, this led to an increase in apparent pixel size by more than a factor of 4 (for double distance), and an accordingly larger FOV and observation duration but corresponding lower pixel resolution (compare table 4.2). The weather conditions were unfavourable during all three campaigns with 2018 being probably the best with an exceptional sunny summer in Southern and Central Norway. Cloud cover was prevailing in most days during all three years. Release experiments were performed nonetheless when there was a chance that clear sky or at least sparse cloud cover could be expected. However, this kind of raw data requires manual tuning of the background and will remain of lower overall quality or a quantitative SO₂ retrieval is not possible. Therefore, for these periods SO₂ column densities were not retrieved from the raw data.

In the following, sample SO₂ image data is presented for the different experiments and the main features are discussed. For better visualisation, the noise in all images was reduced by applying a Gaussian filter (mean: 0, STD: 3). All times in this thesis refer to coordinated universal time (UTC). The local time zone is UTC+2h, i.e. noon was at

10:00 UTC. In 2018, camera UV2 had a technical failure during the entire duration of the campaign and hence only 5 cameras recorded images.

Table (5.2) Overview of the three field campaigns (average values)

	first campaign July 2017	second campaign July 2018	third campaign July 2019
measurement days	6	6	11
release height	9 m	61 m	55-61 m
released plumes	422 min	209 min	32 min
max release rate	3 g/s	3.5 g/s	2.5 g/s
released puffs	210	600	134
release amount, puffs	1 g	20 g	250 g or 325 g
total released SO ₂	50 kg	34 kg	71 kg
max. camera distance	190 m	500 m	1200 m
camera FOV	14.2° × 10.7°	28.7° × 21.7°	28.7° × 21.7°

5.2.1 Plume releases

The released SO₂ emission rate could only be slightly increased in the course of the three years (see chapter 4). Therefore, most plume releases were performed in 2017 when the cameras were placed closest. In 2017, the best plume release was observed on 20 July 2017 during the morning (7:19 - 9:53 UTC) during partially clear sky. A snapshot of this plume release from all cameras and a sequence of snapshots from the perpendicular looking camera UV3 can be seen in Fig. 5.3 and 5.4. In 2018 and 2019, plume releases were performed mainly to adjust the cameras' FOV to the projected wind direction. When quantitative plume releases were performed, it was typically in the early morning or in the afternoon when the cloud cover was more prominent. In the early morning and late afternoon, overall light intensity was low, changed rapidly and had strong gradients due to the low solar position. The background correction could account for that only up to limited accuracy. Therefore, the SO₂ retrieval during early morning releases in 2018 was of lower quality than the one during the 2017 campaign. The highest release rates (up to 3.5 g/s) were reached on 14 and 15 July 2018 before and after the puff releases. However, high clouds were present in all images and camera placement and exposure times were not ideal. On 16 July 2018, the sky was clear but the continuous release was performed for adjustment reasons only (Fig. 5.5). Quantitative plume experiments were planned for later during the day but were not possible due to the power outage stalling all further experiments. Comparable plume data during partially cloud-free conditions, are available from 26 July 2019 but with some of the cameras placed at larger distances.

All observed plumes filled the entire cameras' FOVs in the course of a few minutes indicating strong meandering. For example, it can be observed how the plume on 16 July 2018 appears to be folding over itself while following the motion of large eddies. Although the emission rate can be assumed constant over short time scales, the plumes separated into patches of high and low SO₂ concentration. Particularly, the detection of the patches of low concentration and hence low column densities became challenging with downwind distance to the source, as the the dispersion of the plume and mixing with surrounding air caused the SO₂ SCDs at the border of the plume to drop below the detection limit. Thus

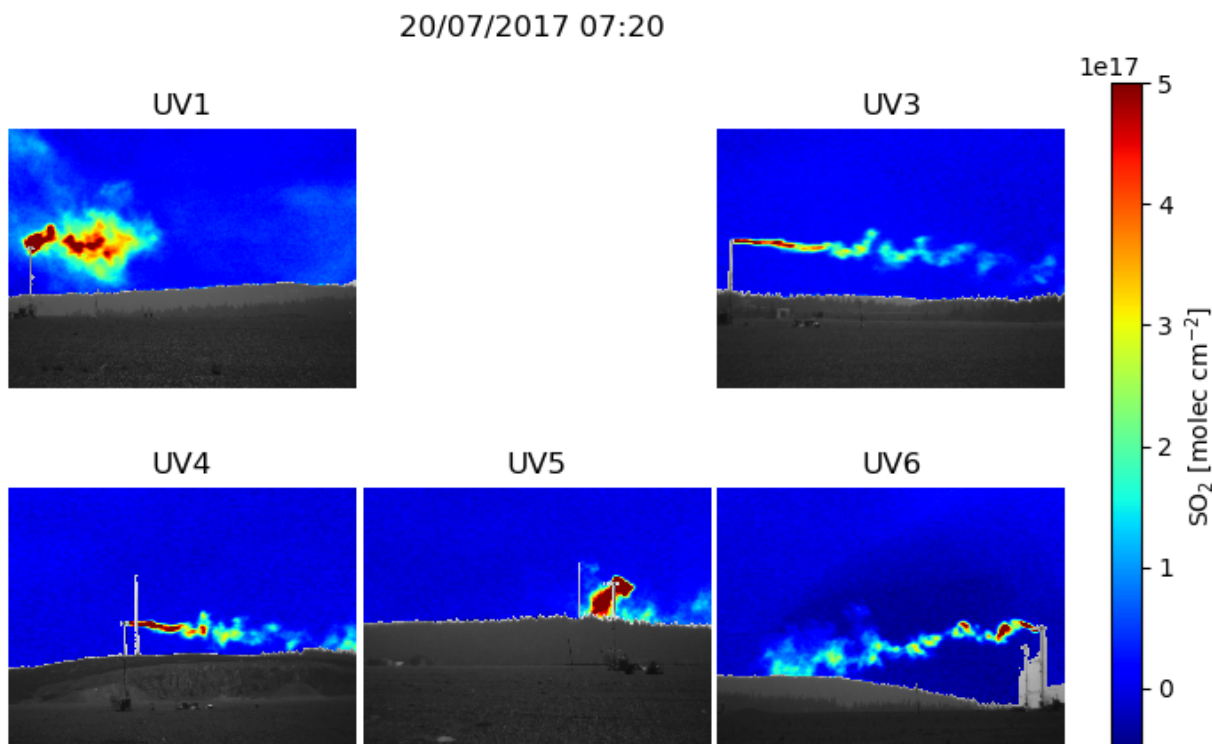


Fig. (5.3) Continuous release on 20 July 2017 7:20: Snapshot of SO_2 camera images. Camera UV2 was not operating in the early morning.

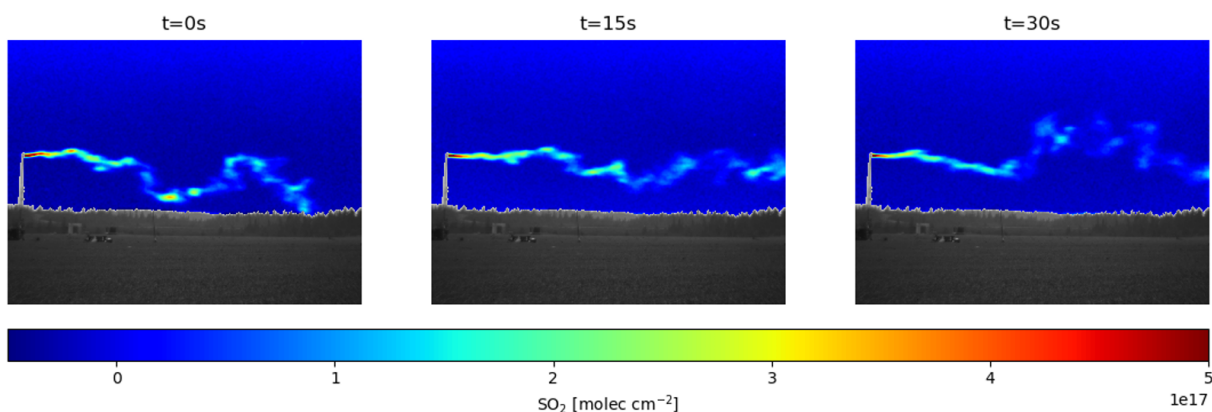


Fig. (5.4) Continuous release on 20 July 2017 8:40: Sequence of SO_2 camera images from camera UV3. The camera observed the plume perpendicular to the mean wind direction. The vertical plume meandering is clearly visible.

a larger fraction of the plume was not detected. This was particular problematic in 2018 and 2019, when the FOV was larger than in 2017: Large parts of the plume were below the detection limit before leaving the FOV. However, the total observed plume length was nonetheless larger than in 2017.

5.2.2 Puff releases

The release procedure changed from gas bottle to canister to balloon releases and the total release amount increased from circa 1 g per puff to 325 g in the course of the three

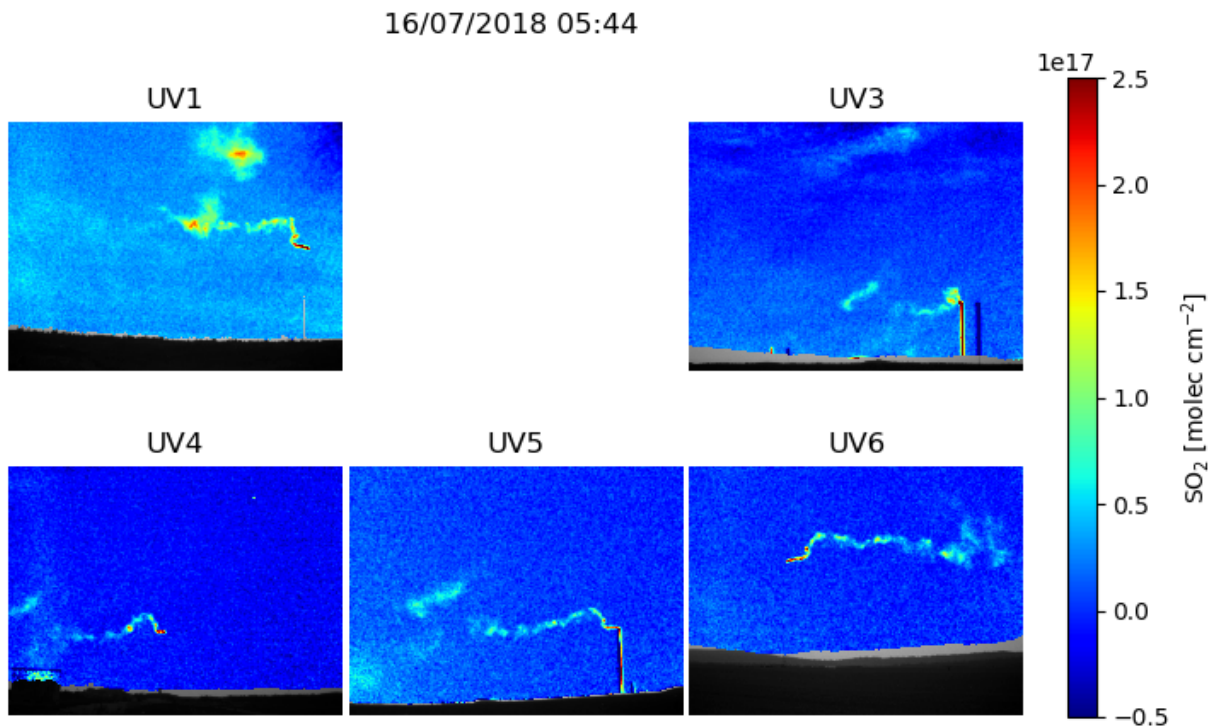


Fig. (5.5) Continuous release on 16 July 2018 5:44: Snapshot of SO₂ camera images. Due to the early morning measurement, the background contains a higher noise level and artefacts. The release was performed for camera adjustment and the cameras were moved during the release. Therefore, distinct features of the background, e.g. the tower, cannot be corrected.

campaigns. Naturally, the observed puffs behaved differently during the three campaigns.

In 2017, only one set of puff releases was performed during partly cloudy conditions. At the start of the puff release experiments (10:00), the field of view of camera UV1 was completely cloud-free, cameras UV2-UV4 observed sparse clouds and cameras UV5 and UV6 observed a full cloud cover in the background. SO₂ SCD images were retrieved for 10:29-10:31 using manually-combined background images (see section 5.1) (Fig. 5.6). Due to the rapid movement of the clouds, the additional optical density of the cloud cover could only be corrected for a few seconds with a single background image, leading to strong artefacts in the SO₂ images of cameras UV5 and UV6. Despite the cloud cover during the puff releases, this short data set was used to demonstrate the novel methodology to study puff dispersion presented in this thesis and Dinger et al. [2018]. The puffs were released with high frequency (6 puffs/min) and could be observed for more than ten seconds. This led to the presence of more than one puff in the images of some cameras (Fig. 5.7).

In 2018 and 2019, puff releases were the main experimental focus and releases were performed whenever the cloud cover was sparse with chance of improvement. Therefore, SO₂ images could be retrieved for long periods on several days during both years. Due to the large distances, the puffs fill only a small area ($<100 \text{ pixels} \times 100 \text{ pixels}$) of the images, also after few ten seconds. The puffs could be observed for 1-2 minutes from most cameras and mostly, single puffs were present in the images. Figures 5.8 and 5.9 show snapshots of the cameras during the puff release. In 2019, trees in the foreground obscured the view of the puffs.

In general during all three campaigns, the overall movement of the puffs was dominated

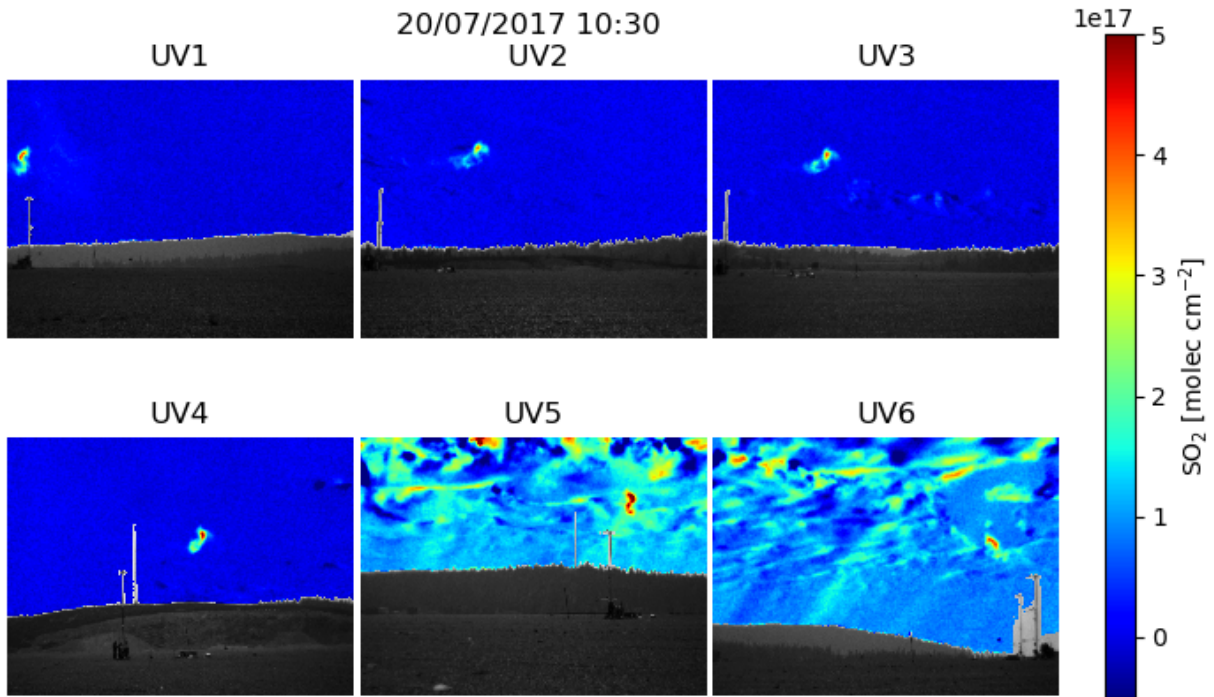


Fig. (5.6) Puff releases on 20 July 2017 10:30: Snapshot of SO_2 camera images. Artefacts due to cloud cover appeared with increasing time to the background image. For cameras UV5 and UV6, the signal from artefacts was as strong as the signal from the SO_2 gas after few seconds.

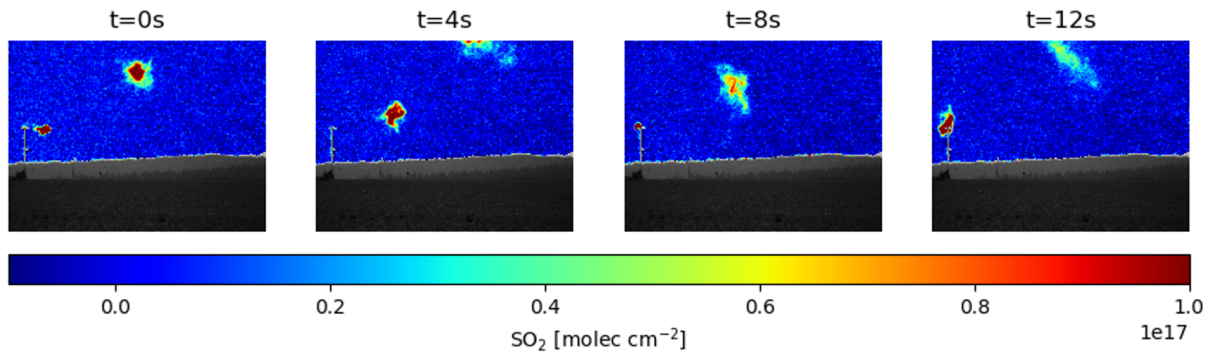


Fig. (5.7) Puff releases on 20 July 2017 10:30: Sequence of SO_2 camera images from camera UV1. The puffs moved approximately towards the camera. Notice that at all times two puffs are visible in the FOV of the camera.

by the meandering motion of their centre of mass which filled the entire FOV for sideways facing cameras. The puffs remained comparably compact but exhibited complex internal structures and rotations around multiple axes (see Fig.5.10 and 5.11). The puffs increased or decreased their sizes in the images depending on their moving directions relative to the cameras. Similar to the plume releases, the edges of the puffs dropped below the detection limit.

For a statistically analysis of the puff releases, the puffs are assumed to be released instantaneously from a symmetrical source. However, in reality in 2017 and 2018, the SO_2 had to be transported through the pipe to the top of the release tower. In 2018,

it took up to 2 second until all SO₂ gas left the pipe due to dispersion inside the pipe and friction on the pipe surface. As consequence of the extended release, the puffs were elongated rather than spherical as expected from a point source. The deviation from a round shape depended on the strength of the advection by the wind. In 2017, the puffs were released directly from the gas bottles leading to a varying shape and mass. In 2018, the puffs were release from a canister with constant volume. Most puffs in 2018 were circa 6 m long with 2m diameter. The elongated shape could be observed clearly from cameras with a perpendicular pointing direction (see e.g. camera UV1 and UV5 in Fig. 5.10). After a few seconds, the puffs dispersed and the initial elongated shape could no longer be recognised. In 2019, the puffs were released by sudden puncture of a spherical balloon. The puffs showed the desired spherical shape directly after release (see Fig. 5.11 first row). Additionally, due the larger distances and 10 times higher release amount, the puffs were observed up to few minutes. However, camera saturation or heavy gas effects might play a role close to the release while the puffs are still compact.

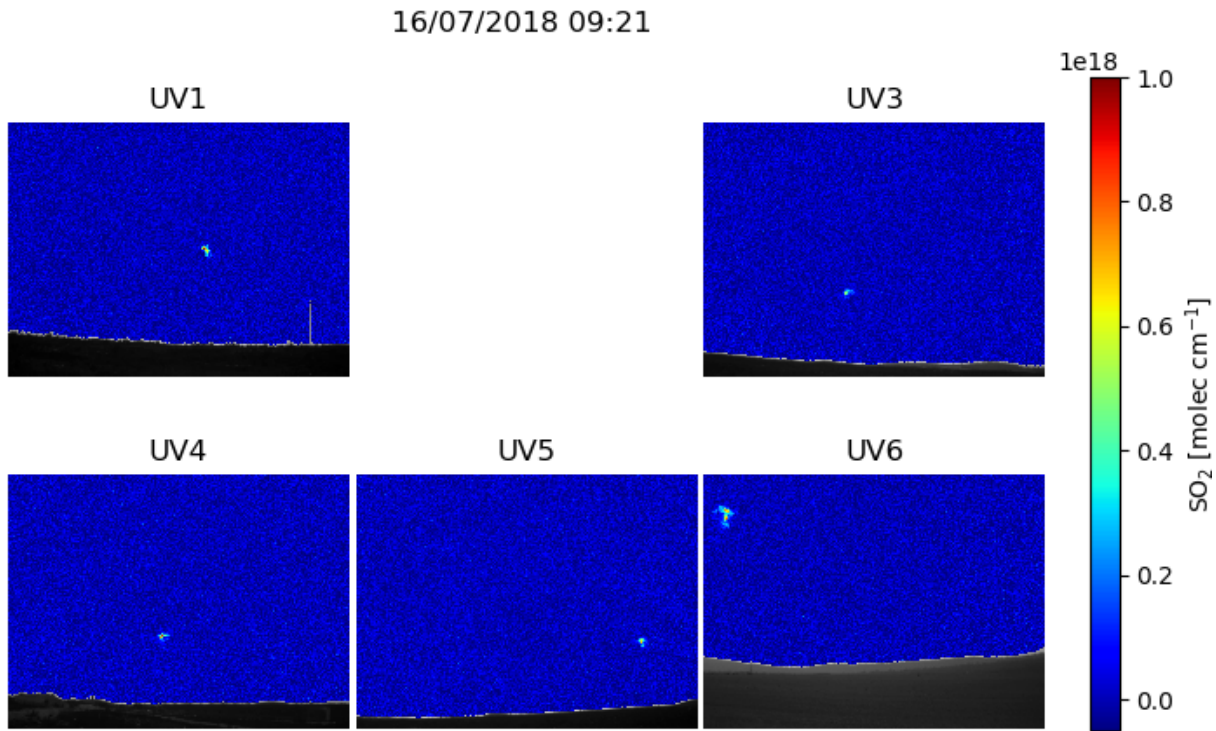


Fig. (5.8) Puff release on 16 July 2018 09:21: Snapshot of SO₂ camera images. The puff fills only a small area of the total images.

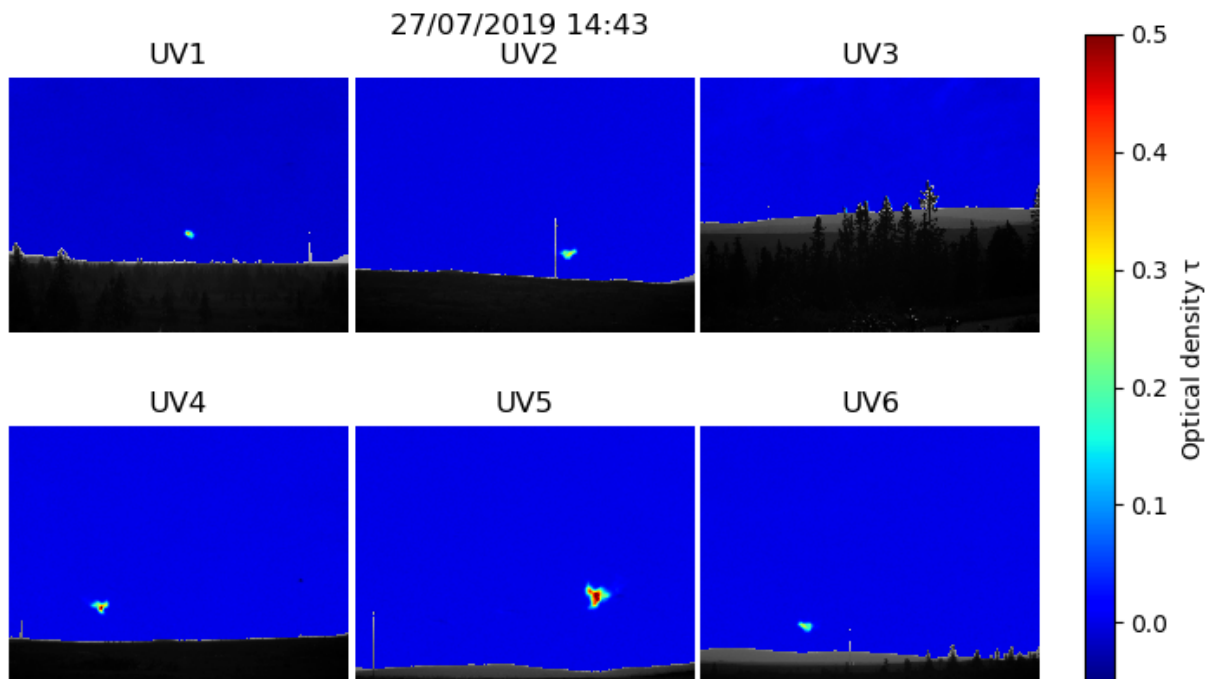


Fig. (5.9) Puff releases on 27 July 2019 14:43: Snapshot of SO₂ camera images 45s after release. The cameras were positioned at different distances to the release tower, leading to different puff sizes in the images. From the position of camera UV3, the puff was behind a tree.

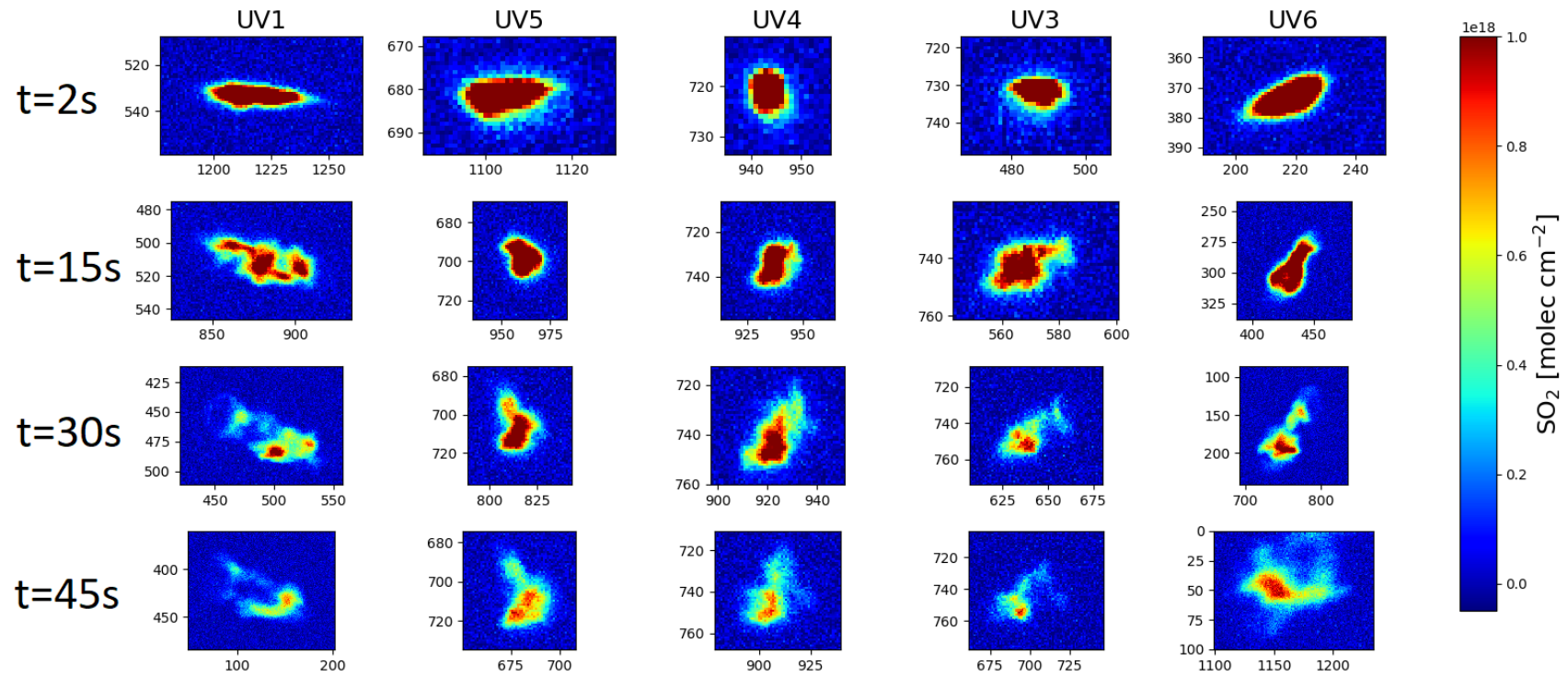


Fig. (5.10) Puff release 25 on 16 July 2018 6:35: Sequence of SO₂ camera images of a single puff. Each rows shows a zoomed-in snapshot of the puff projected to the five cameras at a different time after release. The cameras were placed on a half circle around the release and the column order represents their order along the circle. Note that due to different distances between cameras and the puff, the pixel sizes of the images are not comparable. The elongation of the puff at the release is clearly visible. Within few seconds after release, concentration distribution exhibits complex shapes.

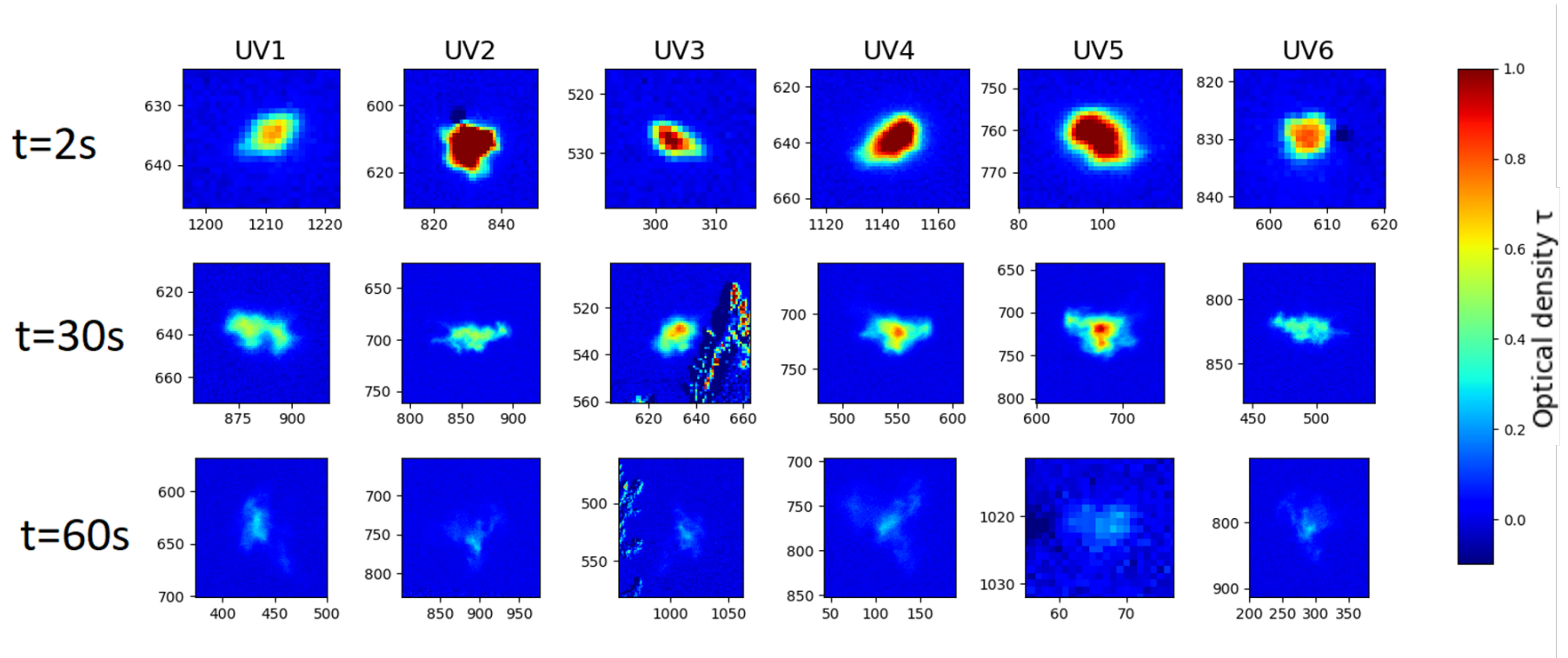


Fig. (5.11) Puff release 23 on 27 July 2019 14:43: Sequence of SO₂ camera images of a single puff. Each rows shows a zoomed-in snapshot of the puff projected to the six cameras at a different time after release. The puff had a spherical shape. For camera UV3, the puff passes behind trees which are visible as artefacts in the zoomed-in images.

5.3 Discussion

The COMTESSA tracer experiments were a novel attempt to quantify the dispersion of a passive tracers, here sulfur dioxide, with SO₂ cameras. The dispersion of continuous and instantaneous releases on different days over the course of three years were quantitatively imaged from up to six viewing directions simultaneously. The state of the surface layer was in parallel characterised by eddy covariance measurements along up to three towers. Different viewing geometries and experiments have been tested. Plumes and ensembles of puffs which could be observed for up to few minutes and several hundreds meters were recorded. The meandering motion filled generally the entire field of view of the cameras while the plume diameter and puffs generally stay compact.

The COMTESSA data set is a comprehensive data set of three campaigns at the same spot. Therefore, the experimental setup remained comparable while a variety of conditions was observed. The data set contains both classical, Eulerian measurements of turbulence along the towers and SO₂ camera images which can be used for both Eulerian and Lagrangian analyses. The image data has a high spatial (few centimetres) and temporal resolution (few Hertz) and provides integrated concentrations along the line of sight. Compared to previous experiments relying on black-and-white photographs of smoke clouds [e.g. Gifford, 1980], integrated concentrations can be retrieved from SO₂ camera images. This allows for tomography. Such kind of data set with comparable temporal and spatial resolution has not been available from other studies.

The biggest drawback of all three measurement campaigns was the unfavourable weather of Norway. Performing the experiments in another place with stable fair weather periods and general higher solar radiance, simplifies the logistics significantly and increases the chance for successful measurements. However, the requirements for the experimental site and necessary local support were high: Sulfur dioxide is a toxic gas and deliberate releases have to be made in accordance with national environmental agencies which prefer collaboration with institutions from the same country. Further, a fenced-in, large and flat area was required to study an undisturbed turbulent flow and to limit visible topography in the image background. Besides deserts, military areas are well-suited but again need special agreements. Despite considerable efforts, we were not able to get access to a site at a more favourable location. The unfavourable weather conditions caused many cloud artefacts in the images. This limited the amount of usable data significantly and prohibited a straightforward SO₂ retrieval. Also, the non-ideal background analysis increased the noise in the images and therefore the detection limit. As consequence, the duration of the plume releases and the number of puff releases under similar conditions was relatively low which might lead to biases under a statistical analysis of the turbulent dispersion. The background correction could be improved by using images before and after the release to interpolate the linear scaling parameter rather than using a single image. This could account better for gradients in the image background, however, structured clouds could still not be corrected for. Alternatively, an iterative approach could be used to correct for clouds: First, the preliminary SO₂ column densities are retrieved to constrain the position of the puffs. Then, the last image which had no SO₂ within the estimated ROI of the puff is identified and the SO₂ SCDs are calculated based on this image without additional scaling and only within the ROI. This corresponds to an automated creation of the overlay-images used in 2017 but requires that the position of the puffs can be detected automatically after the preliminary background correction.

The experiments required a considerable effort in designing, organising and completing

by a team of more than ten scientists at NILU. The high cost linked to the equipment prohibits that the experiments can be easily repeated. However, several lessons have been learned for future studies. The puff release technique was improved to ensure a sufficient high release amounts to be detected by the SO₂ cameras, a consistent mass and a symmetric, spherical shape of the puff to avoid non-isotropic dispersion. Balloon releases were found to be most suitable for this purpose. The SO₂ release rate for continuous releases was limited by the available valves and gas bottle temperature. The maximum achieved release rates of 3.5 g/s were too low to be able to observe the plume from a large enough distance to study the turbulent dispersion several minutes downwind. When placing the cameras, we were limited by the topography. At the same time, the goal of the experiment determines which distances and lenses were chosen. A large field of view was desired for long observation times. However, the puffs extended only over comparably few pixel limiting the resolution for a tomographic reconstruction. Hence, if the internal structure of the puff dispersion should be studied, smaller field of views are required. An option to combine both long observation times and high spatial resolution would be, assuming relatively stable wind direction, to position a set of cameras to image the air volume close to the release and a second set to image the air volume downstream of the release. However, this setup complicates tomography: More cameras in total are required and the relative pose of the sets of cameras needs to be reconstructed accurately, e.g. using distinct topography or custom-made targets. A possibility would be to use a UV LED-target on a drone equipped with accurate real time kinematics or differential GPS recording continuously the drone's 3D position with centimetres accuracy. Provided time synchronisation, flying the drone slowly through the field of view of the cameras will create a large number of available feature points in the image. This set of 3D positions with corresponding image coordinates will enable a complete camera calibration including the camera's pose, position and distortion parameters.

Chapter 6

Turbulent dispersion from SO₂ camera images

The released SO₂ is subject to turbulent dispersion. The dispersion of a SO₂ plume relative to its propagation direction is visible in a single image. Assumed that the mean propagation direction does not change, the statistical nature of the dispersion can be analysed when many such images are available. For puff releases, each image represents a snapshot of the puff shape and the evolution of the shape of this single puff can be accessed by a time series of SO₂ camera images. Again, an ensemble of many time series of puff releases is required for studying the turbulent dispersion. The enclosed SO₂ distribution of a puff allows for constraining its position in the image plane easier than the position of plumes. Therefore, in the rest of thesis, ensemble of puff releases were chosen to study turbulent dispersion.

The motion of each puff can be separated into a centre of mass (CM) motion and a relative motion around its centre of mass. Eventually, we are interested in reconstructing the three-dimensional (3D) properties of the motion i.e. the extension of the puffs to study its relative dispersion as well as the 3D trajectories to study meandering and velocity autocorrelations. The images represent the SO₂ distribution projected to the two-dimensional (2D) camera sensor (see Fig. 6.1). Without additional information, the projected shape and centre of mass can be extracted only in pixel coordinates from the images of a single camera. Each pixel spans a solid angle whose cross section at the position of the puff depends on the distance d . The apparent width of one pixel $s(d)$ for a camera with focal length f and physical pixel width on the sensor s_p will be

$$s(d) = s_p \frac{d - f}{f}. \quad (6.1)$$

For SO₂ distributions whose extension in direction of the light path are negligible small compared to the overall distance to the camera, the image coordinates can be scaled with $s(d)$ to represent axes in metres. For more extended but symmetrical distribution, the effect of increasing distance from the front to the end of the puff will cancel out in first approximation if the distance to the centre of mass is considered. This distance between the puff and the camera sensor can be estimated by reconstructing the 3D CM trajectory from a set of simultaneous images of the same puff from different viewing directions.

Here, a simplified tomographic algorithm is presented to reconstruct the 3D trajectories of the centre of mass of the puffs and the relative dispersion projected to the image planes. Then, in chapter 7, large ensembles of puff releases are used to quantify the

relative dispersion and CM velocity correlations statistically. The method is presented for SO₂ column density images but it can be applied to images of any kind of integrated quantity. This chapter follows and extends Dinger et al. [2018]. Identical phrasing occurs.

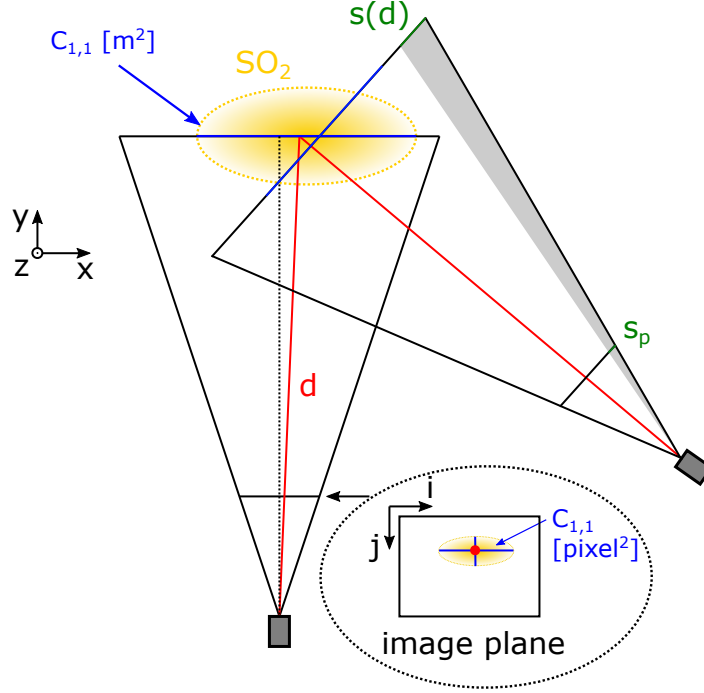


Fig. (6.1) Sketch of the field of view of two cameras from above. The three-dimensional SO₂ puff (yellow) in the world coordinate system (x,y,z) is projected to the two-dimensional image plane (i,j). The centre of mass in the image plane corresponds to a solid angle in the world coordinate system (red). The apparent size of a pixel scales with the distance to the object plane (grey area). Adapted from Dinger et al. [2018]

6.1 Detection of puffs

As a first step, the puff is detected inside the image to separate it from clouds or additional puffs which are present in the image. The detection algorithm tracks rectangular extensions ("region-of-interest", ROI) which contains the arbitrary shaped projection of the puff in the image plane and surrounding SO₂-free pixels. The ROI is generously chosen to make sure that the entire puff lies within. Let the image plane be spanned by two discrete coordinate axes $i = [1, \dots, N_i]$ and $j = [1, \dots, N_j]$ describing the image columns and rows. Then, based on the ROI, the total summed signal S_{tot} and the pixel coordinate of the centre of mass (i_{cm}, j_{cm}) of the puff can be calculated from the image

$$S_{tot} = \sum_{i,j \text{ in ROI}} S(i, j) \quad (6.2)$$

$$\begin{pmatrix} i_{cm} \\ j_{cm} \end{pmatrix} = \frac{1}{S_{tot}} \sum_{i,j \text{ in ROI}} S(i, j) \begin{pmatrix} i \\ j \end{pmatrix} \quad (6.3)$$

where $S(i, j)$ is the SO_2 column density at pixel (i, j) . When the distance is known, $S(i, j)$ is scaled with the column cross section at the position of the puff represented by $s^2(d)$. The total mass M is given by

$$M = s^2(d) \cdot S_{tot} \quad (6.4)$$

The spread of mass around its centre, as expressed by the variance, is described by the weighted covariance matrix \mathbf{C} . The diagonal elements of \mathbf{C} are the spreads of the SO_2 puff in the image plane along the image columns and rows respectively. These diagonal elements are defined as

$$C_{1,1} = \frac{1}{S_{tot}} \sum_{i,j \text{ in ROI}} S(i, j) \cdot (i - i_{cm})^2 = \frac{1}{S_{tot}} \sum_{i,j \text{ in ROI}} i^2 \cdot S(i, j) - i_{cm}^2 \quad (6.5)$$

$$C_{2,2} = \frac{1}{S_{tot}} \sum_{i,j \text{ in ROI}} S(i, j) \cdot (j - j_{cm})^2 = \frac{1}{S_{tot}} \sum_{i,j \text{ in ROI}} j^2 \cdot S(i, j) - j_{cm}^2 \quad (6.6)$$

$$(6.7)$$

For non-spherical puffs as observed in 2018, it can be meaningful to calculate the spread along the axes of strongest variance rather than along the image axes. This is called principal component analysis (PCA) and calculates the eigendecomposition of \mathbf{C} by finding the matrix \mathbf{V} that diagonalizes \mathbf{C}

$$\mathbf{V}^{-1}\mathbf{C}\mathbf{V} = \mathbf{D} \quad (6.8)$$

with the diagonal matrix \mathbf{D} . Then, the eigenvectors of \mathbf{D} define the main and minor axes and the eigenvalues of \mathbf{D} are the variances along these two axes.

For a known distance, the spread of the puff in metres becomes

$$C_{a,b}[\text{metre}^2] = s^2(d) \cdot C_{a,b}[\text{pixel}^2] \quad \text{for } a, b \text{ in } \{1,2\} \quad (6.9)$$

This spread corresponds to the relative dispersion of a single puff projected to the image plane. For cameras observing the puff perpendicular to its propagation direction, it can be interpreted as the relative dispersion in along wind direction. Analogously, other cameras observe the cross wind component or a combination of both. For small elevation angles, the spread along image rows can be interpreted as vertical dispersion. The elevation angles of the cameras were 5-12° during the puff releases analysed in the rest of the thesis, leading to an extension of the light path through the puffs by up to a factor of $1/\cos(12^\circ)=1.02$ for homogeneous puffs. Due to the complex shape of the puffs, no correction factor is applied and the spread along image rows is directly used as estimate of the vertical dispersion. However, the vertical dispersion might be overestimated and an relative uncertainty of 2% should be assumed.

6.1.1 Detection algorithm

The following section is adapted from Dinger et al. [2018].

The ROIs of the puffs are detected automatically and iteratively in each time series of a puff release. Figure 6.3 depicts the tracking algorithm schematically. The algorithm is based on three copies of the original image (see Fig. 6.2): (1) the original high-resolution image, (2) an image which was blurred with a 2D Gaussian function (mean $\mu=1$, standard deviation $\sigma=5$) and (3) a low-resolution image which was sub-sampled to $(87 \times 65 \text{ pixel})$

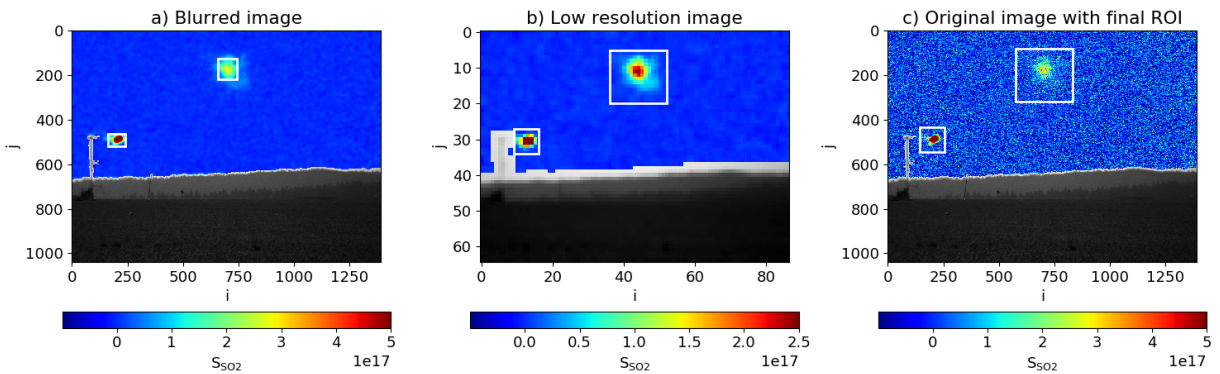


Fig. (6.2) Puff detection based on noise-reduced images, here for camera UV1 at 10:30:12 on 20 July 2017. The ROI is detected in a blurred image based on the position of the CM in the previous image (a). A low resolution image is used to detect connected areas above a threshold (b). The combination of both detections gives the resulting ROI, which is used to calculate the CM, total signal and spread in the original image (c). Reproduced from Dinger et al. [2018]

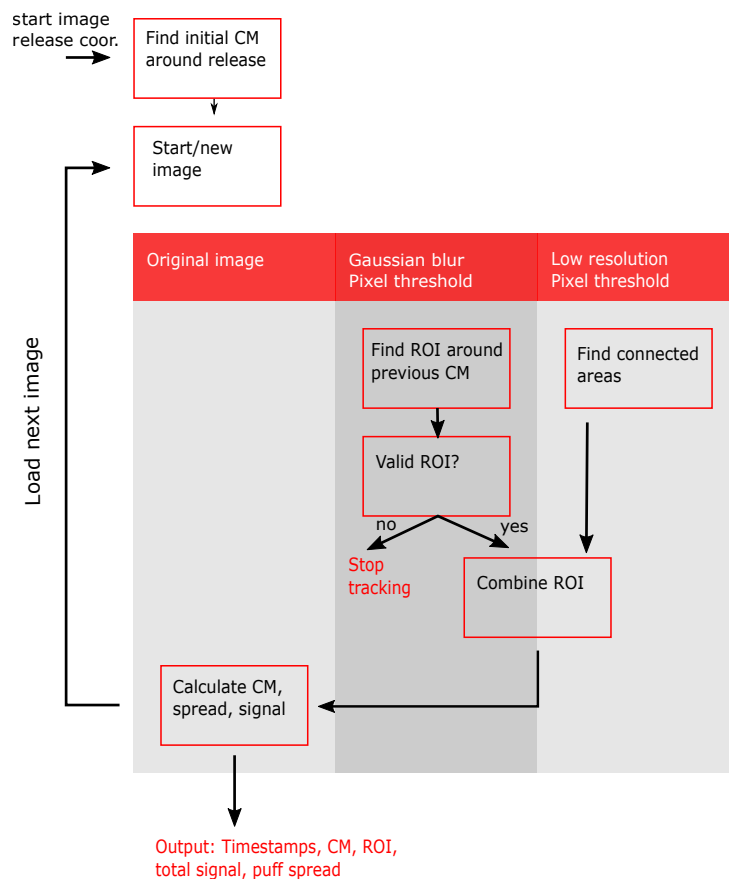


Fig. (6.3) Flow diagram of the detection algorithm. The puffs are detected iteratively based on the previous detection and two noise-reduced versions of the original image. The conditions for a valid ROI can be found in the text. Reproduced from Dinger et al. [2018]

using image pyramids. The images are increasingly noise-reduced and have consequently lower detection limits for SO₂.

The puffs are tracked iteratively from the release point. Therefore the image coordinates of the release point and the release time of the individual puffs have to be provided manually. The release time can be detected using signal thresholds around the release point if it is not available. The tracking will start from this first image. After every successful detection of the ROI, the next image will be loaded. First the ROI is detected within the blurred image around the last-known position of the puff. That is the coordinate of the release for the first image, and the one of the CM in the previous image for all other images. A 50×50 ROI is set around this coordinate. Then the ROI is increased incrementally by single image rows and columns. New pixel rows or columns are added to the ROI if they contain at least 5% pixel above the threshold value 1.5e16 molec cm⁻². The threshold is chosen as the double of the standard deviation to suppress noise and cloud artefacts effectively. The ROI contains the central part of the puffs but not necessarily separated fractions and weak tails. Weak tails and separated fractions can be detected within the low-resolution image which suppresses noise 4-times more compared to the blurred image. The image is separated into connected regions containing a significant signal. A pixel is considered to contain a signal if the average of the pixels in a 5x5 neighbourhood is above a threshold. This method detects the SO₂ puffs and clouds alike, thus a separate selection is necessary to identify the puffs. The detected ROIs are rescaled to the original resolution and compared to the previously detected ROI from the blurred image. If the previously found ROI immerses completely in a new ROI, it will be replaced by the larger ROI. In this way, the full area of the puffs including tails close to the detection limit and separated SO₂ patches are included. When the final ROI of a puff is determined, the total signal, CM and spread of the puff are calculated within this ROI based on the original image. For the next image, the CM of the previous image is used as a starting point for the ROI which is determined equivalently. The procedure is repeated until an invalid ROI is detected. This is the case when the puff touches the image borders or moving in front of non-sky areas such as the ground or vegetation and topography on the horizon. In these cases, the ROI would no longer contain the complete puff. Further, the tracking stops when it is likely that cloud artefacts are tracked instead of the puff. This can be indicated by jumps in the CM or a sudden increase or decrease of the ROI.

6.1.2 Total signal

Due to mass conservation, the masses retrieved from all cameras should be approximately equal over the whole observation period. The total summed signal, on the other hand, gives insight to the quality of detection. Figure 6.4 shows the total signal from all cameras for an example puff (number 25) on 16 July 2018. Images of this puff can be seen in Fig. 5.10. The total signal was calculated including all pixels within the ROI and additionally including only pixels whose signal exceeded the 3 σ detection limit where σ is the average standard deviation of the full resolution image.

Several aspects of the signal are discussed exemplary for puff 25 but are valid for all puffs

1. Initial signal: After a short increase, the total signal for each camera reaches an initial signal. This initial signal was more than a factor 2 different for the cameras depending on their distances to the release. The standard deviation of the cameras

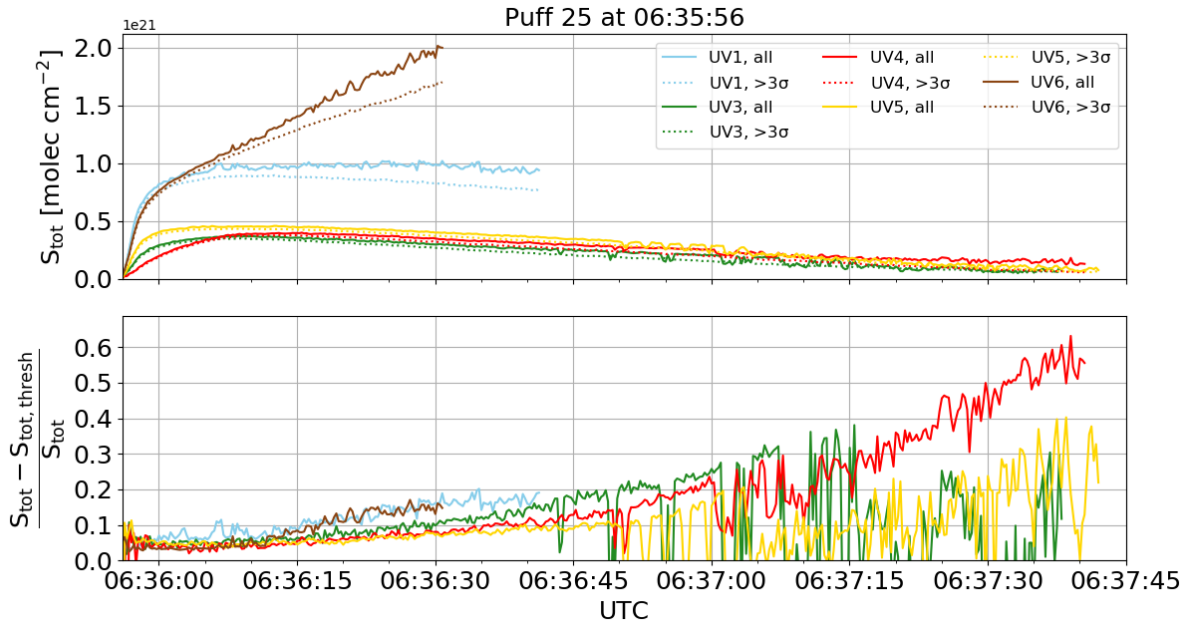


Fig. (6.4) Total signal (Eq. 6.2) in the region of interest for puff 25 on 16 July 2018 (see Fig. 5.10 for images), summed over all pixel (solid lines) and summed only over pixel above detection limit (dotted lines). The lower panel gives the fraction of the total signal which is below the detection limit. The relative position of the camera and wind direction limits the observation duration and total signal.

are comparable leading to different signal-to-noise ratios between the cameras. For camera UV4, the view of the puff was obscured by the release tower leading to an underestimation and slower increase of the signal in the beginning.

2. Trend: Assuming mass conservation and a perfect, noise-free detector, puffs moving away from the camera lead to an increasing projected pixel size and thus a decreasing total signal (see camera UV3, UV4 and UV5 in Figure 6.4). These cameras could observe the puffs for the longest time. With increasing distance and decreasing signal, the signal-to-noise ratio decreases until the puffs could no longer be tracked. For puffs moving perpendicular to the camera (camera UV1), the total signal stays constant. Tracking stopped due to the puff leaving the field of view rather than due to the decrease in signal.
3. Detection limit: The signal calculated based only on pixels above detection limit cuts away 99.7% of the noise pixels, assuming normal distributed noise. The signal hence appears smoother. Assuming that the background does not have a systematic bias, the difference to the signal based on all pixels, represents the amount of the total signal which is only due to column densities below the detection limit. For puff 25, shortly after the release circa 5% of the signal was below the detection limit for all cameras and the percentage increased to 25% after 60 s. Afterwards the relative noise became predominant due to the overall low signal. Here, it is worth to mention that most trajectories used for the ensemble analysis in chapter 7 did not exceed 60 s. The percentage of pixels below the detection limit is two times larger for cameras UV1 and UV6, which were positioned closer to the puff's trajectory. The

projection of the puff extended over more pixels in the image (compare Fig. 5.10: 100 pixels width for UV1 versus 30 pixels of UV5 at 30 s after release) and the pixels were therefore more likely to drop below detection limit.

4. Systematic errors: The background correction might have produced systematic biases if strong intensity gradients or clouds were present. The larger the ROI, the stronger the effect of such systematic biases. The size of the puffs increased as they dispersed but their projected size depended mostly on their relative moving direction/distance. For large puff projection as observed for camera UV1 and UV6 (100×100 pixels after 30 s) a comparable small bias of $\tau=0.003$, which was less than 10% of the detection limit (compare Fig. 5.1 and its discussion), could lead to an offset of $S_{tot}=1.14\cdot 10^{20}$ molec cm⁻² as the total signal was calculated as sum over all pixels (Eq. 6.2). Hence, if such a bias was present, it could explain 11% of the signal for camera UV1 in Fig. 6.4. When considering only pixels above the detection limit, biases lead to smaller systematic errors as less pixels were summed.

6.1.3 Projected trajectories of centre of mass

The CM positions were calculated according to Eq. 6.3 after applying a pixel threshold. The threshold was chosen such that it suppressed approximately the whole noise distribution by choosing 3σ where σ was the standard deviation of the background. A lower threshold, which does not cut-off most of the noise, would have led to a bias in the CM position as the distribution of the remaining noise pixels would lead to a CM which is shifted towards the centre of the ROI. Note, that a systematic offset in the background did not effect the calculation of the centre of mass, as long as it was isotropically distributed within the ROI. The threshold method is robust towards negative values and varying total ROI area. However, at the same time, it could lead to biased positions if the puff exhibited an extended, low-concentration tail below the threshold value. The trajectories of the CM projected to the image plane of the cameras can be seen in Fig. 6.5 for six example puffs. It is clear to see how the projection of the same 3D trajectories results in stretched or shortened trajectories in the image planes of the individual cameras. Perpendicular viewing cameras (UV1 in Fig. 6.5) observed the puffs until they left the field of view leading to clear trajectories. For the parallel viewing directions (UV3, UV4 in Fig. 6.5), the tracking stopped due to the decrease in total signal (see discussion of the total signal). Towards, the end of these trajectories, the uncertainty of the position of the CM increased up to 1 pixel. For a distance of 500 m, this error translates to a positional error of circa 19 cm (see table 4.2). Therefore, a running mean with a window size of few seconds was applied to the trajectories to smooth the trajectory ends.

6.2 Three-dimensional trajectories

The projected trajectories from the cameras were merged into a 3D trajectory using the method described in Dinger et al. [2018]: After correcting the time synchronisation and interpolating the trajectories to regular 250 ms intervals, the solid angle of the CM pixel for each camera was calculated based on the camera's position and pose. A least square fit was used to find the most likely intersection of the solid angles of all cameras. This is the 3D position of the CM.

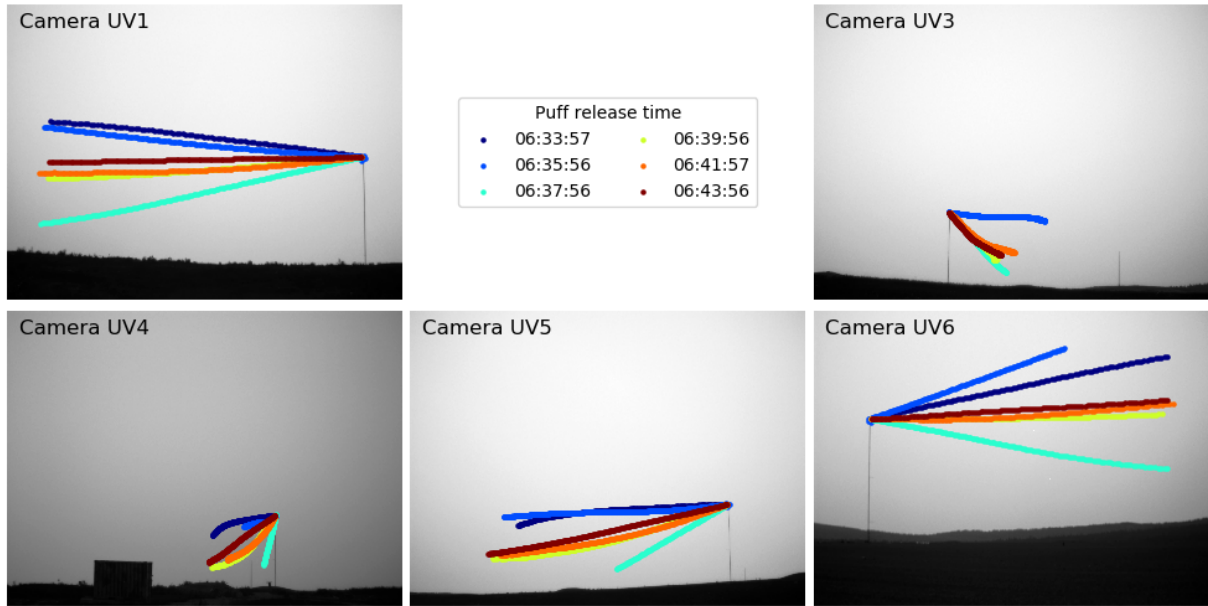


Fig. (6.5) Detected centre of mass trajectories of six puff releases on 16 July 2018 projected to the image planes of five SO₂ cameras. SO₂-free raw background images are shown as reference for the eye. Depending on the wind direction, the projected trajectories fill the entire field of view or only a small part of it.

The 3D trajectories were reconstructed for 18 selected puffs on 20 July 2017, 67 puffs on 15 July 2018 and 105 puffs on 16 July 2018. The other puff release in 2017 and 2018 were obtained during periods of persistent sparse to dense cloud cover and the retrieval would contain significant work to correct each puff individually. Due to the short time passed since the 2019 campaign, only preliminary analysis has yet been performed which will not be presented in the scope of this thesis. For the puffs presented in Fig. 6.5 the resulting 3D trajectories are shown in Fig. 6.6. The trajectories showed small jumps in the order of few metres when the trajectory from one camera ends. This could be caused by uncertainties of the camera pose, the remaining noise in the projected trajectories or faulty distortion correction. The fit error for the trajectories is circa 0.5m close to the release and up to 3m for later times. An error of 3m can be assumed as good estimate of the reconstruction error. The pixel scaling factor $s(d)$ has the same relative error as the distance, and as such the resulting estimated relative error of the puffs' mass and spread (scaling with $s^2(d)$) is $\sqrt{2}\frac{\Delta d}{d} = 1\%$ for a distance of $d=500$ m. The 3D trajectories could be reconstructed for up to 58 metres and 20 seconds in 2017 and 400 metres and 90 seconds in 2018. The duration of length of the individual trajectory varies strongly (see Fig. 6.7) and depends mainly on the puff direction and wind velocity.

6.2.1 Mass conservation

The mass was calculated as the product of the pixel scaling and the total signal according to Eq. 6.4. Assuming that no SO₂ was converted to sulphuric acid on the observed time scales of few minutes, all deviations from a constant, conserved mass were due to uncertainties in the measured total signal and the reconstructed 3D trajectories. Therefore the previous discussion of the total signal and the uncertainty of the 3D trajectory

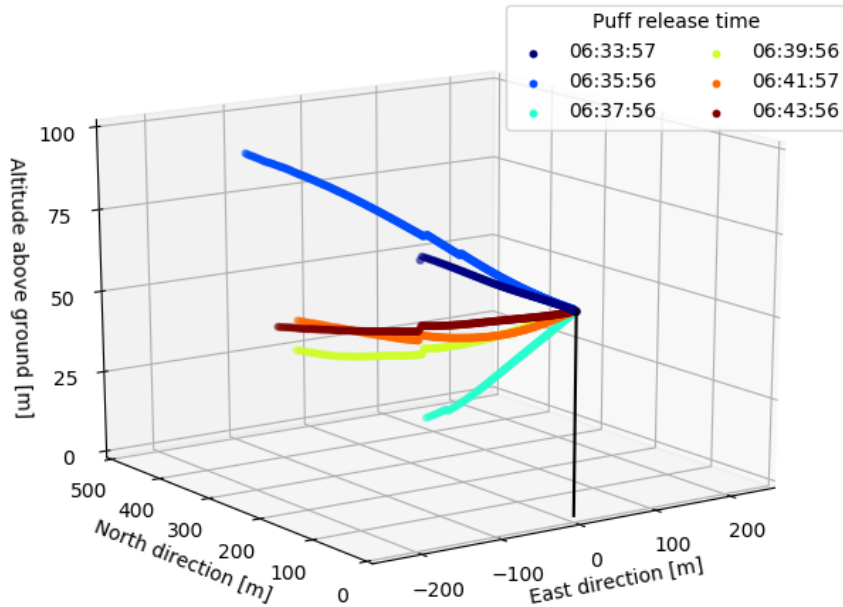


Fig. (6.6) Reconstructed 3D trajectories of six puffs on 16 July 2018. The corresponding projected trajectories are shown in Fig. 6.5.

reconstruction applies to the measured mass as well.

Figure 6.8 shows the mass of puff 25, which was released on 16 July 2018 during cloud-free conditions. After the initial increase, the mass continues to increase until it reaches an approximately constant value after 15s-20s depending on the camera. This could be a sign that the applied, linear SO_2 calibration failed as long as large optical densities were observed while the puff was still compact. For cameras UV3, UV4 and UV5 the retrieved puff mass coincided at 24g and agreed with the estimate for the released mass, $m_{\text{released}}=23\pm 2$ g, estimated from pressure difference in the canister. The mass reconstructed from cameras UV1 and UV6 (blue and brown in Fig. 6.8) systematically overestimated the puff mass by up to 20%. The signal from camera UV1 and UV6 had a higher percentage of signal due to pixels below the detection limit up to 20% (compare Fig. 6.4). This could be an indicator that the overestimation of the mass is due to a positive offset in the background pixels for these cameras. The retrieved puff masses were reasonably well conserved for up to 1 minute after release. Then, the puff was either lost (cameras UV1 and UV6) or the masses decreased rapidly to 50% of their original values.

Comparable initial saturation was observed for most analysed puffs. Figure 6.9 shows the maximum recorded optical density value within the region of interest of the cameras for six puffs. The variability between the cameras and puffs is large. Very high values ($\tau > 1$) were observed for the closest cameras UV6, UV1 and UV4 which persisted up to 15s. From the radiative transfer simulations in Kern et al. [2013], a underestimation of circa 30% can be expected for $\tau=1$ if no aerosol is present. After 20s, all cameras recorded for all but one puffs maximum values below 0.6. As the saturation depends on the puff mass and distance to the camera, it is meaningful to treat the saturation individually for each camera and puff. It was defined that the puff measurements for which the retrieved mass was within a $\pm 10\%$ tolerance range of the constant detected mass value were considered not affected by saturation (in the beginning) and dilution

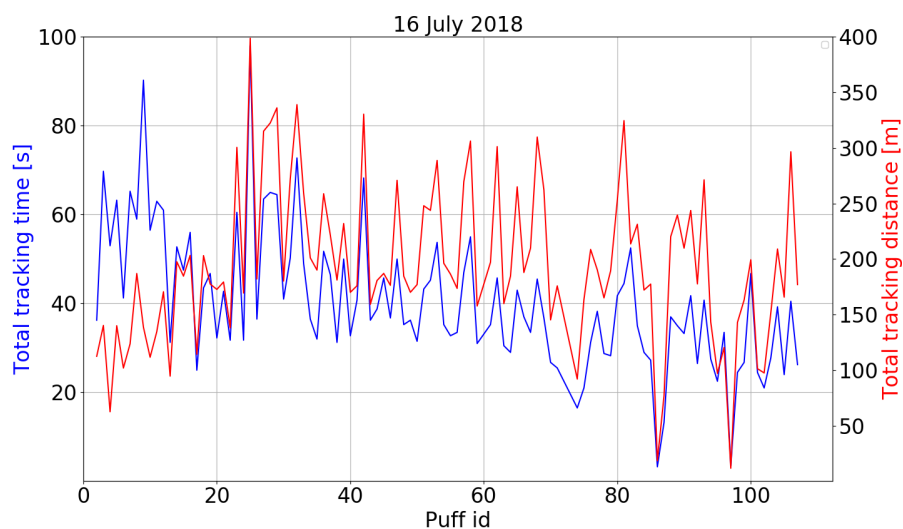


Fig. (6.7) Duration and length of all reconstructed 3D trajectories on 16 July 2018. Puffs 86 and 97 were low-mass cleaning puffs and could not be tracked for a long time.

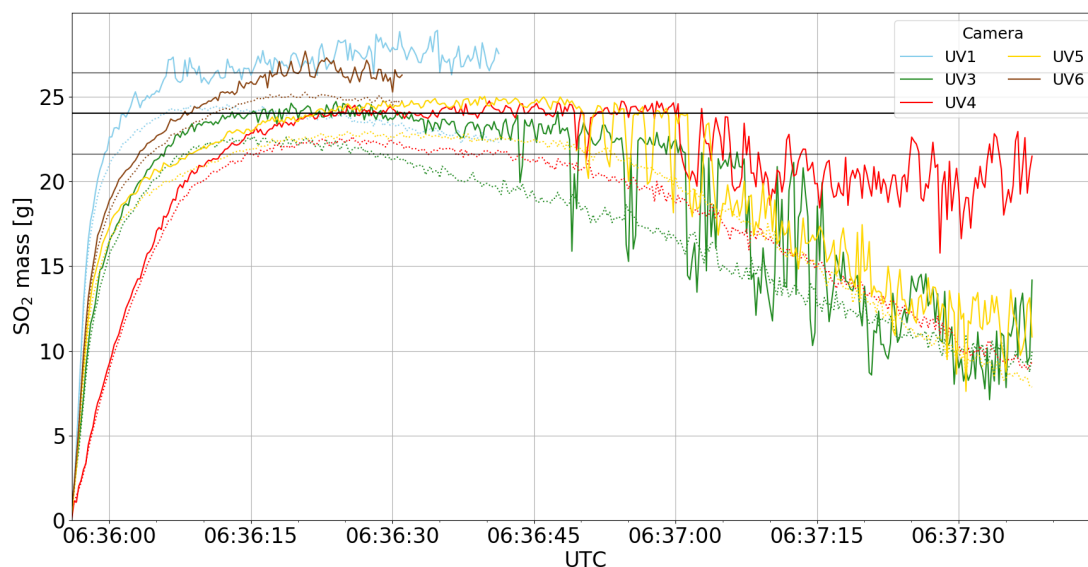


Fig. (6.8) Puff mass in the region of interest for puff 25 on 16 July 2018. These masses correspond to the scaled total signal shown in Fig. 6.4. The total mass of cameras UV3, UV4 and UV5 coincided at 24 g (black line) and agreed with the estimated released mass of 23 ± 2 g. A 10% tolerance window (grey lines) was used to select times for which the correct mass was reconstructed.

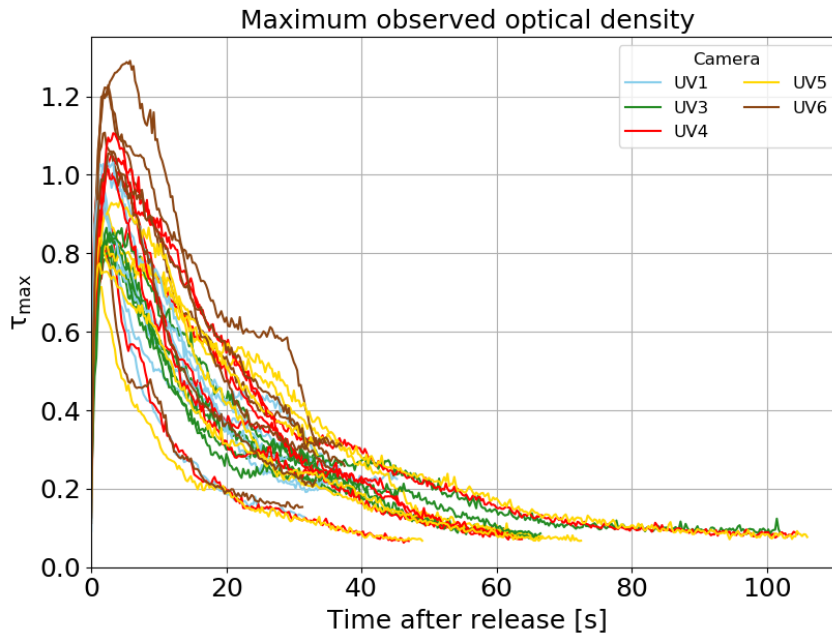


Fig. (6.9) Maximum observed optical density within the ROI for the six puffs shown in Fig. 6.5 and 6.6. For pixels with optical densities above 0.75, the saturation is significant. Depending on the puff and camera, saturation effects up to 20 s after the release can be expected.

below the detection limit (in the end). The constant detected mass value was estimated for each puff based on the camera-averaged mass value at 15 s after release. This mass threshold also assured that puffs affected by clouds in the ROI or biases in the background correction were not considered.

The saturation affects only the pixels in the puffs' centres because the pixels at the puff edges recorded significantly lower optical densities close to the detection limit. The mass in the puff centre is underestimated leading to a perceived stronger spread (given by the variance) and hence underestimated puff spread. However, it is assumed that the centre of mass is only mildly affected by the mass saturation. This is the case when most mass is concentrated in the puff centre compared to the puff edges which is expected at short times after release.

6.2.2 Puff spread

Figure 6.10 shows the spread (Eq. 6.7 - 6.9) of puff 25 on 16 July 2018 along pixel rows, pixel columns and along the eigenaxes of the projected mass distribution. Only values, for which the mass conservation was satisfactory fulfilled ($\pm 10\%$ of constant mass, see section 6.2.1), were considered for the spread. Additionally, the spread was calculated based only on pixels above the detection limit. Obviously, as the pixels with SO_2 SCDs below the detection limit were located at the puff edges, this spread can be interpreted as a lower limit. This lower spread was less affected by noise and biases in the background correction. The spread along the eigenaxes was only calculated for the pixel above detection limit as the calculation (Eq. 6.8) could not treat negative values (as present in the noise) correctly. The spread along the eigenaxes can be used to detect and correct the rotation of the puffs

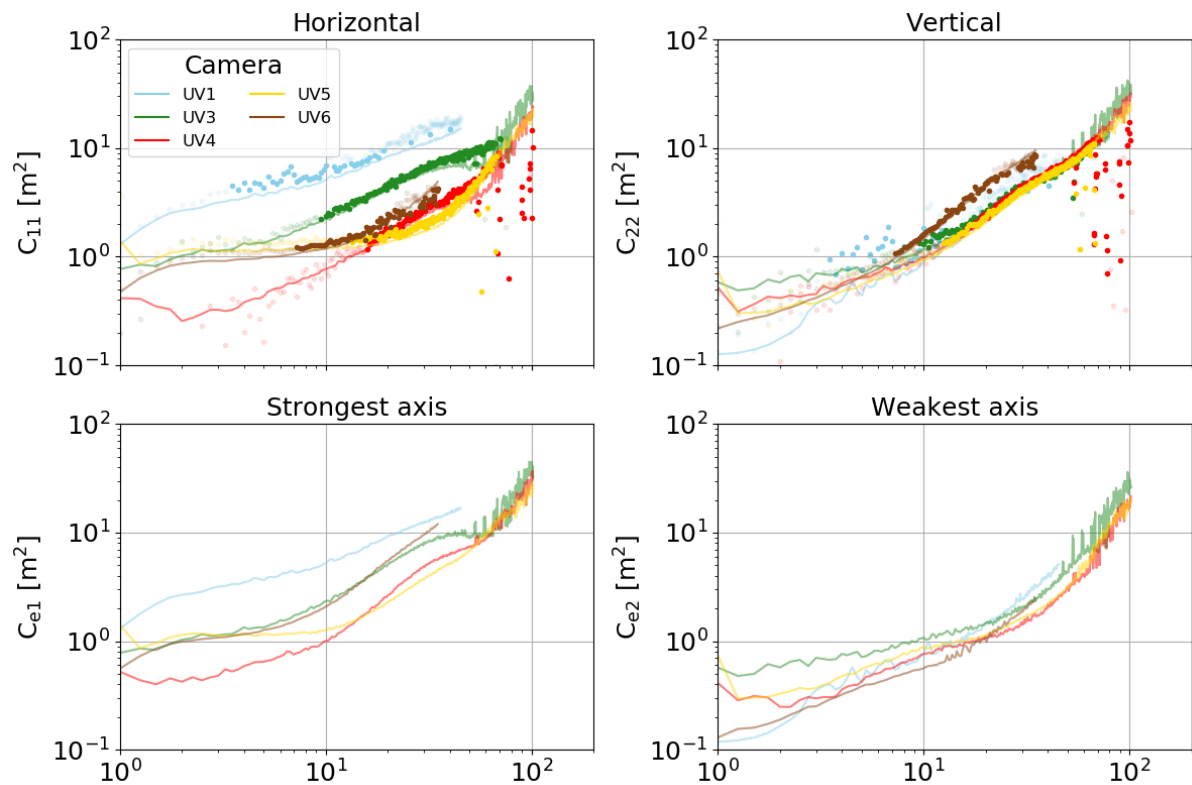


Fig. (6.10) Spread of mass around the centre of mass for puff 25 on 16 July 2018. The four panels show the spread in horizontal and vertical image direction and along the axes of strongest and weakest variance. Full symbols (●) represent data for which a valid mass was estimated and empty symbols (○) are points for which the estimated mass was outside the tolerance window of 10%. The lines are the spread based only on pixels above the detection limit. As such they represent a lower limit of the puff spread. For the eigenvalue composition (lower panels) only pixels above the detection limits were considered as the decomposition required positive pixel values.

in the image plane.

The puff spreads are projections of the 3D SO₂ concentration distribution to the cameras' object planes. This means, that each camera detected the spread perpendicular to the camera's optical axis. For puff 25, the viewing direction of camera UV1 was approximately perpendicular to the propagation direction of the puff. Therefore, camera UV1 observed the spread in along wind and vertical direction. Analogously, camera UV3 observed the spread in cross wind direction and cameras UV4, UV5 and UV6 observed the puff under a slant angle. The elongation of the puffs in wind direction is clearly visible in the horizontal spread with larger values for the along wind camera compared to the cross wind camera.

In the vertical, the cameras observed comparable projections of the vertical puff extensions because of comparable elevation angles (5° and 11°). Indeed, the vertical spread for cameras UV1-UV5 coincided. Merely, the spread for camera UV6 was larger which can be explained by the trajectory of the puff moving towards (and above) camera UV6 and therefore leading to a larger projection to the vertical image plane.

6.2.3 Flow direction and velocity at the release

The average horizontal and vertical moving directions were calculated by fitting a linear function to the first 10 seconds of each 3D trajectory projected to the horizontal plane and the plane spanned by the horizontal distance ($\sqrt{x^2 + y^2}$) and the altitude, respectively. The moving direction was defined geographically as 0° towards north and increasing towards east. The mean flow velocity was estimated similarly for the first 10 seconds after release. A linear fit was estimated to the relation between time after release and absolute distance ($\sqrt{x^2 + y^2 + z^2}$) of the centre of mass to the source.

In Fig. 6.11, the results of the flow analysis based on the trajectories are compared to 5-min averages obtained from the eddy-covariance measurements of the sonic anemometer close to the source. The centre of mass velocities agree with the wind velocities at the source. That confirms the assumption that the average wind field is homogeneous over the observed distances.

6.2.4 Rotation to mean flow system

The trajectories were reconstructed in geographic coordinates (East, North, Altitude). However, for the analysis of turbulent dispersion, it is convenient to align the trajectories with the mean flow. The coordinate system of the turbulent flow (x, y, z) is defined based on the the mean wind direction $\bar{\mathbf{u}} = (\bar{u}, \bar{v}, \bar{w}) = (\bar{u}, 0, 0)$. Then the geographic trajectories $(x_{geo}, y_{geo}, z_{geo})$ can be rotated by the mean wind direction ϕ_{geo} according to

$$(x, y, z)^T = \mathbf{R}(\phi_{geo}) \cdot (x_{geo}, y_{geo}, z_{geo})^T \quad (6.10)$$

$$\mathbf{R}(\phi_{geo}) = \begin{bmatrix} \cos(-\phi_{geo} + \frac{\pi}{2}) & \sin(-\phi_{geo} + \frac{\pi}{2}) & 0 \\ -\sin(-\phi_{geo} + \frac{\pi}{2}) & \cos(-\phi_{geo} + \frac{\pi}{2}) & 0 \\ 0 & 0 & 1 \end{bmatrix} \quad (6.11)$$

to along wind, cross wind and vertical components. The mean flow direction can be either taken as the mean wind direction from the eddy covariance measurements at the source or directly from the mean propagation direction of the puffs.

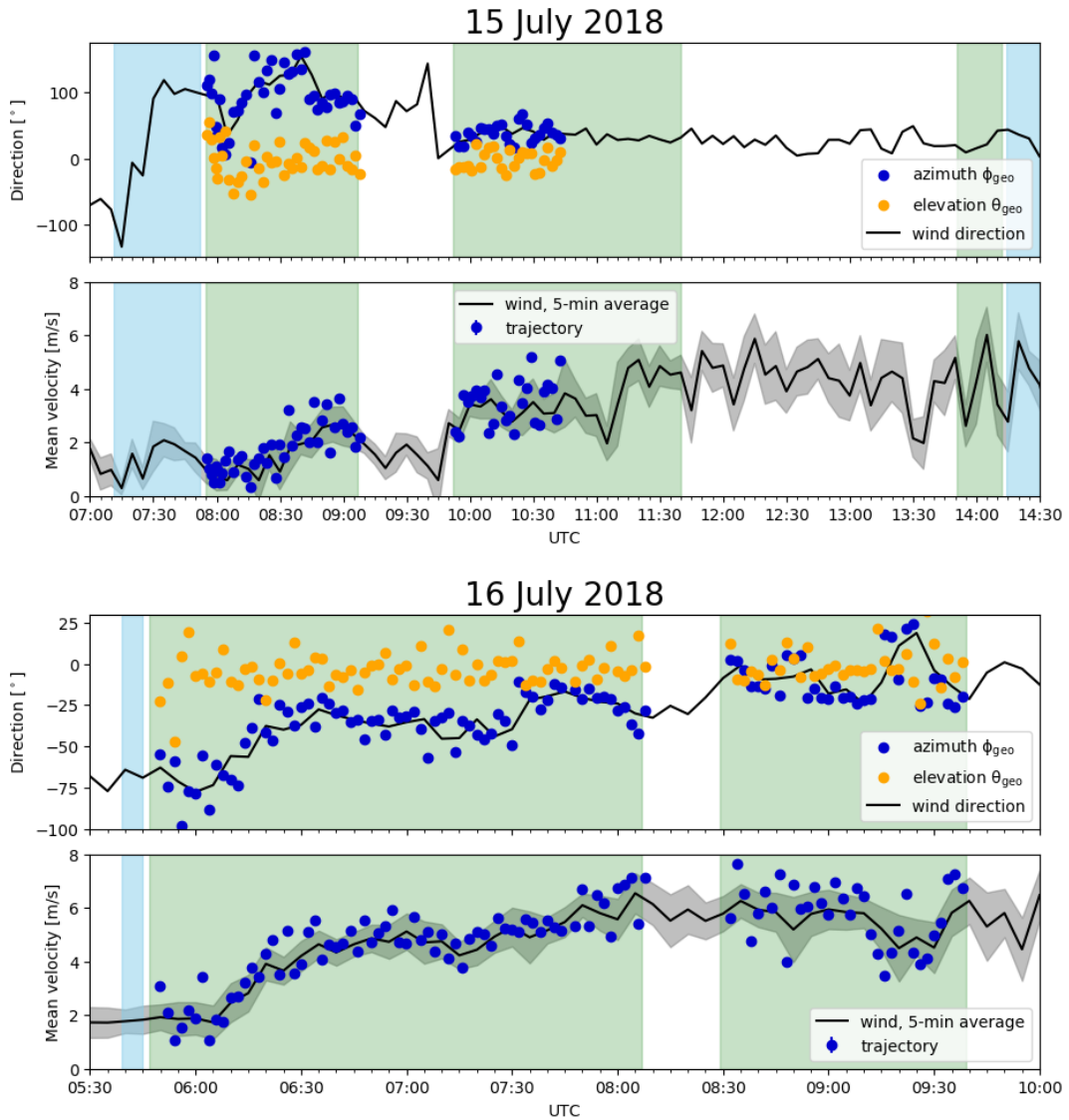


Fig. (6.11) Mean flow direction and velocity reconstructed from the puff trajectories and from the sonic anemometer close to the source location on two days. Shaded areas indicate periods of continuous (blue) and instantaneous (green) release experiments. On 15 July 2018 not all puff releases were analysed due to the increasing cloud cover. Sonic anemometer data courtesy to H. Ardeshiri and M. Cassiani.

6.2.5 Center of mass velocities

After rotation of the trajectories, the components of the centre of mass velocity were calculated as the time-derivative of the travelled along wind, cross wind and vertical distances. The discrete jumps in the 3D trajectories caused spikes in the derivative which were filtered out. Figure 6.12 shows the velocity components for six puffs on 16 July 2018. The mean wind direction for rotating the trajectories was taken from the eddy covariance data. The elongated puff shape during release become obvious in the velocities: While gas is released the centre of mass velocity is underestimated as new gas arrives at the release point. After circa 3 s, the velocities have reached a nearly constant value and can be assumed to represent the centre of mass velocity of the full released puffs.

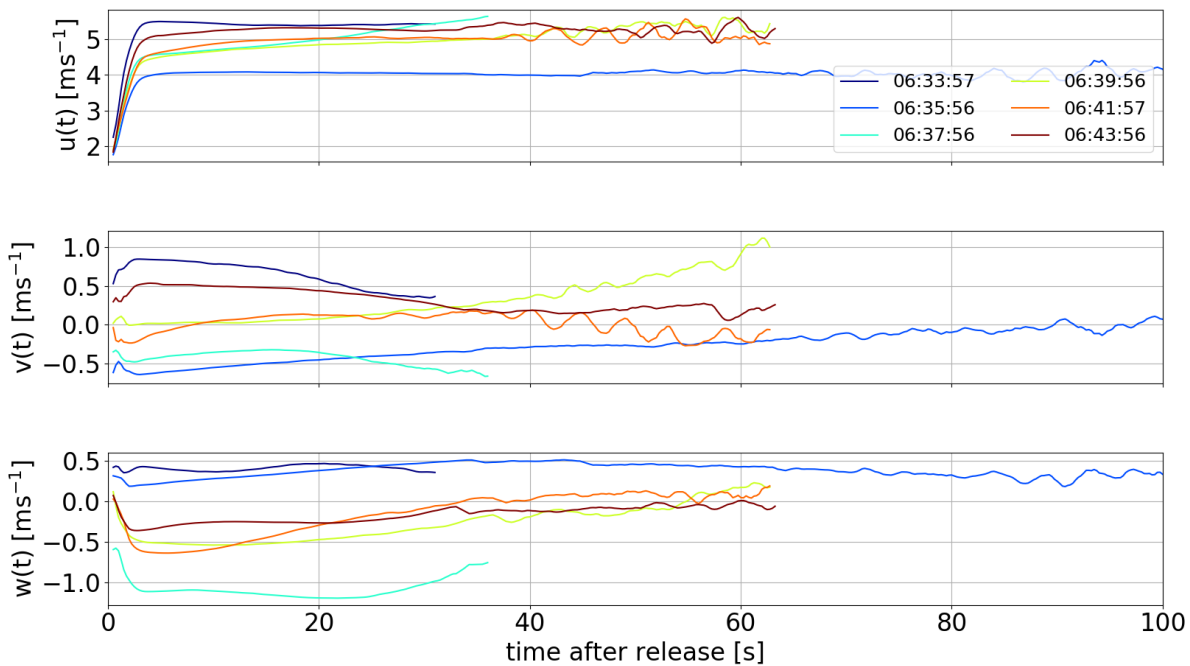


Fig. (6.12) Centre of mass velocity components for six puffs on 16 July 2018 derived from the 3D trajectories after rotation with the mean wind.

Chapter 7

Statistical analysis of puff ensembles

In the last chapter, the dispersion of single puffs was analysed. Ensembles of several puffs can be used to estimate statistical parameters of the turbulent dispersion as long as the puffs were released during comparable conditions. In the following, several periods of nearly-stationary conditions were identified in 2017 and 2018 based on the eddy covariance data and the releases of each period were regarded as a statistical ensemble (section 7.1). The statistical treatment allows for analysis of the mean displacement (relative dispersion, meandering and absolute dispersion) of puff ensembles (section 7.2) and the centre of mass velocity correlations (section 7.3).

7.1 Time intervals of nearly-stationary turbulence

Based on all available time series from the eddy covariance (EC) systems and the puff trajectories, 5 periods of nearly-stationary turbulence were identified for which sufficient many puff releases were performed. Figure 7.1 relates the selected time intervals in 2018 to the 5-minute averaged data from the eddy covariance (EC) measurements. Besides the directly measured wind velocity and heat and moisture fluxes, their time series allowed for the calculation of i.a. turbulence intensity, friction velocity, mean energy dissipation rate and the Obukhov length. Details on the calculation can be found in appendix A.2. Independently, the propagation direction and velocity of the puffs were retrieved from the centre of mass trajectories (Fig. 6.11). The 3D trajectories for the intervals are shown in Fig. 7.2 and 7.3 and Tables 7.1 and 7.2 summarise the intervals based on puff trajectories and EC measurements, respectively. Both methods gave comparable wind direction and velocity for the intervals.

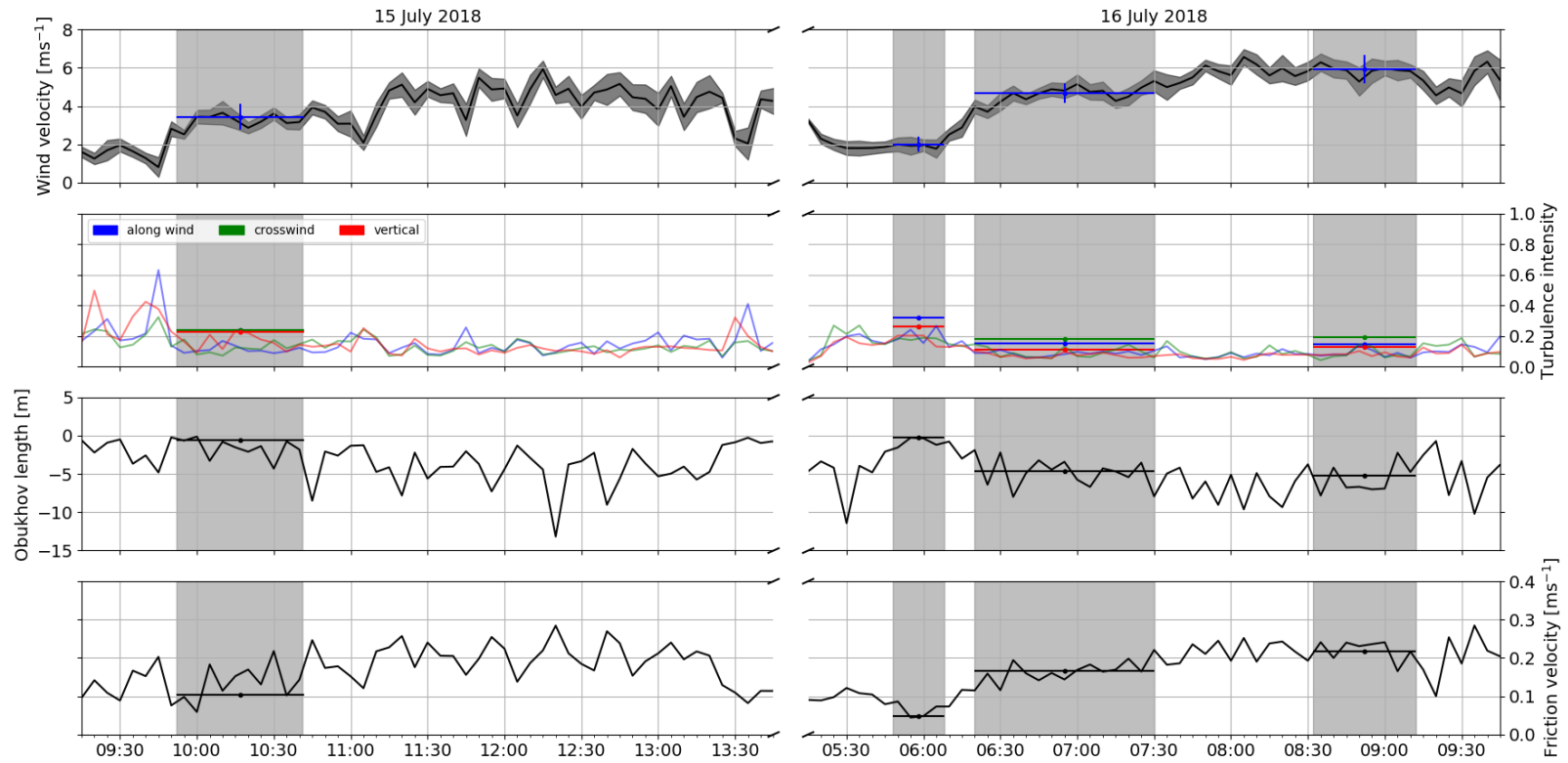


Fig. (7.1) Overview of meteorological parameters (wind velocity, turbulence intensity, Obukhov length, friction velocity) based on 5-minute averages derived from the eddy covariance measurements on 15 and 16 July 2018. The values were also derived for averages over the selected time intervals (grey shaded areas) according to Table 7.1. Data provided by H. Ardeshiri and M. Cassiani.

Table (7.1) Intervals of nearly-stationary conditions: EC measurements. Data provided by H. Ardeshiri and M. Cassiani.

Parameter			20-1	15-1	16-1	16-2	16-3
Date			20/07/2017	15/07/2018	16/07/2018	16/07/2018	16/07/2018
UTC time			10:27 - 10:32	9:52 - 10:42	5:48 - 6:08	6:20 - 7:30	8:32 - 9:12
averaging time	T	[min]	5	50	20	70	40
mean direction	ϕ_{geo}	[°]	-	38	289	323	349
mean velocity	\bar{u}	[m s ⁻¹]	5.2	3.4	2.0	4.7	5.9
velocity variance	σ_u^2	[m ² s ⁻²]	2.3	0.67	0.41	0.50	0.74
	σ_v^2	[m ² s ⁻²]	0.86	0.67	0.28	0.71	1.26
	σ_w^2	[m ² s ⁻²]	0.28	0.61	0.28	0.27	0.60
turbulence	i_u		0.29	0.24	0.32	0.15	0.15
intensity	i_v		0.18	0.24	0.26	0.18	0.19
	i_w		0.10	0.23	0.26	0.11	0.13
energy	ϵ_u	[m ² s ⁻³]	0.015	0.00366	0.0235	0.00179	0.00384
dissipation	ϵ_v	[m ² s ⁻³]	-	0.00295	0.0162	0.00176	0.00344
	ϵ_w	[m ² s ⁻³]	-	0.00255	0.0068	0.00146	0.00265
friction velocity	u_*	[m s ⁻¹]	0.249	0.103	0.048	0.165	0.217
Obukhov length	L	[m]	-6.22	-0.56	-0.28	-4.60	-5.21
Richardson flux number	R_f		-0.988	6.957	-0.292	-0.145	-0.143

Table (7.2) Intervals of nearly-stationary conditions: Puff trajectories

Parameter	20-1	15-1	16-1	16-2	16-3
Date	20/07/2017	15/07/2018	16/07/2018	16/07/2018	16/07/2018
UTC time	10:27 - 10:32	9:52 - 10:42	5:48 - 6:08	6:20 - 7:30	8:32 - 9:12
number of puffs	6	26	11	35	20
direction ϕ_{geo} [°]	-	39	290	324	349
velocity $\langle u \rangle$ [m s ⁻¹]	-	3.5	2.0	4.8	6.1

The periods spanned between 5 min and 70 min and contained between 6 and 35 puffs each with different meteorological conditions. Therefore, the periods allow for observation of turbulent dispersion under different aspects.

Interval 20-1 on 20 July 2017 10:27 - 10:32 This interval was limited to 6 puffs due to cloudy conditions and was therefore only used for demonstration purposes in Dinger et al. [2018]. In 2017, the low release height of 9 m led to particularly high variances of the wind velocity and the energy dissipation rate. The puffs were released within 60 s and could be observed up to 50 m and for 15 to 20 s. The relative dispersion could be observed while the velocity autocorrelations could not be studied due to the short observation time.

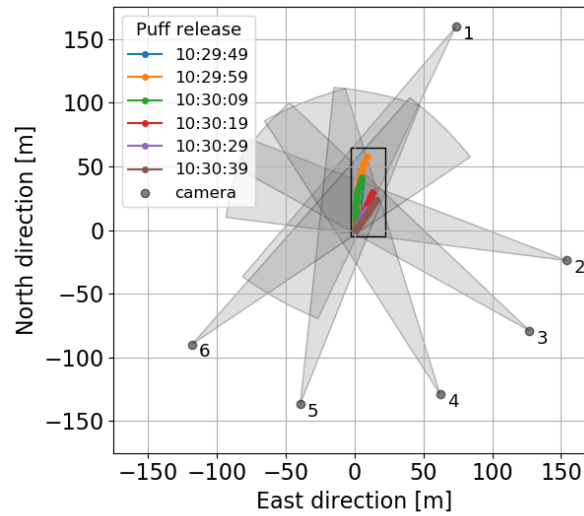


Fig. (7.2) Interval of nearly-stationary conditions in 2017: Map of centre of mass trajectories. The cameras' field of views are indicated in grey. Adapted from Dinger et al. [2018].

Interval 15-1 on 15 July 2018 9:52 - 10:42 The interval was during a period of nearly homogeneous, isotropic turbulence under thermally neutral stability ($L=-0.56$ m) as indicated by the comparable values of the three components of the velocity variance (0.61-0.67 m²s⁻²). The puffs moved towards Northwest and could be observed nearly perpendicular to their moving direction by cameras UV3 and UV6, which is preferable when analysing the relative dispersion of the puffs. Some clouds were present during the interval and the puffs could be tracked for between 35 s and 70 s. The long interval duration of 50 min provides a good statistic of 26 puffs for the analysis.

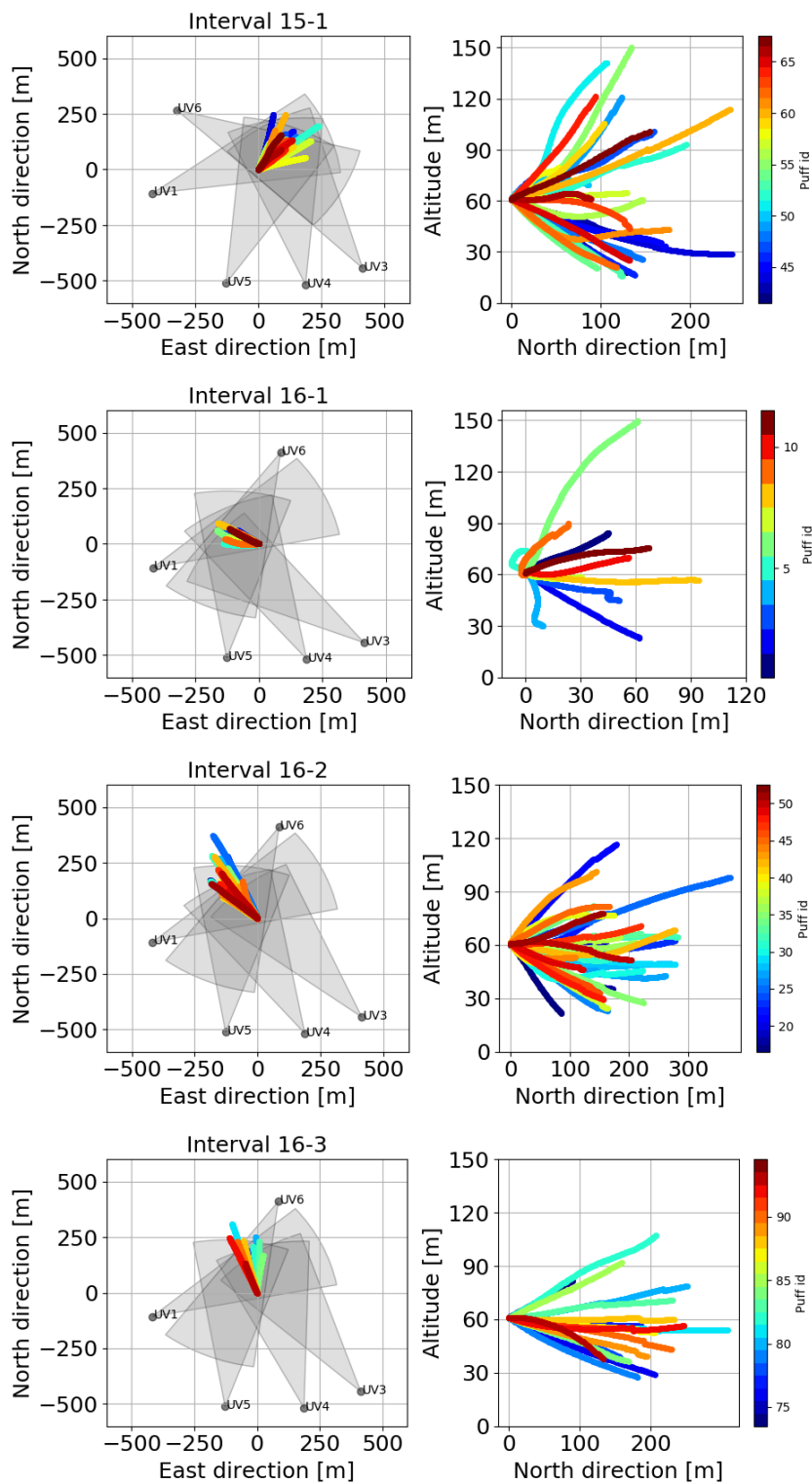


Fig. (7.3) Intervals of nearly-stationary conditions in 2018: Map of centre of mass trajectories projected to the North-East- and North-Altitude-planes. The cameras' field of views are indicated in grey. The intervals contain different amounts of puffs and the puff id refers to the release within that day.

Interval 16-1 on 16 July 2018 5:48 - 6:08 During the early morning, wind velocities were low and turbulence intensity was high. The puffs were transported slowly with the mean wind and could be observed for a long time up to 90 s within the cameras' field of views. Hence, long CM trajectories, desirable for the analysis of the velocity autocorrelations, are available. However, the light intensity in the early morning was low and exposure times were set cautiously low to account for the rapidly increasing intensity. In consequence, the image series had a two-times lower time resolution compared to the other intervals and a higher background noise affecting the accuracy of CM positions and relative dispersion. Further, with only 11 puffs this time interval was the shortest of 2018 and statistics have to be applied with care.

Interval 16-2 on 16 July 2018 6:20 - 7:30 Between interval 16-1 and 16-2, the wind velocity more than doubled, the turbulence intensity dropped and the surface layer became weakly unstable ($L=-4.60$ m). Then, the conditions remained nearly stationary. This is the longest selected interval with 35 puffs providing good statistics. Due to the higher wind velocity, most CM trajectories were tracked for between 30 s and 50 s.

Interval 16-3 on 16 July 2018 8:32 - 9:12 During the last interval on 16 July 2018, wind velocities increased further to a mean value of 5.9 m s^{-1} leading to short tracking times of the CM trajectories (generally below 35 s). Contrary to all other intervals, during 16-3 all puffs were released with the same mass (compare chapter 4) leading to a more comparable source distribution.

The puff ensembles of all intervals share one weakness which can lead to systematic biases when analysing the statistics: Puffs trajectories towards "extreme" directions are lost first. The cameras observed a limited volume downstream of the release. Their poses were adjusted to observe *most* of the puffs for the longest possible time. However, especially during strong turbulence, some of the trajectories differed strongly from the mean trajectory. E.g. some puffs dropped towards the ground usually causing the cameras to observe it in front of topography instead of clear sky, others moved particularly towards the west. These puffs were usually tracked for a considerably shorter time than the other puffs and therefore limited the total observation time of the entire ensemble. It is desirable that the total tracking is sufficient long to observe the relative dispersion independent of the initial source (compare Eq. 2.22 for source time scale) and to extend over the Lagrangian time scale. Ignoring the shortest trajectories increased the total observation time, however selected systematic straight trajectories. The puffs were regularly released every 2 minutes within the intervals in 2018 (every 10 seconds in 2017). Therefore their ensembles were a regularly sampled sub ensembles of the trajectories of all air parcels. Considering only trajectories with a minimum duration will remove the extreme cases which were caused by large eddies and most likely led to an underestimation of i.a. the meandering (the variance of the trajectories). However, it can be assumed that the relative dispersion is only slightly affected by ignoring trajectories as the relative dispersion is driven by eddies of comparable size as the puffs which are not systematically removed.

7.2 Turbulent dispersion

7.2.1 Relative dispersion

Figures 7.4 and 7.5 show the relative dispersion for 2017 and 2018, respectively, for single puffs averaged over all cameras and the ensemble averages. Only puff spreads for which the mass was conserved were considered (see section 6.2.1).

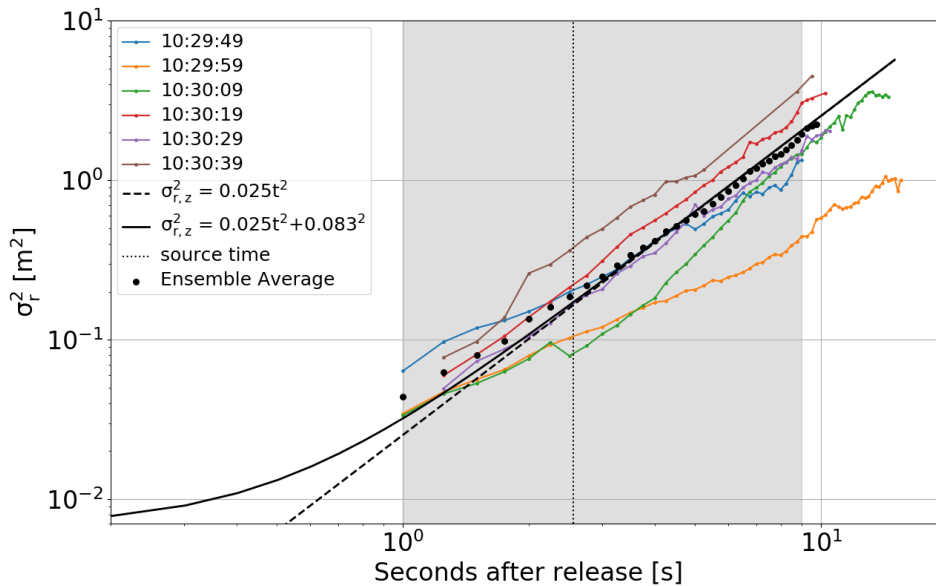


Fig. (7.4) Vertical relative dispersion for interval 20-1. A quadratic relation was fitted to the ensemble average between 1 s and 9 s (grey area) to obtain the source size and source time scale. Reproduced from Dinger et al. [2018].

Except for the vertical component of interval 16-1, the relative dispersion accelerated following a t^2 -scaling which is characteristic for the source-dominated regime of the inertial subrange [Batchelor, 1952]. After several tens of seconds, the measured increase in puff size stagnated as the signal of more pixels at the puff edges dropped below the detection limit leading to an underestimation of the size. Almost all puffs remained smaller than $\sigma_r=10$ m during the entire duration of observation (up to 100 s). However, it was not possible to observe the Richardson-Obukhov t^3 -scaling (Eq. 2.26), which would have been required for an estimate of the Richardson-Obukhov constant, due to the limited length of the time series. Merely, the vertical component of interval 16-1 showed a t^3 -scaling. However, the dent at 15 s and lack of typical t^2 -scaling raise doubt whether the poor statistics of 11 puffs for this intervals was sufficient to correctly capture the relative dispersion. The rotation of single puffs might have led to the dent at 15 s.

The elongated shape and the rotation posed challenges to the analysis of the relative dispersion as it was generally not possible to distinguish if an increase in projected puff size was due to puff dispersion or a rotation without a full, tomographic reconstruction of the SO_2 concentration distribution. Bianchi et al. [2016] modelled via direct numerical simulation the evolution of non-spherical puffs in isotropic turbulence and showed that, while becoming more spherical, they never fully reach full sphericity within the inertial subrange. However, they found that the “concentration statistics is only mildly affected

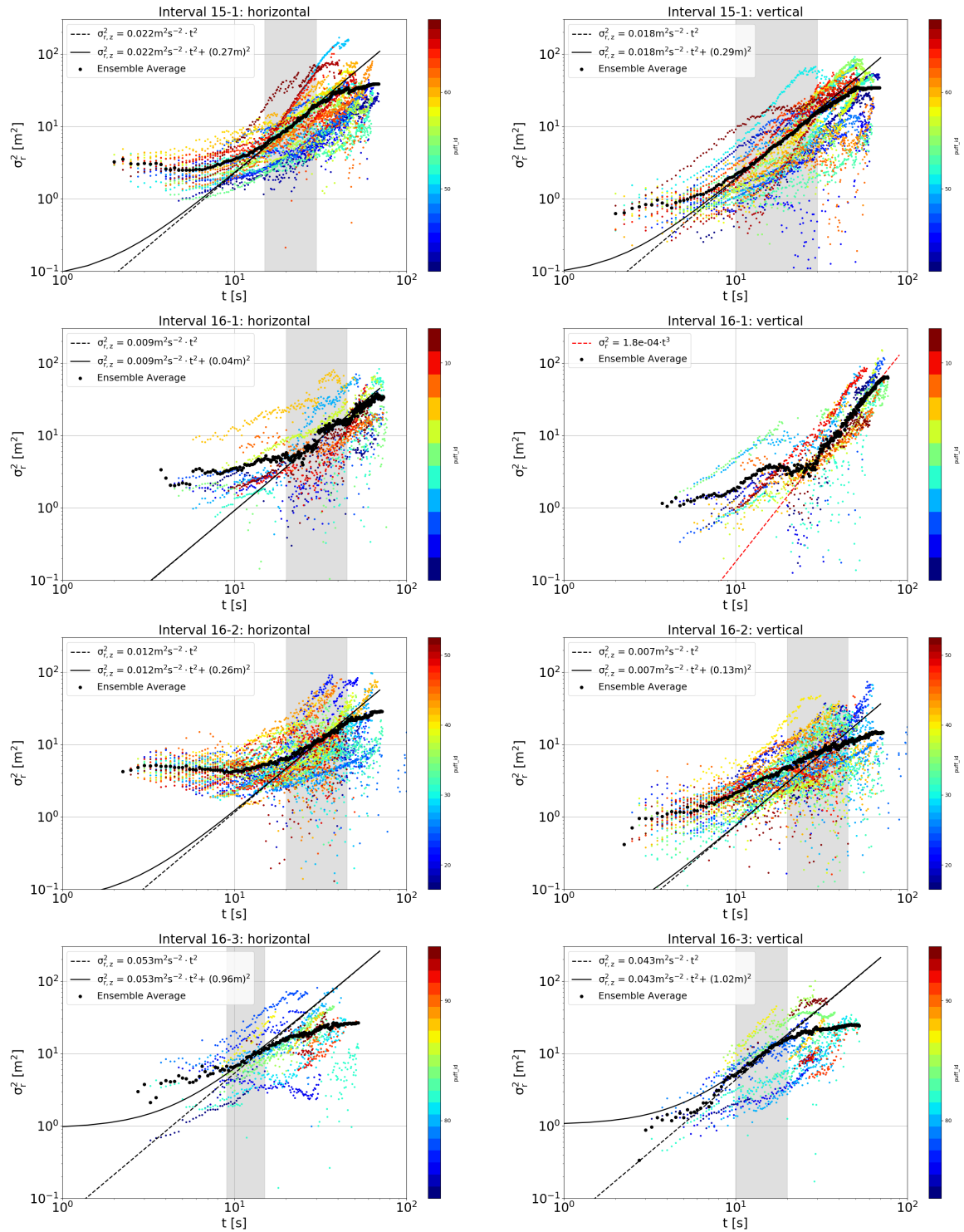


Fig. (7.5) Relative dispersion for the ensemble average (black) and for single puffs (coloured). The relative dispersion of the single puffs was averaged over the cameras. Quadratic (black) or cubic (red) scaling was fitted to the ensemble average when possible.

by the asphericity of the puffs.”

While for long times, the elongation can be therefore neglected for analysing the relative dispersion, for short times, the cameras observed different effective source size in the horizontal due to their orientation to the moving direction of the puffs (compare section 6.2.2). For short times as observed, only a mixture of the along wind and cross wind dispersion is observed. For the vertical component, all cameras observed the vertical relative dispersion due to comparably small elevation angles. The vertical source size and time scale were estimated by fitting a linear function with slope 2 to the linear slope in the log-log-plot (dashed line and grey area in Fig. 7.5)

$$\ln(\sigma_r^2) = 2 \cdot \ln(t) + a \quad (7.1)$$

where the fit parameter was given according to Eq. 2.24 as

$$a = \ln(6^{-2/3} \cdot \frac{11}{3} \cdot C_k \cdot \epsilon^{2/3} \cdot \sigma_{r,0}^{2/3}) \quad (7.2)$$

with the Kolmogorov’s constant for the longitudinal structure function $C_k=2$ [see e.g. Franzese and Cassiani, 2007] and the measured mean rate of energy dissipation ϵ (see Table 7.1). From Eq. 7.2, the source size $\sigma_{r,0}$ and the source time scale $t_s = (6 \cdot \sigma_{r,0}^2 / \epsilon)^{1/3}$ were calculated and the resulting initial relative dispersion (Eq. 2.24) is shown as solid line in Fig. 7.4 and 7.5. The results are given in Table 7.3.

Table (7.3) Vertical source size and derived time scale

Parameter	20-1	15-1	16-1	16-2	16-3
source size	8.3 cm	29 cm	-	13 cm	102 cm
source time scale	2.6 s	10.5 s	-	7.5 s	24 s

For the interval in 2017, the estimated source size was 8.3 cm and compared to the radius of the release outlet (6.25 cm). In 2018, the release was positioned vertically and the vertical source size depended on the wind velocity and the duration of the release itself. The vertical component of interval 15-1 showed an extended and clear t^2 -expansion with estimated source size of 29 cm. This value agreed with direct size estimates of single puffs from the images suggesting a vertical size of circa 50 cm at 2 s after release (see Fig. 5.10 and 6.10). Interval 16-1 did not show such scaling and no estimate was possible (see above). For interval 16-2, single puffs showed clear t^2 - and t^3 -scaling but other puffs even decreased in observed size leading to an average relative dispersion with slower expansion than t^2 in the vertical component. For interval 16-3, the wind velocity was high and the observed trajectories were particularly short with few observations within the mass threshold. The source size was estimated to 102 cm. This is counter-intuitive to the simple picture that high wind velocities (as observed during 16-3 compared to 15-1) at the release led to a stronger elongation of the puff and hence smaller vertical source size. The high estimated value could be caused by rotation of the puffs such that the elongation was observed in vertical direction. Alternatively the estimated value of ϵ might not be representative for the interval due to the long averaging time and probably changing conditions of the surface layer. This would agree with the fact that the measured relative dispersion up to 10 s after release was systematically lower than the estimated curve according to Eq. 2.24.

In summary, the time scales ranged between 7.5s and 24s for 2018 and were only marginally smaller than the total trajectory lengths. Therefore, due to the unintended elongated shape, the source regime was observed over the entire duration of reliable signal. In consequence, the Richardson-Obukhov-scaling (t^3 -scaling) of the inertial subrange could not be observed in the puff ensembles from neither 2017 nor 2018. If the time series would be longer, the observation of the Richardson-Obukhov scaling would allow for an experimental estimate of the Richardson-Obukhov constant; an important model parameter whose value still is not exactly known [see e.g Franzese and Cassiani, 2007]. Hence, it could be demonstrated that the experimental setup and methodology in principle allows for such an estimation if the released puffs have a smaller, or ideally round shape and if the time series of the relative dispersion is longer.

7.2.2 Centre of mass meandering

The meandering was calculated as the variance of the distribution of the centre of mass trajectories after rotation to the coordinate system of the mean flow defined based on the eddy covariance measurements (Table 7.1). The rotated CM trajectories and the meandering in cross wind and vertical direction for the longest interval (16-2) can be seen in Fig. 7.6. The included CM trajectories have different observation times, leading to a decreasing number of trajectories for the calculation of the variance: the shortest two trajectories were reconstructed for 25s and 30s while 16 of the 35 trajectories could be observed for more than 45s. The meandering was calculated for the entire ensemble and for the sub-ensemble containing only the 16 trajectories, which could be observed for at least 45s. For trivial reasons, the curves coincide for times above 45s. As discussed in section 7.1, the observations of the shortest trajectories stopped because the puffs were transported outside of the prevailing field of views of the cameras by infrequent, large eddies or sudden thermal updrafts. This led to an underestimation of the meandering with decreasing sub-ensemble size. In cross wind direction, the meandering calculated based on the >45 s sub ensemble underestimates the meandering during the first 30s by circa 20%. It can be assumed that the meandering was at least similarly underestimated for times larger than 45s. During the first 30s, the trajectory distribution was stronger spread in the positive cross wind direction filling the 3σ environment while the distribution was more compact in the negative direction. After 40s, the trajectories were skewed towards the negative direction. In the vertical, the meandering was 30% weaker than in the cross wind direction but the underestimation of the meandering was more prominent. Many puffs followed a downwards path while only few were caught in a strong updraft. The downwards puffs tended to be lost earliest leading to an underestimation of up to 50% during the first 30s when the trajectories shorter than 45s were ignored. In conclusion, the meandering could be measured quantitatively as long as the trajectories of all puffs within one ensembles were used but could be considered only as lower bound for sub ensembles.

7.2.3 Absolute dispersion

The absolute dispersion describes the mean square displacement of particles from the release point and can be calculated as the sum of relative dispersion and meandering (see Eq. 2.17). Figure 7.7 shows the relative dispersion and the centre of mass meandering of the vertical component and the resulting absolute dispersion for the two longest intervals

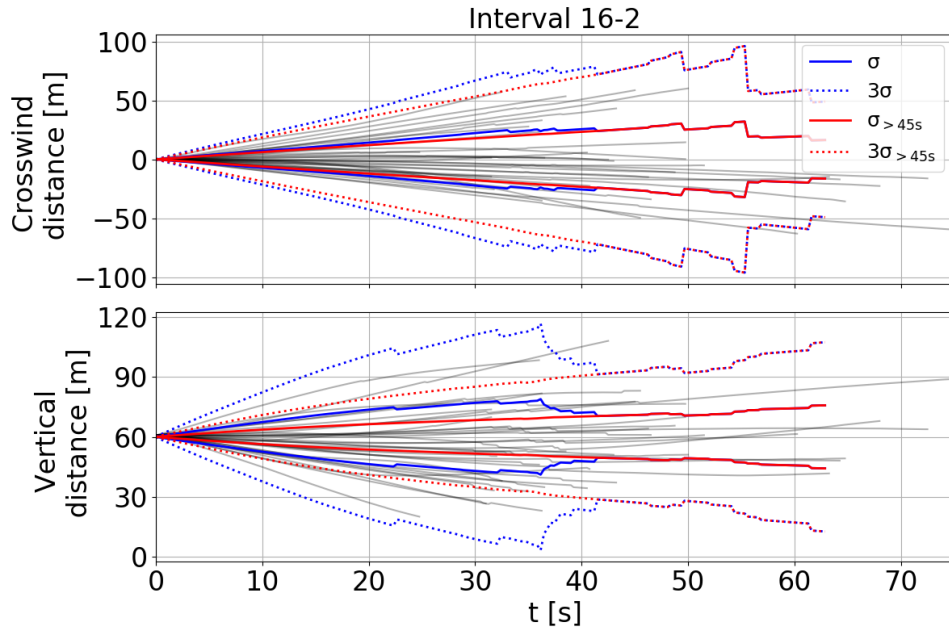


Fig. (7.6) Centre of mass meandering σ of the trajectory distribution for interval 16-2. The 3σ meandering is the envelope of the single trajectories (grey). The meandering was only representative of the flow as long as all puff trajectories within the interval were considered. The shortest trajectory was 25 s long. Subsampling of only longer (>45 s) trajectories (red) led to a systematic bias towards trajectories due to smaller eddies causing an underestimation of the meandering.

(15-1 and 16-2). The meandering was estimated accurately only for 35 s for 15-1 and for 25 s for 16-2. Therefore, the meandering limited the time series of the absolute dispersion. During the entire observation duration the absolute dispersion was dominated by the centre of mass meandering which was one order of magnitude larger than the relative dispersion. This confirms that the puff sizes were small.

In theory, the measured absolute dispersion can be used to estimate the Lagrangian integral time scale T^L by fitting Taylor's theorem (Eq. 2.19) to the curve. However, the expected range of T^L is in the same order of magnitude as the length of the time series. In the approximation of small times after release ($t \ll T^L$), the absolute dispersion becomes even independent of the Lagrangian time scale and the fit would be under determined (Eq. 2.21). In Fig. 7.7, the approximation for small times as well as the full equation were fitted to the measured absolute dispersion. Additionally, Eq. 2.21 based on the Eulerian velocity variance (Table 7.1) is plotted for comparison. Taylor's theorem considers particles from a point source. To account for the finite source, Eq. 2.19 and Eq. 2.21 were extended by an initial source size taken from the measured absolute dispersion at 1 s after release. The Lagrangian time scale estimated by the fit was 70 ± 10 s for 15-1 and 16.1 ± 0.1 s for interval 16-2. However, the total fitted time series were short with 35 s for 15-1 and 25 s for 16-2 and it can be assumed that the fit over-optimised the data. In fact, the Lagrangian time scales varied by more than 50% when the fit window was decreased by few seconds. Further, both fits optimised the variance of the vertical velocity as fit parameter. For interval 16-2, the quadratic fit resulted in $\sigma_w = 0.50 \text{ m}^2 \text{ s}^{-2}$, the fit of Taylor's theorem $\sigma_w = 0.81 \text{ m}^2 \text{ s}^{-2}$ with negligible small fit error compared to the

value estimated from the EC measurements $\sigma_w = 0.27 \text{ m}^2 \text{ s}^{-2}$ and the trajectories $\sigma_w = 0.65 \text{ m}^2 \text{ s}^{-2}$. Both fitted curves described the absolute dispersion relatively well, while the absolute dispersion for short times estimated from the Eulerian velocity variance underestimated the absolute dispersion for both intervals. Therefore, it can be assumed that the Eulerian variance did not represent the Lagrangian variance.

In conclusion, a longer time series of the absolute dispersion, and particularly of the meandering, is indispensable to estimate T^L reliably. However, it could be shown that, the Lagrangian time scale can in principle be estimated from the absolute dispersion of puff ensembles. This independent estimate could be compared to the Lagrangian time scales obtained from the autocorrelations (see section 7.3) to assess the validity of Taylor's theorem. Additionally, the relationship of Lagrangian and Eulerian time scales could be analysed analogously to section 7.3.

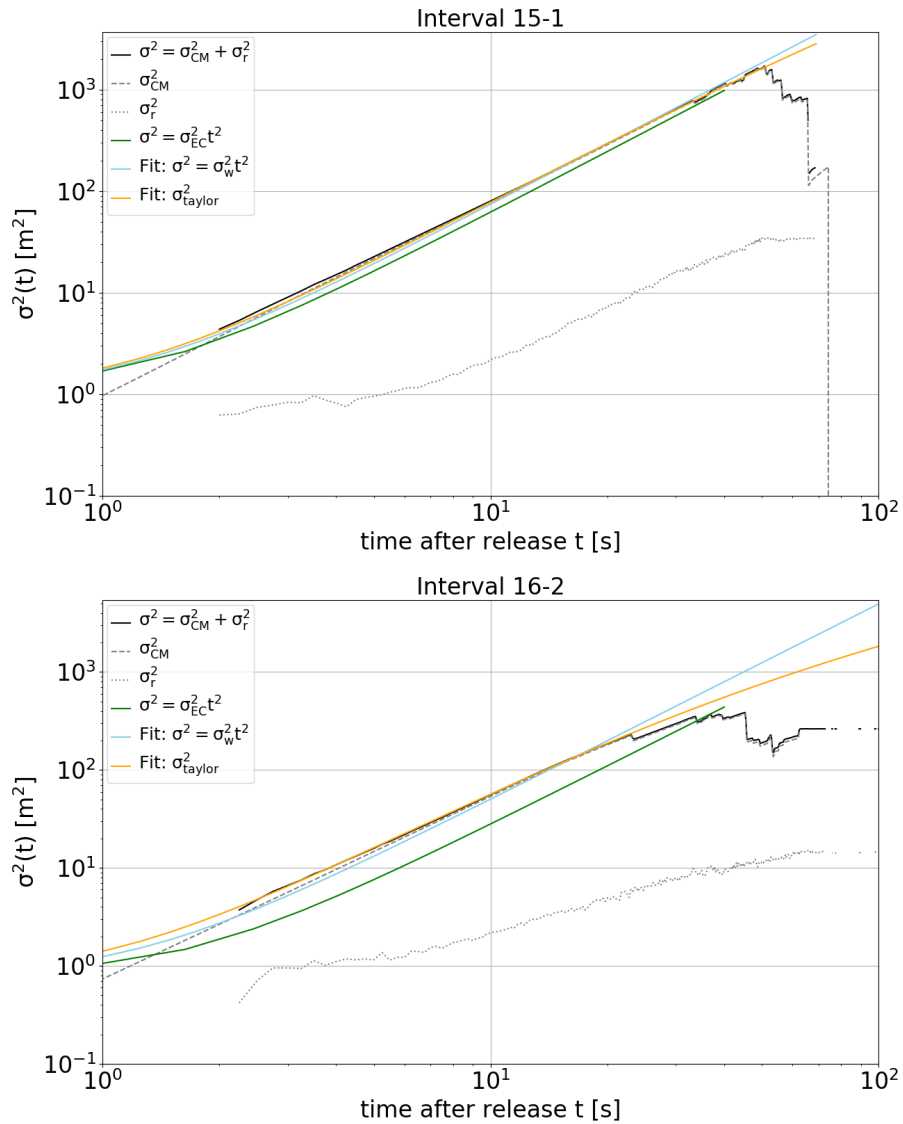


Fig. (7.7) Absolute dispersion for the vertical component for the two longest intervals 15-1 (upper panel) and 16-2 (lower panel). Taylor's description of the absolute dispersion in homogeneous turbulence was fitted to the curve in its complete form (Eq. 2.19) and for the approximation $t \ll T_L$ (Eq. 2.21).

7.3 Velocity correlations

The eddy covariance data and the centre of mass trajectories allow for the calculation of the Eulerian and Lagrangian velocity autocorrelations and thus studies on the relationship between the two frameworks. The motivation is to estimate the constant C of the linear stretching of time (Eq. 2.16) from atmospheric data and compare it with previous atmospheric and numeric studies (Table 2.1). Long and large ensembles are necessary. Thus only the intervals from 2018 were considered for the following analysis.

The estimation of the Eulerian and Lagrangian time scales rely on the stochastic approximation of $R^E(\tau)$ and $R^L(\tau)$ as exponential decays [Csanady, 1973]. This approximation has the advantage that the time scales can be determined as time when $R^L(\tau)$ falls to $1/e \approx 0.37$ [e.g. Hanna, 1981; Anfossi et al., 2006] and therefore requires comparably short time series. However, the shape of $R^L(\tau)$ in the atmospheric boundary layer, especially the convective boundary layer, might differ significantly from this picture and even show oscillations around zero [Deardorff and Willis, 1985].

7.3.1 Eulerian integral time scales

The Eulerian autocorrelations functions of the velocity components were calculated according to Eq. 2.12 from the EC velocities at 60 m for the four intervals in 2018 defined in Table 7.1. The Eulerian time scales T^E are given in Table 7.4. To give an uncertainty, T^E was also estimated using an exponential fit. The difference of the two values was used as error estimate in Table 7.6. The analysis of the Eulerian eddy covariance data set was performed by H. Ardeshiri.

Table (7.4) Eulerian time scales

Interval	T_u^E [s]	T_v^E [s]	T_w^E [s]
15-1	58.9±6.3	48.6±8.4	22.5±3
16-1	19.6±5.2	15.6±2.3	16.0±1.5
16-2	34.5±8.7	69.0±3.0	9.2±0.1
16-3	30.0±0.2	183.1±70.7	16.2±6.2

7.3.2 Lagrangian integral time scales

The Lagrangian integral time scales were estimated from the CM velocities of the puffs. The trajectories of each ensemble (as defined in Table 7.2) were rotated to the coordinate system of the mean wind. This coordinate system was defined based on the Eulerian wind velocity and direction from the eddy covariance measurements close to the source, but could, in principle, be based on the beginning of the Lagrangian trajectories as the Eulerian and Lagrangian mean velocities at the same spot are equal [Yeung, 2002]. The Eulerian measurements were chosen, as they sample the velocity components continuously with high accuracy while the trajectory ensembles gave only one value each 2 minutes. Hence, the eddy covariance measurements represent the mean flow at the release better. After rotation, the components of the centre of mass velocity were calculated (see section 6.2.5).

Assumption: Centre of mass behaves as a particle

The velocity of a particle within a puff can be separated into a velocity component relative to the puff's centre of mass u_i^r and the velocity of the centre of mass u_i^{cm} :

$$u_i = u_i^{cm} + u_i^r. \quad (7.3)$$

The Lagrangian autocorrelation function describes the correlations of all particles inside each puff but can be expressed as the sum of the contributions from relative and centre mass velocities [e.g. Mikkelsen et al., 1987]

$$R^L(\tau) = R^{L,cm}(t, \tau) + R^{L,r}(t, \tau) \quad (7.4)$$

While the total autocorrelation function considering ensembles of single particles is independent of time in homogeneous, isotropic turbulence, the proportionate importance of the centre of mass and relative velocity changes with time. Due to the puff growth, larger and more energetic eddies will contribute to the relative dispersion and its contributions grows.

From the COMTESSA data set, the velocities of single SO₂ molecules cannot be reconstructed. In consequence, only the autocorrelation of the CM velocity can be estimated from the CM trajectories. The centre of mass motion is mainly affected by the large eddies while the relative motion around the centre of mass is representative of the small eddies. The size of the puffs ($1-\sigma$) did not exceed 10 m during the course of observations (compare relative dispersion, Fig. 7.5) and can therefore be considered small compared to the scales of the large eddies. Therefore, it is assumed that the integral characteristic of the correlation function of a puff is similar to that of a single particle correlation function,

$$R^L(\tau) = R^{L,cm}(t, \tau) + R^{L,r}(t, \tau) \approx R^{L,cm}(\tau) \quad (7.5)$$

It is clear that by using this approximation, smaller-scale velocity fluctuations will be filtered away. However, e.g. Hanna [1981] pointed out that the Lagrangian time scale corresponds to the scale of the peak of energy spectrum and is as such only little affected by small scales.

Further it is assumed that the size of the puffs did not change significantly compared to the most energetic structures. In that case, the neglected relative contribution of the smaller-scale fluctuations is constant. The centre of mass velocity autocorrelation function can then be considered independent of the time t after release (in stationary turbulence).

Lagrangian velocity fluctuations

According to these assumptions, each puff was considered as a single particle whose velocity was described as propagating with the centre of mass velocity of the SO₂ distribution. The velocity fluctuations can be calculated relative to the Eulerian mean velocity [e.g. Mito and Hanratty, 2002; Luo et al., 2007, 2010] or the mean velocity of the trajectories [e.g. Wang et al., 1995; Dosio et al., 2005]. Figure 7.8 shows the mean velocity and velocity variance based on the eddy covariance data and the trajectories for interval 16-2. The trend is comparable during all intervals. Due to the elongated release, the Lagrangian velocity represented the velocity field after circa 4s. The Eulerian and Lagrangian mean velocities were similar in the along wind and cross wind component shortly after the release for all intervals. However, the Lagrangian mean along wind velocity continued to

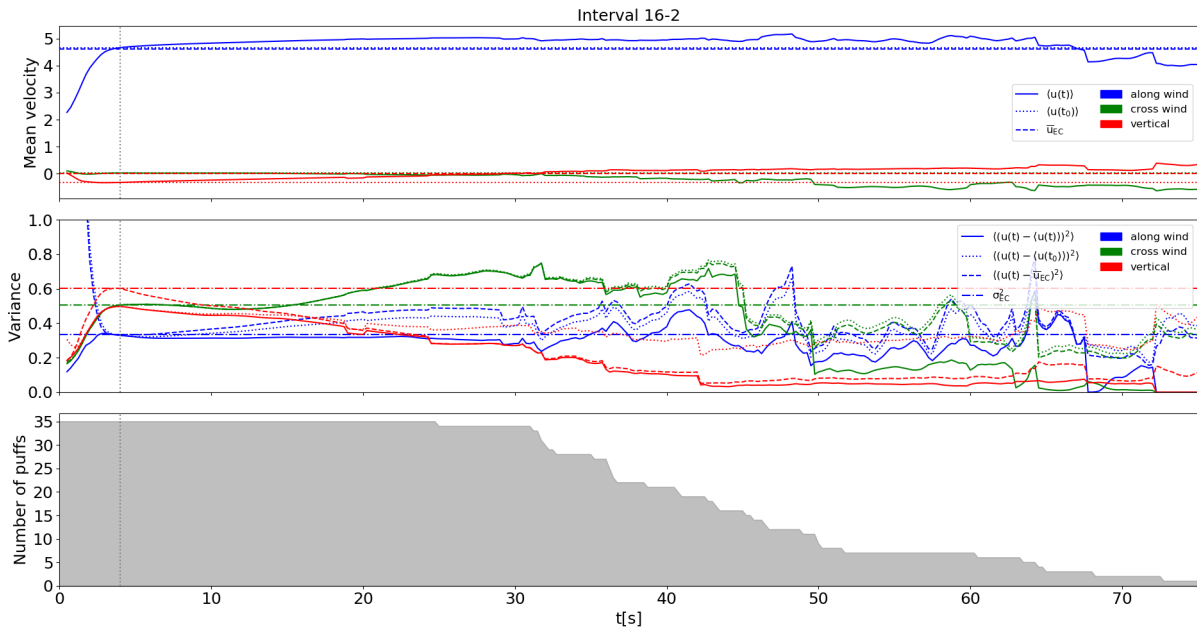


Fig. (7.8) Mean wind velocity calculated based on the Eulerian eddy covariance (EC) measurements and the Lagrangian trajectories (upper panel). The variances of the trajectories' velocity components were calculated with respect to the Eulerian and Lagrangian mean velocity (mid panel). The number of puff trajectories included in the ensemble decreased with time after release (lowest panel).

increase slightly (up to 5%) with time after release for all intervals. In the vertical component, the average trajectory dropped in the beginning ($> -0.5 \text{ m s}^{-1}$) and rose upwards after 10-30 s. This is consistent with a positive skewness of the velocity distribution typical for the lower convective boundary layer. However, SO_2 is heavier than air and in spite of the dilution, a small heavy gas dispersion effects cannot completely be excluded. The Lagrangian mean velocity was strongly affected by the trajectory ensemble: when a trajectory ends, small discontinuities could be observed in the mean velocity and the general uncertainty increases.

The Eulerian velocity variance represented the variance of the velocity field but did not necessarily represent the variance of the CM velocities. The Eulerian and Lagrangian variances showed good agreement at 4 s after release in the along and cross wind component however differed up to $0.38 \text{ m}^2 \text{ s}^{-2}$ (interval 16-2) in the vertical. As long as all trajectories were included, the variances showed a smooth trend but showed strong variation when trajectories were dropped. With decreasing ensemble size, the variances decreased as extreme trajectories were lost first (see section 7.2.2).

The Lagrangian autocorrelation functions were calculated according to Eq. 2.13 based on the CM velocity fluctuations. Figure 7.9 shows the autocorrelation function for interval 15-1 calculated based on the velocity fluctuations defined with respect to different mean velocities: (1) The velocity fluctuations were defined with respect to the Eulerian mean velocity \bar{u}_{EC} and the variance was considered time-independent, (2) the velocity fluctuations were defined relative to the Lagrangian mean velocity at time $t_0=4\text{s}$ $\langle u(t_0) \rangle$ and the variance was considered time-independent and (3) the velocity fluctuations were defined with respect to the time-dependent Lagrangian mean velocity $\langle u(t) \rangle$ and the vari-

ances depended on the time. Definition (3) accounted for non homogeneous turbulence and was used by Wang et al. [1995] and Dosio et al. [2005]. The autocorrelation functions showed discrete jumps which coincided with the end of single puff trajectories linked to an abrupt change in velocity fluctuations and variance. The three definition showed the same trend, although definition (3) was systematically lower in this interval following the time-trend of the variance. The limited amount of puffs (11-35 puffs per interval) and

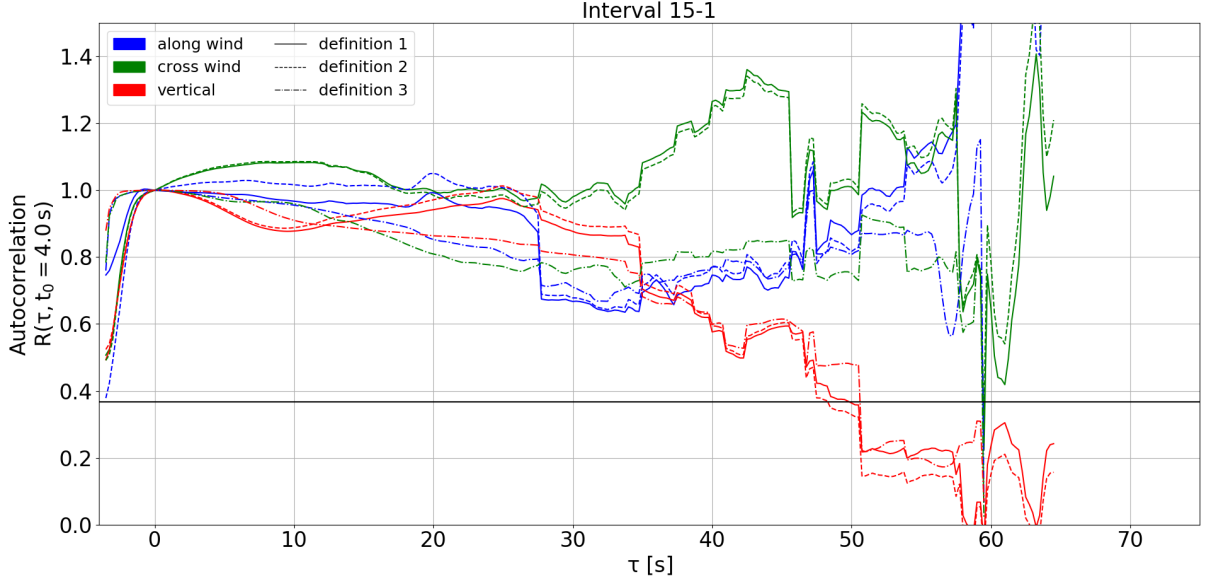


Fig. (7.9) Autocorrelation function for interval 15-1 based on three different definitions of the velocity fluctuations: (1) velocity fluctuations with respect to the Eulerian mean wind velocity and constant variance, (2) velocity fluctuations with respect to the Lagrangian mean wind velocity at $t_0=4$ s and constant variance, and (3) velocity fluctuations with respect to time dependent Lagrangian mean wind velocity. Definition (1) is used for the estimation of T^L and definition (3) corresponds to Wang et al. [1995] and Dosio et al. [2005].

particularly the variable trajectory length led to an under-representation and/or biases of the velocity distribution and therefore large uncertainties in the derived mean velocity and velocity variances (see also section 7.2.2 for discussion of biases in the trajectory distribution). Therefore, choosing time-dependent mean velocity and variances enhances the uncertainties when less trajectories were available and were therefore not suitable to normalise the autocorrelation function.

In the following, the autocorrelation functions were based on definition (1), for which the fluctuation $\tilde{u}_i(t) = u_i(t) - \bar{u}_{i,EC}$ were defined with respect to the Eulerian mean velocity $\bar{u}_{i,EC}$. The initial variance at time $t_0 = 4$ s was chosen as constant normalisation. The autocorrelation was calculated as following (solid line in Fig. 7.9)

$$R^L(\tau) = \frac{\langle \tilde{u}(t_0)\tilde{u}(t_0 + \tau) \rangle}{\langle \tilde{u}^2(t_0) \rangle} \quad (7.6)$$

and the time scale T^L was determined as first time when

$$R^L(\tau = T^L) = \frac{1}{e}. \quad (7.7)$$

Figure 7.10 shows the autocorrelation functions for the three components for the four intervals. For the vertical components, the drop to $1/e$ is clearly visible while for the along wind and cross wind components, the autocorrelations only dropped in few intervals during the observed times. For these components, it was only possible to state that the Lagrangian integral time scale was at least the total observation time but it could have been significantly higher. The estimated time scales are reported in Table 7.5. The uncertainties in Table 7.6 were estimated from the autocorrelation based on sub ensembles (see below).

Dependency on trajectory ensemble

The Lagrangian time scales were smaller than the length of the shortest trajectory in each interval. This means that the Lagrangian time scales have been estimated based on a sub ensemble of the trajectories. The puff trajectories following large eddies were tracked for the shortest times and were systematically sorted out. Large eddies led to a longer persistence of the centre of mass velocity and in consequence a higher time scale. Therefore, it can be assumed, that the time scales estimated from sub ensembles represent lower bounds for the Lagrangian time scale.

To analyse the effect of the sub ensembles, the calculation of the autocorrelation functions and Lagrangian time scales was repeated for sub ensembles where each sub ensemble contained only trajectories of a minimum length (Fig. 7.10). Following Eq. 7.6, the autocorrelations were normalised with the initial variance of the sub ensemble which was lower due to the systematic trajectory loss. Table 7.5 lists the variances and derived Lagrangian time scales for the sub ensembles. These recalculated variances were chosen rather than the variances based on all trajectory to access the uncertainty of choice of the sub ensemble. The variances decreased with decreasing number of trajectories agreeing with the assumption that the sub ensembles filtered the large eddies.

The uncertainties of the Lagrangian time scales were estimated from the shift of the $1/e$ drop of the sub ensembles. The shortest sub ensembles for which the estimated time scale was smaller than the minimum trajectory length was selected as reference, e.g. 60 s minimum trajectory length for interval 15-1. The difference was used as error estimate in Table 7.4. Intervals 16-1 and 16-3 did not contain enough long trajectories that a sub ensemble was found. The highest relative error of 32% estimated for interval 15-1 was used for these two intervals.

7.3.3 Relationship of Eulerian and Lagrangian time scales

The Eulerian and Lagrangian integral time scales were determined for several intervals during different states of the surface layer. The quantitative values are listed in Table 7.6.

The ratio $\beta = \frac{T^L}{T^E}$ is given with the standard deviation $\frac{\Delta\beta}{\beta} = \sqrt{\left(\frac{\Delta T^L}{T^L}\right)^2 + \left(\frac{\Delta T^E}{T^E}\right)^2}$, as well as the proposed constant $C = \beta i$ where i is the turbulence intensity. As discussed above, only the Lagrangian vertical autocorrelation dropped consistently below $1/e$. Therefore, it was only possible to estimate T^L for the vertical component. Furthermore, the value must be interpreted as a lower bound and the derived values for β and C represented lower bounds as well. The values for β ranged between 1.5 and 2.9, and C ranged between 0.20 and 0.58.

Figure 7.11 shows the vertical Lagrangian time scales compared to the Eulerian time

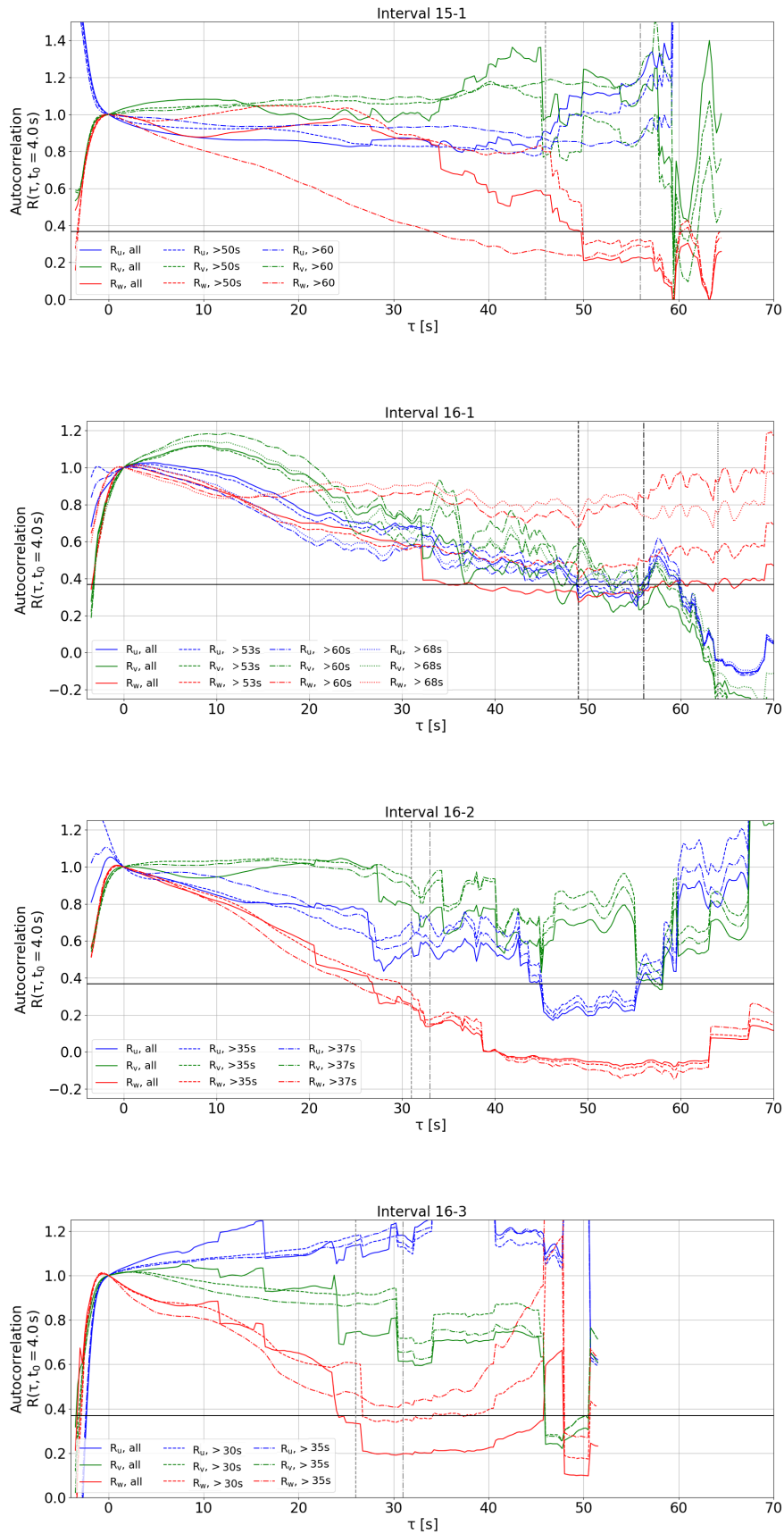


Fig. (7.10) Lagrangian autocorrelation functions for the four time intervals. For each interval, sub ensembles containing only puffs which were observed for a minimum duration (indicated by vertical lines) were selected. The included number of puffs is listed in Table 7.5.

Table (7.5) Lagrangian time scale for the vertical component based on sub ensembles

interval	min. trajectory length [s]	number of trajectories	$\langle \tilde{w}^2(t_0) \rangle$ [m ² s ⁻²]	T_w^L [s]
15-1	-	26	0.71	49.7
	50	17	0.50	50.0
	60	8	0.55	34.0
16-1	-	11	0.41	34.8
	53	10	0.28	-
	60	9	0.16	-
	68	7	0.20	-
16-2	-	35	0.65	26.8
	35	28	0.47	29.8
	37	24	0.32	24.7
16-3	-	20	0.66	24.2
	30	10	0.37	26.7
	35	9	0.24	-

Table (7.6) Eulerian and (lower bound) Lagrangian time scales for the vertical component

Interval	T^E [s]	T^L [s]	β	$C = \beta i$
15-1	22.5±3	50±16	2.2±0.7	0.50±0.15
16-1	16.0±1.5	35±11	2.2±0.7	0.58±0.19
16-2	9.2±0.1	27±3	2.9±0.3	0.33±0.04
16-3	16.2±6.2	24±8	1.5±0.8	0.20±0.10

scales for the four intervals. Figure 7.12 presents the relationship between the ratio of the time scales and the reciprocal turbulence intensity. These are the first experimental estimates in the ABL since the PHOENIX experiments by Hanna [1981] which reported considerable high errors of at least 50% for the Lagrangian times scales. For an eye guide, the experimental value of $C = \beta i = 0.7$ from Hanna [1981] and the value range of previous theoretical studies and simulations are reproduced (compare Table 2.1).

Assuming a linear relationship [Corrsin, 1963; Pasquill and Smith, 1983], the value of C was estimated by a weighted least square fit. Due to the fact, that T^L are lower bounds, the fit result $C = 0.33 \pm 0.01$ represents a lower bound as well. As such the measured value confirms the range ($C = 0.3 - 0.8$) of previous theoretical studies and simulations and previous measurements ($C = 0.7$). During all intervals, neutral to weakly unstable conditions were observed. A dependency of C on the stability has been proposed in the literature [e.g Hanna, 1981]. The widely cited value of $C = 0.7$ is based on the measurements of Hanna [1981] during convective conditions and at mostly larger turbulence intensity than observed during COMTESSA. He states that "[t]he theoretical formula $\beta = 0.4i$ preferred by others best fits the few points at high $1/i$ (high wind velocities), but underestimates the points at low $1/i$ ". This trend is also observed in the COMTESSA data: Considering single

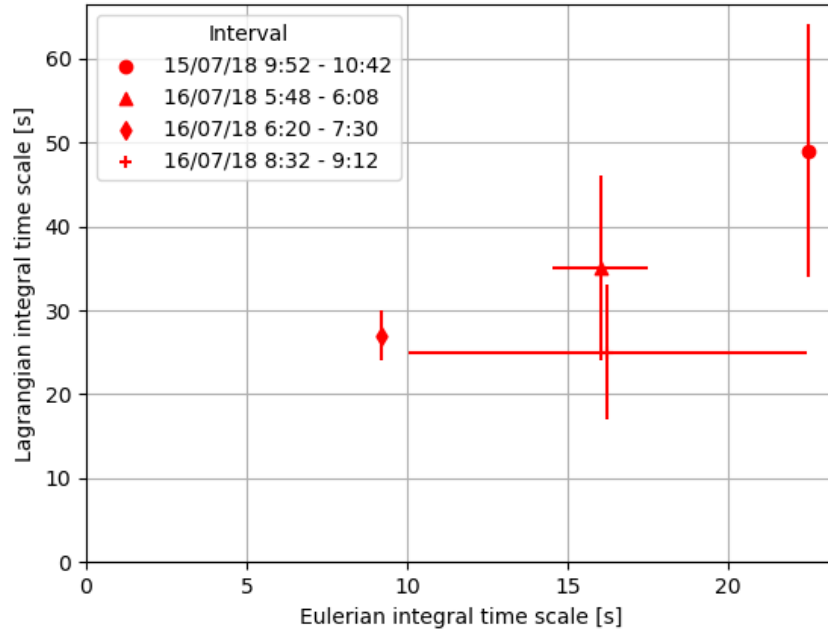


Fig. (7.11) Measured relationship of Eulerian and (lower-bound) Lagrangian time scales for the vertical component.

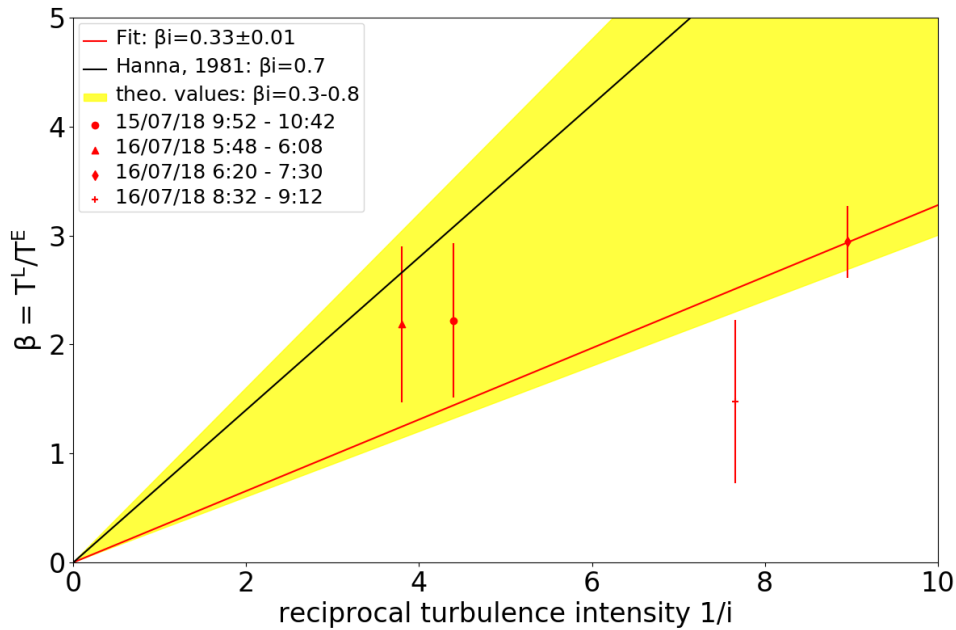


Fig. (7.12) The ratio of the time scales β versus the reciprocal turbulence intensity for the vertical component. The measured β are lower bound values. The predicted linear relationship between β and $1/i$ of Corrsin [1963] was fitted to the data. Proposed values based on experiments and theory are indicated.

intervals, C is higher for the intervals at high turbulent intensity and low wind velocities (15-1 and 16-1) compared to the intervals of higher wind velocities (16-2 and 16-3). Based

on LES, Anfossi et al. [2006] estimated that the proportionality is smaller ($C_w=0.40$ in the vertical) for neutral conditions than for strongly convective conditions ($C_w=0.54$ in the vertical). Further, Dosio et al. [2005] found that $C=0.7$ fitted the overall results from a LES of the convective boundary layer, but data during high wind velocities (high $1/i$) were better represented by $C=0.40$. Considering the wide range of estimates, the new experimentally estimated lower value of $C = 0.33 \pm 0.01$ agrees with previous measurements and theoretical studies. This measurement confirms satisfactorily the hypothesis of Hay and Pasquill [1959] and further supports the parametrisations of C generally used.

Chapter 8

Conclusions

This thesis presented the three COMTESSA artificial SO₂ release campaigns and the analysis of the turbulent dispersion of SO₂ puffs. During the summers in 2017-2019, SO₂ puffs were released and simultaneously recorded from up to six UV SO₂ cameras. The meteorological parameters (wind velocity, heat, moisture and CO₂ fluxes) were recorded by state-of-the-art eddy covariance systems. The COMTESSA artificial release experiments provide a novel data set of high-resolution (both temporal and spatial) column-integrated tracer concentration. The turbulent flow, in which the turbulent dispersion of the released SO₂ was observed, was characterised by the eddy covariance measurements. Hence, the COMTESSA data set consists of novel data of projected three-dimensional tracer dispersion in high-resolution (few Hertz and up to few centimetres) while the background flow was fully characterised. This data set will be made publicly available after the end of the project in 2020. The experiments required great effort and are not easily repeated. The experimental setup (both the release and the cameras setup) were optimised by the COMTESSA team and the experience documented here will be beneficial for future study design. A detailed discussion of the experimental setup was given in section 5.3.

This thesis focused on the analysis of the dispersion of 98 puffs observed within five time intervals on different days and under different conditions of the ABL (neutral to weakly unstable). The 3D trajectories of the centre of mass motion of the puffs were reconstructed based on the tomographic setup of the SO₂ cameras. Using the obtained distance, the image coordinates were scaled to represent the images of the puffs in metres. It was demonstrated that the scaled images can be used to obtain the relative dispersion and that the 3D trajectories can be used to obtain the meandering. Combined, the absolute dispersion of the SO₂ puffs was estimated.

The relative dispersion of the puffs in each of the five analysed intervals showed the t^2 -scaling of the source regime according to [Batchelor, 1952]. This allowed for the estimate of the source time scales of up to 24 s for the observed intervals. The source time scale was higher than intended due to the unintended elongation of the puffs during release. The extended source regime had as consequence that the onset of the Richardson-Obukhov scaling of the inertial subrange was shifted to a larger time after release. At the same time, the observation time of the puffs was limited to 25-100 s by the camera setup and the topography (see also section 5.3). Therefore, the Richardson-Obukhov scaling could not be observed in the presented data. However, the novel approach demonstrated that the Richardson-Obukhov scaling can be observed from SO₂ camera data if either the source time scale is smaller (e.g. by releasing smaller puffs) or longer time series can be obtained. Then, the Richardson-Obukhov constant, an important model parameter,

could be estimated from the measured relative dispersion. Further, the time series of the meandering was limited by the length of the shortest trajectory. This limited the absolute dispersion to circa 30 s. For short times, the absolute dispersion is independent of the Lagrangian time scale (Eq. 2.19 and 2.21), which should be estimated. Similarly, an estimation of the Lagrangian time scale was not possible from the measured absolute dispersion but it could be demonstrated that the method is suitable to measure the Lagrangian time scale if a longer time series is provided.

In the second part of the analysis, both the Lagrangian and the Eulerian time scales were estimated from the 3D CM trajectories (Lagrangian) and from the eddy covariance measurements (Eulerian). The Lagrangian time scales for four ensembles for the vertical component were estimated from the CM velocity autocorrelations. The obtained time scales were smaller than the length of the shortest trajectory. The shortest trajectories were associated with transport by large eddies for which the CM velocity is more persistent than compared to smaller eddies. Therefore, the obtained values for the Lagrangian time scales were interpreted as lower bounds. Combining the Eulerian and Lagrangian time scales, the linear relation between the ratio of the time scales $\beta = \frac{T^L}{T^E}$ and the reciprocal turbulence intensity i was revised. The linear relation $\beta = 0.33 \cdot \frac{1}{i}$ was estimated where $C=0.33\pm 0.01$ is the lower bound for the proportionality constant. This value is the first experimental estimate of C in the ABL since the early measurements by Hanna [1981] ($C=0.7$) which were connected to high uncertainties of 50%. As a lower bound, the new value confirms the range of theoretical studies and studies based on LES and DNS.

Future work

In the future, the analyses presented here will be extended to the data obtained during the 2019 release campaign. Due to the higher release amount and the partially greater distances, the puffs were observed for a longer time leading to longer time series of the relative dispersion and meandering. Further, the source distribution was smaller and isotropic. Hence, a smaller time scale can be expected. These aspects combined let us expect that the Richardson-Obukhov scaling can be observed in the time series of the relative dispersion. However, the release frequency of the larger puffs was smaller and less puffs are available for the statistics.

Apart from the presented analysis, the tomographic setup allows, in principle, also for a complete tomographic reconstruction of the SO₂ concentration distribution within the plumes and puffs. Then, the higher moments of the concentration distribution can be inferred which has never been done. The higher moments control whether the local concentrations for instance exceed toxicity or flammability thresholds.

Further, the data set will be made publicly available. This will allow the data to be used as validation set for simulations or new models. For example, the 3D data can be compared to state-of-the-art LES.

Besides the turbulent dispersion, the COMTESSA data set provides also chances to assess SO₂ camera applications. For instance, for calculating the SO₂ emission rates, the velocity of the plume needs to be known. The velocity is often inferred directly from the images using cross-correlation or optical flow methods. The quality of these algorithms has been discussed using experimental and simulated data [e.g. Peters et al., 2015; Gliß et al., 2018]. The COMTESSA data set contains simultaneously measured wind velocities at high frequencies and resolution. Further, the knowledge of the release amount allows to assess the uncertainties of a typical SO₂ flux retrieval from SO₂ cameras. The

simultaneous measurements from different viewing directions and distances to the plumes allow to study radiative transfer effects under clear-sky and cloudy conditions. Also, the proposed correction of the projection of the plume direction [Klein et al., 2017] could be evaluated using the plume data. However, the data here contains almost no aerosol in contrast to typical environments (volcanoes, power plants,...) and results might represent a best case scenario only.

Appendix

Appendix A

Details on measurements and data analysis

A.1 Details on pose reconstruction

The azimuth and elevation angles of the cameras' optical centre, ($i_c=696$, $j_c=520$), were estimated based on image features for which the position was known. The azimuth angle of an arbitrary pixel column i is given as

$$\alpha_i = \alpha_{i_c} + \tan^{-1} \left(\frac{(i - i_c) \cdot s_p}{f} \right) \quad (\text{A.1})$$

where α_{i_c} is the azimuth angle of the optical centre, f is the focal length and $s_p=4.65 \mu\text{m}$ is the size of one pixel on the sensor. Macroscopically, the angle between the camera at position $(x_{cam}, y_{cam}, z_{cam})$ and a feature at position $(x_{feat}, y_{feat}, z_{feat})$ is given by

$$\alpha = \tan^{-1} \left(\frac{x_{feat} - x_{cam}}{y_{feat} - y_{cam}} \right) \quad (\text{A.2})$$

Given the pixel coordinate (i_{feat}, j_{feat}) of a image feature, e.g. the tower top, the above equations are combined to calculate the azimuth angle of the camera as

$$\alpha_{i_c} = \tan^{-1} \left(\frac{x_{feat} - x_{cam}}{y_{feat} - y_{cam}} \right) - \tan^{-1} \left(\frac{(i_{feat} - i_c) \cdot s_p}{f} \right) \quad (\text{A.3})$$

The elevation angle is calculated analogously considering the image row j and the total distance $d = \sqrt{(x_{feat} - x_{cam})^2 + (y_{feat} - y_{cam})^2}$.

A.2 Analysis of eddy covariance time series

The following section is adapted from Dinger et al. [2018].

Before the actual post processing, the collected data was treated by the LICOR EddyPro software system for despiking [e.g. Vickers and Mahrt, 1997; Mauder, 2013] and for applying the triple rotation correction [Wilczak et al., 2001] that nullify the average vertical and across-wind components, and the $\overline{v'w'}$ Reynolds stress component. This means that the coordinate system is aligned with the measured mean wind direction. See also Burba [2013] for a description of the corrections applied in EddyPro. The values for the mean

wind and the three turbulent fluxes are reported at the highest respective level close to the source location. The energy spectrum of a velocity component is the Fourier transform of the autocorrelation function of that velocity component and was calculated according to e.g. Stull [1988, p.312] and using Taylor's hypothesis. The mean dissipation of turbulent kinetic energy was obtained by fitting a Kolmogorov spectrum (Eq. 2.11) to the inertial range of the measured spectrum using the method discussed in detail by Stull [1988]. The value of the Kolmogorov constant $C_k=0.49$ was taken according to measurements and theory of homogeneous isotropic turbulence [e.g Stull, 1988; Pope, 2000]. The surface layer is further characterised by estimating the friction velocity u_* from the Reynolds stress component at two meters as $u_*^2 = |\overline{u'w'}|$. The Obukhov length is calculated according to Eq. 2.7 with the sonic temperature as an approximation of virtual temperature as discussed in e.g. Kaimal and Finnigan [1994].

A.3 Optical camera calibration and distortion

Generally, a 3D scene is projected to an image plane by applying the extrinsic and intrinsic camera matrix to a point. For distortion-free pinhole cameras, this projection can be described as

$$s \cdot (i, j, 1) = K \cdot E(x, y, z, 1) \quad (\text{A.4})$$

where K is the intrinsic camera matrix describing the physical properties (focal length, aspect ratio and optical centre) and E is the extrinsic matrix depending on relative position and pose of the camera and scene. If the optical configuration is not changed, K is specific to the camera and can be reused. Typically, the radial and tangential distortion is described by a set of distortion coefficients k_n and p_n . The Brown-Conrady model [Brown, 1966] can be used to correct for the distortion of the pixel coordinates according to

$$i_{undistorted} = i(1 + k_1r^2 + k_2r^4 + k_3r^6 + \dots) + p_1(r^2 + 2i^2) + 2p_2ij \quad (\text{A.5})$$

$$j_{undistorted} = j(1 + k_1r^2 + k_2r^4 + k_3r^6 + \dots) + 2p_1ij + p_2(r^2 + 2j^2) \quad (\text{A.6})$$

where r is the pixel distance to the centre pixel.

The intrinsic camera matrix and the distortion coefficients of the individual cameras were measured following the method introduced by Zhang [2000]. This process is known as camera calibration in computer vision applications. Images of a checker board were recorded from different angles and distances for all 12 UV cameras. Camera calibrations were performed shortly after the 2018 and 2019 campaign with the same camera configuration (same lens combinations and unchanged aperture etc). For the distortion pattern, a 9×6 checker board was printed in size Din-A0 and attached to a flat 2 mm aluminium plate (Fig. A.1). The SO_2 cameras are optimized for backscattered sunlight in the UV region. The reflectivity of the pattern in the UV, however, is rather low leading to a low signal-to-noise ratio (SNR). Therefore a comparably high amount of different orientations were recorded (ca. 100 per camera compared to generally recommended 20 scenes). In 2018, all images were recorded with 250 ms exposure time but the images within 10 s were averaged to increase the SNR. In 2019, 10 images recorded at 500 ms exposure times were recorded per scene. The apertures of the off-band cameras (330 nm) were closed to record at the same frame rate as the on-band cameras (310 nm) for which the incoming radiation is weaker. The closed apertures led to a larger depth of field and therefore sharper images over a larger range of distances. The camera calibration was therefore more precise for the off-band cameras.

After recording the images, the camera calibration was performed using the Open Source Computer Vision Library (OpenCV). The readily available functions detected the corners of the distortion pattern and calculated a camera model which mapped the detected corners to the equally spaced checker board. The functions estimated the intrinsic camera matrix and distortion coefficients. From these, macroscopic parameters such as focal length and aspect ratio were calculated. The numerical values of the calibrations are summarised in tables A.1 and A.2. The cameras had similar radial distortion and negligible tangential distortion.



Fig. (A.1) Distortion pattern and UV camera image

Table (A.1) Camera calibration from 21/08/2018

Camera	focal length [mm]	centre pixel		distortion coefficients				
		i_c	j_c	k_1	k_2	p_1	p_2	k_3
UV1 310	12.62	678.4	629.8	-0.323	-0.038	-4.7e-4	6.8e-4	0
UV3 310	12.53	688.6	634.5	-0.279	-0.337	-6.1e-4	1.2-3	0
UV4 310	12.76	709.4	606.3	-0.291	-0.227	2.3e-3	-1.3e-2	0
UV5 310	12.64	690.2	640.5	-0.314	-0.069	1.5e-3	3.0e-4	0
UV6 310	12.71	646.5	613.8	-0.344	-0.007	-5.0e-4	10.4e-4	0

Table (A.2) Camera calibration from 26-27/08/2019

Camera	focal length [mm]	centre pixel		distortion coefficients				
		i_c	j_c	k_1	k_2	p_1	p_2	k_3
UV1 310	12.75	710.9	587.7	-0.322	0.633	9.2e-5	9.1e-4	0
UV2 310	12.77	712.8	528.3	-0.346	0.404	3.5e-4	9.6e-5	0
UV3 310	12.73	718.3	527.8	-0.344	0.263	1.7e-3	7.6e-4	0
UV4 310	12.73	700.7	551.6	-0.314	-0.003	-3.4e-3	-7.4e-4	0
UV5 310	12.83	708.2	564.3	-0.332	0.247	-1.0e-4	-3.2e-4	0
UV6 310	12.87	697.1	548.3	-0.322	0.102	4.1e-4	-1.5e-3	0
UV1 330	12.89	716.7	567.3	-0.337	0.751	-1.8e-3	3.9e-4	0
UV2 330	12.87	729.7	545.7	-0.366	0.750	-1.6e-3	6.2e-4	0
UV3 330	12.86	737.6	504.6	-0.375	0.668	-2.1e-3	1.4e-3	0
UV4 330	12.85	705.6	603.1	-0.356	0.375	-7.1e-4	5.6e-4	0
UV5 330	12.87	724.6	535.4	-0.353	0.853	-1.6e-3	5.4e-4	0
UV6 330	13.01	771.9	597.9	-0.333	0.387	-2.2e-3	7.1e-4	0

List of Abbreviations

ABL	atmospheric boundary layer
CCD	charged-couple device
CM	centre of mass
COMTESSA	Camera Observation and Modelling of 4D Tracer Dispersion in the Atmosphere
CO ₂	chemical formula for carbon dioxide
DOAS	differential optical absorption spectroscopy
DNS	direct numerical simulations
EC	eddy covariance
FOV	field of view
IR	infrared
LES	large eddy simulations
Lidar	light detection and ranging
NILU	Norsk institutt for luftforskning / Norwegian Institute for Air Research
ROI	region of interest
SCD	slant column density
SNR	signal to noise ratio
SO ₂	chemical formula for sulfur dioxide
STD	standard deviation
UTC	Coordinated universal time
UV	ultraviolet

List of Figures

1.1	Drawing of turbulence in water	1
1.2	Overview of data analysis	4
2.1	Diurnal cycle of the atmospheric boundary layer	8
2.2	Energy cascade according to Kolmogorov's theory	11
2.3	Lagrangian and Eulerian frameworks	12
2.4	Autocorrelation function in the Lagrangian and Eulerian framework	13
2.5	Sketch of absolute dispersion, relative dispersion and meandering	16
2.6	Overview of different study design for atmospheric dispersion experiments .	18
3.1	Measurement principle of atmospheric optical absorption spectroscopy . . .	22
3.2	Typical measurement geometry of a SO ₂ camera	24
3.3	Typical image of volcanic SO ₂ emission from a SO ₂ camera	24
3.4	Measurement principle of the two-filter SO ₂ camera	25
3.5	Image of a COMTESSA SO ₂ camera	29
3.6	Internal view of COMTESSA cameras	31
3.7	Filter transmittance curves	32
4.1	Experimental site	33
4.2	Image of COMTESSA SO ₂ camera during the 2017 campaign	35
4.3	Overview map of the camera positions used during all three campaigns . .	36
4.4	Sketch of release tower with positions of sonic anemometers and release pipe and image-inlets of the release	39
4.5	Pictures of the gas bottle setup during the three campaigns	40
5.1	Mean and standard deviation in arbitrary image areas after background correction	49
5.2	SO ₂ calibration using gas cells for all cameras on the 16 July 2018	51
5.3	Continuous release on 20 July 2017 7:20: Snapshot of SO ₂ camera images .	54
5.4	Continuous release on 20 July 2017 8:40: Sequence of SO ₂ camera images .	54
5.5	Continuous release on 16 July 2018 5:44: Snapshot of SO ₂ camera images .	55
5.6	Puff releases on 20 July 2017 10:30: Snapshot of SO ₂ camera images	56
5.7	Puff releases on 20 July 2017 10:30: Sequence of SO ₂ camera images	56
5.8	Puff release on 16 July 2018 09:21: Snapshot of SO ₂ camera images.	57
5.9	Puff releases on 27 July 2019 14:43: Snapshot of SO ₂ camera images	58
5.10	Puff release 25 on 16 July 2018 6:35: Sequence of SO ₂ camera images of a single puff	59
5.11	Puff release 23 on 27 July 2019 14:43: Sequence of SO ₂ camera images of a single puff	60

6.1	Sketch of the field of view of two cameras from above	64
6.2	Puff detection based on noise-reduced images	66
6.3	Flow diagram of the puff detection algorithm	66
6.4	Total signal in the region of interest for puff 25 on 16 July 2018	68
6.5	Detected centre of mass trajectories of six puffs on 16 July 2018	70
6.6	Reconstructed 3D trajectories of six puffs on 16 July 2018	71
6.7	Duration and length of all reconstructed 3D trajectories on 16 July 2018	72
6.8	Puff mass in the region of interest for puff 25 on 16 July 2018	72
6.9	Maximum observed optical density for six puffs on 16 July 2018	73
6.10	Puff spread in the region of interest for puff 25 on 16 July 2018	74
6.11	Mean flow direction and velocity reconstructed from the puff trajectories and from the eddy covariance data	76
6.12	Centre of mass velocity components for six puffs on 16 July 2018	77
7.1	Overview of meteorological parameters on 15 and 16 July 2018	80
7.2	Map of centre of mass trajectories in 2017	82
7.3	Map of centre of mass trajectories in 2018	83
7.4	Relative dispersion for interval 20-1	85
7.5	Relative dispersion for the ensemble average	86
7.6	Centre of mass meandering for interval 16-2	89
7.7	Absolute dispersion in the vertical component	90
7.8	Mean wind velocity for interval 16-2	93
7.9	Autocorrelation function for interval 15-1 based on three different defini- tions of the velocity fluctuations	94
7.10	Lagrangian autocorrelation functions for the four time intervals	96
7.11	Measured relationship of Eulerian and (lower-bound) Lagrangian time scales for the vertical component.	98
7.12	β versus the reciprocal turbulence intensity	98
A.1	Distortion pattern and UV camera image	109

List of Tables

2.1	Overview of previous studies on the Eulerian-Lagrangian transformation . . .	15
3.1	COMTESSA SO ₂ camera specifications	30
4.1	EC measurement level heights at the release tower	34
4.2	Resolution and FOV of the two lens types for various object distances . . .	36
4.3	Plume release experiments	41
4.4	Puff release experiments in 2017	42
4.5	Puff release experiments in 2018	43
4.6	Puff release experiments in 2019	44
5.1	Calibration gas cells as measured in 2018	50
5.2	Overview of the three field campaigns (average values)	53
7.1	Intervals of nearly-stationary conditions: EC measurements	81
7.2	Intervals of nearly-stationary conditions: Puff trajectories	82
7.3	Vertical source size and derived time scale	87
7.4	Eulerian time scales	91
7.5	Lagrangian time scale for the vertical component based on sub ensembles .	97
7.6	Eulerian and (lower bound) Lagrangian time scales for the vertical component	97
A.1	Camera calibration from 21/08/2018	109
A.2	Camera calibration from 26-27/08/2019	110

Personal bibliography

Parts of this thesis has been published in

Dinger, A. S., K. Stebel, M. Cassiani, H. Ardeshiri, C. Bernardo, A. Kylling, S.-Y. Park, I. Pisso, N. Schmidbauer, J. Wasseng, and A. Stohl (2018). Observation of turbulent dispersion of artificially released SO₂ puffs with UV cameras. *Atmos. Meas Tech.* (11), 6169-6188, doi:10.5194/amt-11-6169-2018.

Gliss, J., K. Stebel, A. Kylling, A. S. Dinger, H. Sihler, and A. Sudbø (2017). Pyplis - A Python Software Toolbox for the Analysis of SO₂ Camera Images for Emission Rate Retrievals from Point Sources. *Geosciences* 7(4), 134, doi:10.3390/geosciences7040134.

Other publications by the author

Butz, A., A. S. Dinger, N. Bobrowski, J. Kostinek, L. Fieber, C. Fischerkeller, G. B. Giuffrida, F. Hase, F. Klappenbach, J. Kuhn, P. Lübcke, L. Tirpitz, Q. Tu, (2017). Remote sensing of volcanic CO₂, HF, HCl, SO₂, and BrO in the downwind plume of Mt. Etna. *Atmos. Meas Tech.* (10), 1-14, doi:10.5194/amt-10-1-2017.

Bibliography

- Anfossi, D., U. Rizza, C. Mangia, G. A. Degrazia, and E. Pereira Marques Filho (2006). Estimation of the ratio between the Lagrangian and Eulerian time scales in an atmospheric boundary layer generated by large eddy simulation. *Atmos. Environ.* 40(2), 326–337.
- Angell, J. K. (1964). Measurements of lagrangian and eulerian properties of turbulence at a height of 2,500 ft. *Q. J. R. Meteorol. Soc.* 90(383), 57–71.
- Angell, J. K., D. H. Pack, W. H. Hoegker, and N. Delver (1971). Lagrangian-Eulerian time-scale ratios estimated from constant volume balloon flights past a tall tower. *Q. J. R. Meteorol. Soc.* 97(411), 87–92.
- Arya, S. P. (1999). *Air pollution meteorology and dispersion*. New York: Oxford University Press.
- Barad, M. L. (1958). Project Prairie Grass, a Field Program in Diffusion. *Geophys. Res. Pap.* 59.
- Batchelor, G. K. (1952, apr). Diffusion in a field of homogeneous turbulence: II. The relative motion of particles. *Math. Proc. Cambridge Philos. Soc.* 48(2), 345–362.
- Bianchi, S., L. Biferale, A. Celani, and M. Cencini (2016, jan). On the evolution of particle-puffs in turbulence. *Eur. J. Mech. - B/Fluids* 55, 324–329.
- Bluth, G. J. S., J. M. Shannon, I. M. Watson, A. J. Prata, and V. J. Realmuto (2007). Development of an ultra-violet digital camera for volcanic SO₂ imaging. *J. Volcanol. Geotherm. Res.* 161 (1-2), 47–56.
- Bobrowski, N., R. von Glasow, A. Aiuppa, S. Inguaggiato, I. Louban, O. W. Ibrahim, and U. Platt (2007). Reactive halogen chemistry in volcanic plumes. *J. Geophys. Res.* 112(D6), D06311.
- Brown, D. (1966). Decentering Distortion of Lenses. *Photom. Eng.* 32(3), 444–462.
- Burba, G. (2013). *Eddy Covariance Method for Scientific, Industrial, Agricultural, and Regulatory Applications: A Field Book on Measuring Ecosystem Gas Exchange and Areal Emission Rates*. Lincoln, NE, USA: LI-COR Biosciences.
- Burton, M. R., F. Prata, and U. Platt (2015). Volcanological applications of SO₂ cameras. *J. Volcanol. Geotherm. Res.* 300, 2–6.

- Businger, S., S. R. Chiswell, W. C. Ulmer, and R. Johnson (1996). Balloons as a Lagrangian measurement platform for atmospheric research. *J. Geophys. Res. Atmos.* *101*(D2), 4363–4376.
- Businger, S., R. Johnson, and R. Talbot (2006). Scientific insights from four generations of Lagrangian smart balloons in atmospheric research. *Bull. Am. Meteorol. Soc.* *87*(11), 1539–1554.
- Campion, R., H. Delgado-Granados, and T. Mori (2015). Image-based correction of the light dilution effect for SO₂ camera measurements. *J. Volcanol. Geotherm. Res.* *300*, 48–57.
- Carn, S. A., V. E. Fioletov, C. A. McLinden, C. Li, and N. A. Krotkov (2017). A decade of global volcanic SO₂ emissions measured from space. *Sci. Rep.* *7*, 44095.
- Cassiani, M., P. Franzese, and U. Giostra (2005). A PDF micromixing model of dispersion for atmospheric flow. Part I: development of the model, application to homogeneous turbulence and to neutral boundary layer. *Atmos. Environ.* *39*(8), 1457–1469.
- Chang, J. and S. R. Hanna (2010). Modelers’ Data Archive – a Collection of Atmospheric Transport and Dispersion Data Sets. In *90th Amer. Meteorol. Soc. Ann. Meet.*
- Corrsin, S. (1963). Estimates of the Relations between Eulerian and Lagrangian Scales in Large Reynolds Number Turbulence. *J. Atmos. Sci.* *20*(2), 115–119.
- Csanady, G. T. (1973). *Turbulent Diffusion in the Environment*. Dordrecht: Springer Netherlands.
- da Vinci, L. (1510). *Codex Leicester*. Florence, Italy.
- D’Aleo, R., M. Bitetto, D. Delle Donne, G. Tamburello, A. Battaglia, M. Coltelli, D. Patanè, M. Prestifilippo, M. Sciotto, and A. Aiuppa (2016, jul). Spatially resolved SO₂ flux emissions from Mt Etna. *Geophys. Res. Lett.* *43*(14), 7511–7519.
- Dalton, M. P., I. M. Watson, P. A. Nadeau, C. Werner, W. Morrow, and J. M. Shannon (2009). Assessment of the UV camera sulfur dioxide retrieval for point source plumes. *J. Volcanol. Geotherm. Res.* *188*(4), 358–366.
- Deardorff, J. W. (1972, jan). Numerical Investigation of Neutral and Unstable Planetary Boundary Layers. *J. Atmos. Sci.* *29*(1), 91–115.
- Deardorff, J. W. and G. E. Willis (1985). Further results from a laboratory model of the convective planetary boundary layer. *Boundary-Layer Meteorol.* *32*(3), 205–236.
- Dinger, A. S., K. Stebel, M. Cassiani, H. Ardeshiri, C. Bernardo, A. Kylling, S.-y. Park, I. Pisso, N. Schmidbauer, J. Wasseng, and A. Stohl (2018). Observation of turbulent dispersion of artificially released SO₂ puffs with UV cameras. *Atmos. Meas. Tech.* (11), 6169–6188.
- Dosio, A., J. Vilá-Guerau de Arellano, A. A. M. Holtslag, and P. J. H. Builtjes (2005). Relating Eulerian and Lagrangian Statistics for the Turbulent Dispersion in the Atmospheric Convective Boundary Layer. *J. Atmos. Sci.* *62*(4), 1175–1191.

- Edner, H., P. Ragnarson, S. Svanberg, E. Wallinder, R. Ferrara, R. Cioni, B. Raco, and G. Taddeucci (1994). Total fluxes of sulfur dioxide from the Italian volcanoes Etna, Stromboli, and Vulcano measured by differential absorption lidar and passive differential optical absorption spectroscopy. *J. Geophys. Res.* 99(D9), 18827–18838.
- Fast, J. D., K. J. Allwine, R. N. Dietz, K. L. Clawson, and J. C. Torcolini (2006). Dispersion of Perfluorocarbon Tracers within the Salt Lake Valley during VTMX 2000. *J. Appl. Meteorol. Climatol.* 45(6), 793–812.
- Feynman, R. P. (1964). *The Feynman Lectures On Physics*. California Institute of Technology.
- Finn, D., R. G. Carter, R. M. Eckman, J. D. Rich, Z. Gao, and H. Liu (2018). Plume Dispersion in Low-Wind-Speed Conditions During Project Sagebrush Phase 2, with Emphasis on Concentration Variability. *Boundary-Layer Meteorol.* 169(1), 67–91.
- Finn, D., K. Clawson, R. Eckman, R. Carter, J. Rich, B. Reese, S. Beard, M. Brewer, D. Davis, D. Clinger, Z. Gao, and H. Liu (2017). Project sagebrush phase 2; NOAA technical memorandum OAR ARL; 275. Technical report, Air Resources Laboratory, Idaho Falls, Idaho.
- Finn, D., K. L. Clawson, R. M. Eckman, H. Liu, E. S. Russell, Z. Gao, and S. Brooks (2016). Project Sagebrush: Revisiting the Value of the Horizontal Plume Spread Parameter σ_y . *J. Appl. Meteorol. Climatol.* 55(6), 1305–1322.
- Finn, D. D., K. L. Clawson, R. M. Eckman, R. G. Carter, J. D. Rich, T. W. Strong, S. A. Beard, B. R. Reese, D. Davis, H. Liu, E. Russell, Z. Gao, and S. Brooks (2015). Project SageBrush phase 1; NOAA technical memorandum OAR ARL; 268. Technical report, Air Resources Laboratory (U.S.), Idaho Falls, Idaho.
- Fioletov, V. E., C. A. McLinden, N. Krotkov, and C. Li (2015). Lifetimes and emissions of SO₂ from point sources estimated from OMI. *Geophys. Res. Lett.* 42(6), 1969–1976.
- Fioletov, V. E., C. A. McLinden, N. Krotkov, C. Li, J. Joiner, N. Theys, S. Carn, and M. D. Moran (2016). A global catalogue of large SO₂ sources and emissions derived from the Ozone Monitoring Instrument. *Atmos. Chem. Phys.* 16(18), 11497–11519.
- Foken, T. (2008). *Micrometeorology*. Springer, Berlin, Heidelberg.
- Franzese, P. and M. Cassiani (2007). A statistical theory of turbulent relative dispersion. *J. Fluid Mech.* 571, 391–417.
- Fuquay, J. J., C. L. Simpson, M. L. Barad, and J. H. Taylor (1963). Results of Recent Field Programs in Atmospheric Diffusion. *J. Appl. Meteorol.* 2(1), 122–128.
- Galle, B., M. Johansson, C. Rivera, Y. Zhang, M. Kihlman, C. Kern, T. Lehmann, U. Platt, S. Arellano, and S. Hidalgo (2010). Network for Observation of Volcanic and Atmospheric Change (NOVAC) - A global network for volcanic gas monitoring: Network layout and instrument description. *J. Geophys. Res. Atmos.* 115(D05304), 1–19.
- Galmarini, S., A. Stohl, and G. Wotawa (2011, may). Fund experiments on atmospheric hazards. *Nature* 473(7347), 285–285.

- Gant, S., J. Weil, L. Delle Monache, B. McKenna, M. M. Garcia, G. Tickle, H. Tucker, J. Stewart, A. Kelsey, A. McGillivray, R. Batt, H. Witlox, and M. Wardman (2018). Dense gas dispersion model development and testing for the Jack Rabbit II phase 1 chlorine release experiments. *Atmos. Environ.* 192, 218–240.
- Gifford, F. A. (1955). A simultaneous Lagrangian-Eulerian turbulence experiment. *Mon. Weather Rev.* 83(12), 293–301.
- Gifford, F. A. (1957). Relative Atmospheric Diffusion of Smoke Puffs. *J. Meteorol.* 14(5), 410–414.
- Gifford, F. A. (1980). Smoke as a quantitative atmospheric diffusion tracer. *Atmos. Environ.* 14(10), 1119–1121.
- Gliß, J., K. Stebel, A. Kylling, A. S. Dinger, H. Sihler, and A. Sudbø (2017). Pyplis—A Python Software Toolbox for the Analysis of SO₂ Camera Images for Emission Rate Retrievals from Point Sources. *Geosciences* 7(4), 134.
- Gliß, J., K. Stebel, A. Kylling, and A. Sudbø (2018). Improved optical flow velocity analysis in SO₂ camera images of volcanic plumes - Implications for emission-rate retrievals investigated at Mt Etna, Italy and Guallatiri, Chile. *Atmos. Meas. Tech.* 11(2), 781–801.
- Hanna, S. (2010). A history of classic atmospheric dispersion field experiments. In *90th Amer. Meteorol. Soc. Ann. Meet.*, Atlanta (GA).
- Hanna, S. R. (1981). Lagrangian and Eulerian Time-Scale Relations in the Daytime Boundary Layer. *J. Appl. Meteorol.* 20, 242–249.
- Hartl, A., B. C. Song, and I. Pundt (2006). 2-D reconstruction of atmospheric concentration peaks from horizontal long path DOAS tomographic measurements: parametrisation and geometry within a discrete approach. *Atmos. Chem. Phys.* 3(6), 847–861.
- Haugen, D. and J. Fuquay (1963). The Ocean Breeze and Dry Gulch Diffusion Programs. *Air Force Cambridge Res. Lab. Hanford At. Prod. Oper. Rep. HW-78435 1*, 240.
- Hay, J. and F. Pasquill (1959). Diffusion from a Continuous Source in Relation to the Spectrum and Scale of Turbulence. *Adv. Geophys.* 6, 345–365.
- Hiscox, A. L., C. J. Nappo, and D. R. Miller (2006). On the Use of Lidar Images of Smoke Plumes to Measure Dispersion Parameters in the Stable Boundary Layer. *J. Atmos. Ocean. Technol.* 23(8), 1150–1154.
- Huret, N., C. Segonne, S. Payan, G. Salerno, V. Catoire, Y. Ferrec, T. Roberts, A. Pola Fossi, D. Rodriguez, L. Croizé, S. Chevrier, S. Langlois, A. La Spina, and T. Caltabiano (2019). Infrared Hyperspectral and Ultraviolet Remote Measurements of Volcanic Gas Plume at MT Etna during IMAGETNA Campaign. *Remote Sens.* 11(10), 1175.
- Johansson, M., B. Galle, C. Rivera, and Y. Zhang (2009). Tomographic reconstruction of gas plumes using scanning DOAS. *Bull. Volcanol.* 71(10), 1169–1178.
- Jørgensen, H. E. and T. Mikkelsen (1993). Lidar measurements of plume statistics. *Boundary-Layer Meteorol.* 62(1-4), 361–378.

- Jørgensen, H. E., T. Mikkelsen, and H. L. Pécseli (2010). Concentration Fluctuations in Smoke Plumes Released Near the Ground. *Boundary-Layer Meteorol.* 137(3), 345–372.
- Kaimal, J. C. and J. J. Finnigan (1994). *Atmospheric Boundary Layer Flows*. Oxford, England: Oxford University Press.
- Kantzas, E. P., A. J. S. McGonigle, G. Tamburello, A. Aiuppa, and R. G. Bryant (2010). Protocols for UV camera volcanic SO₂ measurements. *J. Volcanol. Geotherm. Res.* 194(1-3), 55–60.
- Kazahaya, R., T. Mori, K. Kazahaya, and J. I. Hirabayashi (2008). Computed tomography reconstruction of SO₂ concentration distribution in the volcanic plume of Miyakejima, Japan, by airborne traverse technique using three UV spectrometers. *Geophys. Res. Lett.* 35(13), 2–7.
- Kemp, M. (2019). Leonardo da Vinci’s laboratory: studies in flow. *Nature* 571, 322–323.
- Kern, C., T. Deutschmann, L. Vogel, M. Wöhrbach, T. Wagner, and U. Platt (2010). Radiative transfer corrections for accurate spectroscopic measurements of volcanic gas emissions. *Bull. Volcanol.* 72(2), 233–247.
- Kern, C., F. Kick, P. Lübcke, L. Vogel, M. Wöhrbach, and U. Platt (2010). Theoretical description of functionality, applications, and limitations of SO₂ cameras for the remote sensing of volcanic plumes. *Atmos. Meas. Tech.* 3(3), 733–749.
- Kern, C., C. Werner, T. Elias, A. J. Sutton, and P. Lübcke (2013). Applying UV cameras for SO₂ detection to distant or optically thick volcanic plumes. *J. Volcanol. Geotherm. Res.* 262, 80–89.
- Klein, A., P. Lübcke, N. Bobrowski, J. Kuhn, and U. Platt (2017). Plume propagation direction determination with SO₂ cameras. *Atmos. Meas. Tech.* 10(3), 979–987.
- Koeltzsch, K. (1998). On the relationship between the Lagrangian and Eulerian time scale. *Atmos. Environ.* 33(1), 117–128.
- Kraus, S. G. (2006). *DOASIS — A framework design for DOAS*. Dissertation, University of Mannheim.
- Kuhn, J., N. Bobrowski, P. Lübcke, L. Vogel, and U. Platt (2014). A Fabry–Perot interferometer-based camera for two-dimensional mapping of SO₂ distributions. *Atmos. Meas. Tech.* 7(11), 3705–3715.
- Kuhn, J., U. Platt, N. Bobrowski, and T. Wagner (2019). Towards imaging of atmospheric trace gases using Fabry–Pérot interferometer correlation spectroscopy in the UV and visible spectral range. *Atmos. Meas. Tech.* 12(1), 735–747.
- Lee, C., R. V. Martin, A. Van Donkelaar, H. Lee, R. R. Dickerson, J. C. Hains, N. Krotkov, A. Richter, K. Vinnikov, and J. J. Schwab (2011). SO₂ emissions and lifetimes: Estimates from inverse modeling using in situ and global, space-based (SCIAMACHY and OMI) observations. *J. Geophys. Res. Atmos.* 116(6), 1–13.
- Louban, I., N. Bobrowski, D. Rouwet, S. Inguaggiato, and U. Platt (2009). Imaging DOAS for volcanological applications. *Bull. Volcanol.* 71(7), 753–765.

- Lübcke, P., N. Bobrowski, S. Illing, C. Kern, J. M. Alvarez Nieves, L. Vogel, J. Zielcke, H. Delgado Granados, and U. Platt (2013). On the absolute calibration of SO₂ cameras. *Atmos. Meas. Tech.* 6(3), 677–696.
- Luo, J., T. Ushijima, O. Kitoh, Z. Lu, and Y. Liu (2007). Lagrangian dispersion in turbulent channel flow and its relationship to Eulerian statistics. *Int. J. Heat Fluid Flow* 28(5), 871–881.
- Luo, J. P., Z. M. Lu, and Y. L. Liu (2010). Lagrangian time scales and its relationship to Eulerian equivalents in turbulent channel flow. *J. Shanghai Univ.* 14(1), 71–75.
- Marmureanu, L., L. Deaconu, J. Vasilescu, N. Ajtai, and C. Talianu (2013). Combined optoelectronic methods used in the monitoring of SO₂ emissions and imissions. *Environ. Eng. Manag. J.* 12(2), 277–282.
- Marro, M., P. Salizzoni, L. Soulhac, and M. Cassiani (2018, jun). Dispersion of a Passive Scalar Fluctuating Plume in a Turbulent Boundary Layer. Part III: Stochastic Modelling. *Boundary-Layer Meteorol.* 167(3), 349–369.
- Mathieu, A., M. Kajino, I. Korsakissok, R. Périllat, D. Quélo, A. Quérel, O. Saunier, T. T. Sekiyama, Y. Igarashi, and D. Didier (2018). Fukushima Daiichi-derived radionuclides in the atmosphere, transport and deposition in Japan: A review. *Appl. Geochemistry* 91, 122–139.
- Mauder, M. (2013). A Comment on “How Well Can We Measure the Vertical Wind Speed? Implications for Fluxes of Energy and Mass” by Kochendorfer et al. *Boundary-Layer Meteorol.* 147(2), 329–335.
- McGonigle, A. J. S., D. R. Hilton, T. P. Fischer, and C. Oppenheimer (2005). Plume velocity determination for volcanic SO₂ flux measurements. *Geophys. Res. Lett.* 32(11).
- McGonigle, A. J. S., T. D. Pering, T. C. Wilkes, G. Tamburello, R. D. Aleo, M. Bitetto, A. Aiuppa, and J. R. Willmott (2017). Ultraviolet Imaging of Volcanic Plumes : A New Paradigm in Volcanology. *Geosciences* 7(68), 1–14.
- Mikkelsen, T., H. E. Jørgensen, M. Nielsen, and S. Ott (2002, dec). Similarity Scaling Of Surface-Released Smoke Plumes. *Boundary-Layer Meteorol.* 105(3), 483–505.
- Mikkelsen, T., S. E. Larsen, and H. L. Pécseli (1987). Diffusion of gaussian puffs. *Q. J. R. Meteorol. Soc.* 113(475), 81–105.
- Mito, Y. and T. J. Hanratty (2002). Use of a modified Langevin equation to describe turbulent dispersion of fluid particles in a channel flow. *Flow, Turbul. Combust.* 68(1), 1–26.
- Monin, A. S. and A. M. Obukhov (1954). Basic laws of turbulent mixing in the surface layer of the atmosphere. *Tr. Akad. Nauk SSSR Geophys Inst.* 24(151), 163–187.
- Monin, A. S. and A. M. Yaglom (1975). *Statistical Fluid Mechanics, Volume II: Mechanics of Turbulence*. Cambridge: MIT Press.
- Mori, T. and M. Burton (2006). The SO₂ camera: A simple, fast and cheap method for ground-based imaging of SO₂ in volcanic plumes. *Geophys. Res. Lett.* 33(24), 1–5.

- Munro, R. J., P. C. Chatwin, and N. Mole (2003, may). Some Simple Statistical Models For Relative And Absolute Dispersion. *Boundary-Layer Meteorol.* 107(2), 253–271.
- Nappo, C. J., D. R. Miller, and A. L. Hiscox (2008). Atmospheric Turbulence and Diffusion Estimates Derived from Plume Image Analysis. *AMS Conf. Air Pollut. Meteorol. Frank Gifford Meml. Sess. 2*.
- Nodop, K., R. Connolly, and F. Girardi (1998). The field campaigns of the European Tracer Experiment (ETEX). *Atmos. Environ.* 32(24), 4095–4108.
- Olesen, H. R., R. Berkowicz, and P. Løfstrøm (2007). Evaluation of OML and AERMOD. In *11th Int. Conf. Harmon. within Atmos. Dispers. Model. Regul. Purp.*
- Oppenheimer, C., T. P. Fischer, and B. Scaillet (2013). *Volcanic Degassing: Process and Impact* (2 ed.), Volume 4. Elsevier Ltd.
- Osorio, M., N. Casaballe, G. Belsterli, M. Barreto, A. Gómez, J. A. Ferrari, and E. Frins (2017). Plume segmentation from UV camera images for SO₂ emission rate quantification on cloud days. *Remote Sens.* 9(6), 517.
- Pasquill, F. and F. B. Smith (1983). *Atmospheric Diffusion (3rd edition)*. Chichester, England: Ellis Hordwood, Ltd.
- Peters, N., A. Hoffmann, T. Barnie, M. Herzog, and C. Oppenheimer (2015). Use of motion estimation algorithms for improved flux measurements using SO₂ cameras. *J. Volcanol. Geotherm. Res.* 300, 58–69.
- Peterson, R., P. Webley, R. D’Amours, R. Servranckx, B. Stunder, and K. Papp (2015). Volcanic ash transport and dispersion models. In *Monit. Volcanoes North Pacific*, Chapter 7, pp. 187–233. Springer, Berlin, Heidelberg.
- Pinsky, M., A. Khain, and A. Korolev (2016, jul). Theoretical analysis of mixing in liquid clouds – Part 3: Inhomogeneous mixing. *Atmos. Chem. Phys.* 16(14), 9273–9297.
- Pisso, I., E. Sollum, H. Grythe, N. Kristiansen, M. Cassiani, S. Eckhardt, D. Arnold, D. Morton, R. L. Thompson, C. D. Groot Zwaafink, N. Evangeliou, H. Sodemann, L. Haimberger, S. Henne, D. Brunner, J. F. Burkhardt, A. Fouilloux, J. Brioude, A. Philipp, P. Seibert, and A. Stohl (2019, jan). The Lagrangian particle dispersion model FLEXPART version 10.3. *Geosci. Model Dev. Discuss.*, 1–67.
- Platt, U., N. Bobrowski, and A. Butz (2018). Ground-Based Remote Sensing and Imaging of Volcanic Gases and Quantitative Determination of Multi-Species Emission Fluxes. *Geosciences* 8(2), 44.
- Platt, U., P. Lübcke, J. Kuhn, N. Bobrowski, F. Prata, M. Burton, and C. Kern (2015). Quantitative imaging of volcanic plumes - Results, needs, and future trends. *J. Volcanol. Geotherm. Res.* 300, 7–21.
- Platt, U. and J. Stutz (2008). *Differential Optical Absorption Spectroscopy — Principles and Applications*. Physics of Earth and Space Environments. Berlin, Heidelberg: Springer.
- Pope, S. B. (2000). *Turbulent Flows*. Cambridge: Cambridge University Press.

- Prata, A. J. (2014). Measuring SO₂ ship emissions with an ultraviolet imaging camera. *Atmos. Meas. Tech.* 7(5), 1213–1229.
- Prata, A. J. and C. Bernardo (2014). Retrieval of sulfur dioxide from a ground-based thermal infrared imaging camera. *Atmos. Meas. Tech.* 7(9), 2807–2828.
- Richardson, L. F. (1926). Atmospheric Diffusion Shown on a Distance-Neighbour Graph. *Proc. R. Soc. London, Ser. A* 110(756), 709–737.
- Roberts, O. F. T. (1923). The Theoretical Scattering of Smoke in a Turbulent Atmosphere. *Proc. R. Soc. A Math. Phys. Eng. Sci.* 104(728), 640–654.
- Roedel, W. and T. Wagner (2011). *Physik unserer Umwelt: Die Atmosphäre.*
- Saffman, P. G. (1963). An approximate calculation of the Lagrangian auto-correlation coefficient for stationary homogeneous turbulence. *Appl. Sci. Res.* 11(3), 245–255.
- Sawford, B. (2001a). Project Prairie Grass—a classic atmospheric dispersion experiment revisited. In *14th Aust. Fluid Mech. Conf.*, pp. 175–178.
- Sawford, B. (2001b). Turbulent Relative Dispersion. *Annu. Rev. Fluid Mech.* (2), 289–317.
- Sawford, B. (2004). Micro-Mixing Modelling of Scalar Fluctuations for Plumes in Homogeneous Turbulence. *Flow, Turbul. Combust.* 72(2-4), 133–160.
- Schröter, M., A. Obermeier, D. Brüggemann, M. Plechschmidt, and O. Klemm (2003, jun). Remote monitoring of air pollutant emissions from point sources by a mobile lidar/sodar system. *J. Air Waste Manag. Assoc.* 53(6), 716–23.
- Shinohara, H. (2005). A new technique to estimate volcanic gas composition: plume measurements with a portable multi-sensor system. *J. Volcanol. Geotherm. Res.* 143(4), 319–333.
- Smekens, J. F., M. R. Burton, and A. B. Clarke (2015). Validation of the SO₂ camera for high temporal and spatial resolution monitoring of SO₂ emissions. *J. Volcanol. Geotherm. Res.* 300, 37–47.
- Stebel, K., A. Amigo, H. Thomas, and A. J. Prata (2014). First estimates of fumarolic SO₂ fluxes from Putana volcano, Chile, using an ultraviolet imaging camera. *J. Volcanol. Geotherm. Res.* 300, 112–120.
- Stohl, A. and D. J. Thomson (1999, jan). A Density Correction for Lagrangian Particle Dispersion Models. *Boundary-Layer Meteorol.* 90(1), 155–167.
- Stoiber, R., L. Malinconico, and S. Williams (1983). Use of the Correlation Spectrometer at volcanoes. In H. Tazieff and J.-C. Sabroux (Eds.), *Forecast. Volcan. Events*, pp. 425–444. Amsterdam: Elsevier.
- Stull, R. B. (1988). *An Introduction to Boundary Layer Meteorology.* Boston: Kluwer Academic Publisher.
- Taylor, G. I. (1921). Diffusion by continuous movements. *Proc. London Math. Soc.* 20(1), 196–212.

- Taylor, G. I. (1938). The spectrum of turbulence. *Proc. R. Soc. A* *164*, 476–490.
- Vandaele, A., C. Hermans, and S. Fally (2009). Fourier transform measurements of SO₂ absorption cross sections: II. Temperature dependence in the 29 000–44 000 cm⁻¹ (227–345 nm) region. *J. Quant. Spectrosc. Radiat. Transf.* *110*(18), 2115–2126.
- Venkatram, A. (2010). The Impact of the Prairie Grass and the St.Louis Dispersion Experiments on Dispersion Modeling Practice. In *16th Conf. Air Pollut. Meteorol.*
- Vickers, D. and L. Mahrt (1997). Quality Control and Flux Sampling Problems for Tower and Aircraft Data. *J. Atmos. Ocean. Technol.* *14*(3), 512–526.
- Wandel, C. F. and O. Kofoed-Hansen (1962). On the Eulerian-Lagrangian transform in the statistical theory of turbulence. *J. Geophys. Res.* *67*(8), 3089–3093.
- Wang, Q., K. D. Squires, and X. Wu (1995). Lagrangian statistics in turbulent channel flow. *Atmos. Environ.* *29*(18), 2417–2427.
- Wilczak, J. M., S. P. Oncley, and S. A. Stage (2001). Sonic anemometer tilt correction algorithms. *Boundary-Layer Meteorol.* *99*, 127–150.
- Wood, K., H. Thomas, M. Watson, A. Calway, T. Richardson, K. Stebel, A. Naismith, L. Berthoud, and J. Lucas (2019). Measurement of three dimensional volcanic plume properties using multiple ground based infrared cameras. *ISPRS J. Photogramm. Remote Sens.* *154*, 163–175.
- Wright, T. E., M. Burton, D. M. Pyle, and T. Caltabiano (2008). Scanning tomography of SO₂ distribution in a volcanic gas plume. *Geophys. Res. Lett.* *35*(17), 1–5.
- Yeung, P. K. (2002). Lagrangian Investigations of Turbulence. *Annu. Rev. Fluid Mech.* *34*(1), 115–142.
- Zak, B. (1981). Lagrangian measurements of sulfur dioxide to sulfate conversion rates. *Atmos. Environ.* *15*(12), 2583–2591.
- Zhang, Z. (2000). A Flexible New Technique for Camera Calibration (Technical Report). *IEEE Trans. Pattern Anal. Mach. Intell.* *22*(11), 1330–1334.

Acknowledgements

This work has been performed within the COMTESSA project which has received funding from the European Research Council (ERC) under the European Union's Horizon 2020 research and innovation programme under grant agreement no. 670462.

I want to express my deep gratitude to all the people who supported me during the work for this thesis. My deep thanks go to my doctoral adviser Prof. Dr. Ulrich Platt who inspired me to pursue this research direction in the first place and accepted me as PhD student. He had always time for helpful discussions and good advice.

I want to thank Prof. Dr. Werner Aeschbach for agreeing to prepare the second referees' report for this thesis. Further, I want to thank Prof. Dr. Ulrich Schwarz and Prof. Dr. Christian Enss for joining the examination committee.

I want to thank my external doctoral advisors Dr. Kerstin Stebel and Dr. Andreas Stohl from NILU for giving me the possibility to join the COMTESSA project. Their guidance and support was invaluable for conducting this work.

I want to thank the entire COMTESSA team: Dr. Hamidreza Ardeshiri, Dr. Massimo Cassiani, Dr. Arve Kylling, Dr. Soon-Young Park, Dr. Ignacio Pisso, Dr. Norbert Schmidbauer, Dr. Kerstin Stebel and Dr. Andreas Stohl. Particularly, I want to thank every single one for the great commitment during the three tracer experiments. In this context, I also want to thank all additional staff which supported our campaigns (Jan Wasseng, Anne-Cathrine Nilsen, Eirik Haugen, Leo Stohl and Kjeller Windteknikk) and the Norwegian military for giving us access to the Regionfelt Østlandet.

I am grateful to Dr. Cirilo Bernardo for designing and developing the SO₂ cameras remotely and I want to thank Rolf Haugen for his unfailing good mood and his help in the lab with assembling and further developing the cameras. I also want to thank Dr. Jonas Gliš for always being up to discuss any aspect of SO₂ cameras or python code. I am grateful for the possibility to use the SO₂ cameras in a more traditional setting during two volcanic measurements campaigns. I enjoyed the scientific and technical discussions during and after the measurements which I certainly could use also for the other field studies. In particular, I want to thank the EPICC team during the campaign at Etna and the extended COMTESSA team at Stromboli.

Many great thanks go to Dr. Massimo Cassiani for his knowledgeable guidance when I dived deeper into the analysis of turbulent dispersion. Here, I also want to thank Dr. Hamidreza Ardeshiri for providing me with the analysed eddy covariance data and for the endless time he spent explaining me what he did. Further, I want to thank Prof. Bjørn Anders Pettersson Reif from the University of Oslo for taking time to discuss the principles of atmospheric turbulence with me and sharing his passion for the field.

Further, I enjoyed being part of both Atmos at NILU and Luftchem at IUP who always welcomed me back whenever I was in Heidelberg.

I appreciate greatly the feedback I received on this manuscript by Dr. Andreas Stohl, Dr. Kerstin Stebel, Dr. Florian Dinger, Dr. Massimo Cassiani, Dr. Udo Dinger and

Mareike Dinger.

I want to thank my fellow PhD students and non academic friends in Oslo. You are such an inspiring bunch! Living with you through similar experiences and discussing all different perspectives over and over again (over far too expensive beers) was both extremely helpful and motivating. Thank you for sticking through. Similarly, I want to express my gratitude to my study friends from Heidelberg. Sometimes I am certain you know me better than I do. Thank you for making me confront also hard facts and tackle problems I would have preferred to ignore. Many thanks go to my training partners and friends and Oslo Budokan Karate for letting me develop the mindset I needed to face any challenge during my PhD studies. Keep on practising Sanchin!

Last but not least, I want to deeply thank my family for their endless support and for believing in me even when I doubted myself. I want to thank Daniele from all my heart. You always manage to put a smile on my face no matter what. A great part of this work is fruit of your unstoppable efforts and love. Grazie.